An Investigation of Sliding Wear of Ti6Al4V

by
Emile Johan Herselman

Thesis presented in partial fulfilment of the requirements for the degree Master of Science in Industrial Engineering at the University of Stellenbosch

Supervisor: Prof. Guven Akdogan
Co-supervisor: Dr. Gert Adriaan Oosthuizen
Faculty of Engineering
Department of Industrial Engineering

March 2012

Declaration

By submitting this thesis electronically, I declare that the entirety of the work contained therein is my own, original work, that I am the sole author thereof (save to the extent explicitly otherwise stated), that reproduction and publication thereof by Stellenbosch University will not infringe any third party rights and that I have not previously in its entirety or in part submitted it for obtaining any qualification.

March 2012

Abstract

Sliding wear is a complicated form of wear involving different factors. The factors affecting the process are the mechanical properties of the materials, sliding distance, sliding speed, and normal force applied to the contact.

An experimental study was conducted to assess the performance of Ti6Al4V in self-mated and various counterface material contact couples subjected to linear reciprocating dry sliding motion. The normal force was varied for all the experiments to understand the effect it had on specific couples. Sliding wear experiments were also conducted on cemented carbides coupled with Ti6Al4V. In certain applications carbide coatings are used and could possibly come into contact with Ti6Al4V. Cemented carbides used in the study were manufactured through spark plasma sintering and liquid phase sintering. An in depth study was conducted to assess the spark plasma sintered materials and compare these to those manufactured through liquid phase sintering.

The experimental study revealed that an increase in normal force, in sliding experiments, led to an increase in friction and wear volume loss of the Ti6Al4V pin. In addition the experiments found that Ti6Al4V was prone to adhesion and surface oxidation.

Opsomming

Glyslytasie is 'n gekompliseerde slytasievorm wat verskillende faktore behels.Die faktore wat die proses beïnvloed is die meganiese eienskappe van die materiale,gly-afstand,glyspoed en normale druk(krag) wat op die kontakoppervlakte toegepas word.

'n Eksperimentele studie om die werksverrigting van Ti6Al4V in verenigde en verskeie teenwerkende materiaal kontakpare wat onderwerp is aan lineêre omgekeerde droë gly-aksie te assesseer is uitgevoer.Die normale krag vir al die eksperimente om die effek wat dit op die spesifieke pare gehad het te verstaan is gevarieer. Glyslytasie-eksperimente is ook op gesementeerde karbiedes wat met Ti6Al4V gekoppel is,uitgevoer. In sekere toepassings is karbiedlae gebruik en kon moontlik met Ti6Al4V in kontak gekom het. Gesementeerde karbiedes wat in die studie gebruik is, is deur vonkplasmasinter en vloeibare fase-sinter vervaardig. 'n Indieptestudie is ook uitgevoer om die vonkplasmasintermateriale en dié materiale wat deur vloeibare fasesinter vervaardig is te vergelyk.

Die eksperimentele studie het getoon dat 'n toename in normale krag in glyeksperimente gelei het tot 'n toename in wrywing en slytasievolumeverlies van die Ti6Al4V pin. Bykomend tot die eksperimente is gevind dat Ti6Al4V geneig was tot adhesie en oppervlakteoksidasie.

Acknowledgements

The author would like to thank the following people for their contribution(s) to this study and the following companies:

Prof. G. Akdogan for his guidance, advice and patience throughout the study,

Dr. G. A. Oosthuizen for his guidance and advice,

Dr. N. Sacks for her guidance and advice,

Friends and family for their continuing support and insight,

DST/NRF Centre of Excellence in Strong Materials, South Africa, for financial support,

Element 6 (Pty) Ltd for the use of scientific equipment,

The Department of Materials and Environmental Chemistry, Stockholm University, Sweden for making their SPS facilities available

Table of Contents

List of Figures

List of Tables

Glossary

Abrasion	Form of wear attributed to friction
Adhesion	Form of wear when materials are coupled at high pressure and temperature
Asperity	Rift on the surface of a material
Asperity Junction	Real contact areas between the surfaces
Carbide	See Cemented Carbide
Cemented Carbide	Material manufactured from tungsten carbide powders
Co	Cobalt
DAQ	Data Acquisition Unit
EDM	Electric Discharge Machine
EDS	Electron Dispersive Spectroscopy
Fracture Toughness	Measure of the resistance a material has to further crack propagation once a crack exists
Galling	Form of sever surface damage
Micrometer	Measuring device
Mo	Molybdenum
Ni	Nickel
PECS	Pulse Electric Current Sintering - SPS
SEM	Scanning Electron Microscope
SPS	Spark Plasma Sintering
Tribology	Main aspects of materials, wear and lubrication
Tribometer	Apparatus used for testing wear of material couples
Vickers Hardness	Hardness measurement
WC	Tungsten carbide
XRD	X-Ray Diffraction Spectroscopy
XRF	X-Ray Florescence Spectroscopy
Young's Modulus	Elastic property - measure of rigidity or stiffness of a metal; the ratio of stress, below the proportional limit, to the corresponding strain

Nomenclature

δ	Amplitude (peak-to-peak) [mm]
μ	Coefficient of friction
μ_a	Adhesion coefficient of friction
μ_d	Deformation coefficient of friction
μ_k	Coefficient of dynamic friction
μ_s	Coefficient of static friction
ν	Sliding Speed/Velocity [$m.s^{-1}$]
π	Constant equal to 3.14
ρ	Density [g/mm^3]
υ	Poisson's ratio
υ_L	Longitudinal speed of sound [$m.s^{-1}$]
υ_T	Transverse speed of sound [$m.s^{-1}$]
ω	Motor Speed [rpm]
D	Length of diagonal [mm]
E	Young's Modulus/Elastic modulus [GPa]
f	Sampling rate [Hz]
F	Tangential force [N]
F_i	Mean tangent force [N] for a cycle
G	Shear Modulus [GPa]
H_c	Coercivity [Ka/m]
i	Cycle number
K_{IC}	Fracture Toughness [$MPa.m^{1/2}$]
H_V	Vickers hardness number
l	Crack length [mm]
N	Normal force/load [N]
N_i	Mean normal force [N] for a cycle
n	Number of measurement point in a cycle
r	Radius of cylinder
S	Sliding Distance [m]
V_{loss}	Wear volume loss [mm^3]
y	Number of levels of variables
x	Number of variables

1. Introduction

Tribology is described as the *"science and technology of interacting surfaces in relative motion and of related subjects and practices"* [***1***]. The main aspects tribology deals with are friction, wear and lubrication. Friction is one of the main causes of wasteful energy consumption. In a time were energy resources are at a high cost and are becoming fewer, a reduction in friction could lead to better and more efficient utilization of these resources [***1***]. A reduction in the cost involved in manufacturing and replacing prematurely worn parts will be a benefit, and this can be obtained by using better tribological practices. Friction is described as the *"resistance to motion during sliding or rolling, when a body moves over another tangentially while in contact"* [***2***]. It is caused by the undulated nature of the surfaces in contact. Wear can be described by the *"surface damage or removal of material from one or both of two solid surfaces in a sliding, rolling it impact motion relative to one another"* [***2***]. Wear mostly occurs at the surface interaction at asperities.

In today's society, tribology is vital to machinery. Unwanted friction and wear are, as the name says, unwanted examples of this are internal combustion engines and aircraft engines, gears, cams, bearings and seals [***2***]. When rubbing of surfaces takes place, friction and wear will take place. The purpose of tribology is to minimize losses caused by friction and wear at all levels of technology and by doing this greater efficiency, better performance, fewer breakdowns and significant cost savings can be obtained [***2***]. There are economic factors to consider when discussing wear. The cost of replacing parts, the loss of production through downtime, and through this the loss of business opportunities are all possible results of wear. To add to this there is also the possibility of inferior quality products, inferior performance and increased energy consumption. [***1***]

Titanium alloys are utilized in many different industries, including petroleum refining, chemical processing, surgical implantation, nuclear waste storage, and marine applications [***3***]. Titanium alloys are used extensively in the aerospace industry because of several properties they exhibit. They have a combination of high strength-to-weight ratio which is maintained at elevated temperatures, their fracture resistance as well as their high resistance to corrosion [***3***]. Aircrafts operate in harsh environments and can go from sea-level to 40 000 feet or even up to an altitude of 50 000 feet [***4***]. Exterior environmental temperatures experienced by aircraft can vary between -55 °C to +90 °C, and depend on the part of the world the aircraft is operating in [***4***]. These conditions can cause various types of wear to occur. Some of the main areas where this wear can occur are in the engines, on the aircraft skin and on the undercarriage. An aircraft engine has many moving parts and operates at very high rotational speeds in the region of 15 000 revs/min. The wear that is caused by this is usually in the form of abrasive and fretting wear. Within the air passing through the engines, dirt can cause erosive wear within the engine when these particles move over the surfaces within. In the aircraft landing gear wear takes place and brakes on an aircraft create a large amount of friction forces, which in turn

causes a large amount of heat leading to wear. The website PlaneCrashInfo.com states that 28% [***5***] of aircraft accidents in the 2000's were caused by mechanical failure, this statistic highlights the importance of maintenance regarding safety. All aircrafts require maintenance and repair. Law and airline regulatory bodies regulate maintenance and repair in the interest of safety. In the USA aircraft are required to be inspected every 3 -5 days according to regulations [***6***] and if the regulations are not followed an aircraft can be grounded. Maintenance and repair of aircraft is costly and causes downtime. An aircraft that is not flying is losing profits for the operator. According to an article written by Battles [***7***] in 2003, it is estimated that maintenance costs between 10 and 45% of the total yearly operating expenses for an aircraft. In another survey performed, a functional cost allocation was produced. The data produced listed maintenance cost of 9.4% of the total costs [***6***]. This is a significant portion if the total operating costs are in the millions of dollars. The maintenance costs can also be broken up further into labour and the cost of equipment and materials. Considering these numbers, it is better practice to prevent wear than replacing parts and less costly for the life of the aircraft.

Different materials are used within aircraft to deal with wear issues and operating conditions. Specialist materials such as aluminium and titanium alloys are used because of their high strength-to-weight ratio, on the fans of a jet engine. In the High Pressure Compressor (HPC) Inconel 718 is used because of its high-strength, thermal-resistance (HSTR) and its exceptional corrosion resistance [***8***]. In the aerospace industry tungsten carbide is used as an erosion resistant coating for components [***9***]. Thermal spray coatings of tungsten carbide are used to lessen the effects of midspan damper wear on jet engine fans and compressor blades [***10***]. WC-Co-Cr has exhibited superior performance as a coating for landing gear components [***11***]. The different materials that are used within an aircraft need to be tested to see if their performance under certain conditions is acceptable to the designer and this is where accelerated wear tests can be used. Accelerated laboratory wear tests using test machinery are popular within the surface engineering research community. Different machinery can be used to understand the tribological behaviour of material couples, several of the techniques used are: pin-on-disc, block-on-ring, micro-abrasion, ballon-plate impact and reciprocating-sliding wear tests [***12***]. These techniques are capable of providing reliable information to how materials react under different conditions and material couples.

In a sliding system, many factors can have an influence on the wear behaviour. Factors influencing the system include the counterface material, properties of the specimen material, experimental conditions and how the materials react with the environment.

Various authors have conducted sliding wear experiments to understand the poor wear performance of the titanium alloy, Ti6Al4V. Molinari [***13***], conducted a study to understand of the mechanisms that cause wear in the alloy, Ti6Al4V, under dry sliding conditions. The study highlights the mechanisms responsible for wear, so as to optimize surface treatments. A disk-on-disk configuration was used and the same alloy was used for the counter face material. Different loads varying form 35 – 200N and different sliding speeds

varying from 0.3 – 0.8 m/s were considered. Straffelini [***14***], conducted experiments on the Ti6Al4V alloy under dry sliding conditions with different sliding speeds, loads and counter face material. Speeds were varied between 0.3 – 0.8m/s, loads between 50 – 200N, and the counter face material was itself and AISI M2 Steel. A disk-on-disk configuration was used for the experiments in the study. In the studies discussed the low resistance of the Ti6Al4V alloy to wear was confirmed. It was found that in dry sliding wear the Ti6Al4V alloy underwent forms of oxidative wear and plastic shearing.

Various authors have studied the effect of sliding on carbide couples with various configurations using accelerated wear machinery. Bonny [***15***] studied the wear of WC-Co cemented carbides using a reciprocating sliding wear test tribometer TE77 according to ASTM G133. The WC-10wt%Co and WC-12wt%Co carbides were used as plate specimens and the pin was made of WC-6wt% Co carbide. The wear experiments were performed with a normal force from 15N to 100N, amplitude of 15mm and a velocity ranging between 0.3 up to 0.9 m/s. The sliding distance for the experiments was 10km. Quercia [***16***] conducted a study of friction and wear characteristics in dry reciprocating sliding contact of WC-Co cemented carbides on a pin-on-disk configuration (ASTM G99-95 procedure). Different grades of WC-Co with varying Co contents were used and the pin was made from a standard hardened martensitic steel ball. The test conditions were as follows: 0.52 m/s sliding speed, 500m sliding distance, normal loads of 2, 5 and 10 N and 75±5% relative humidity of air. Pirso [***17***] conducted a study of the wear of WC-Co cemented carbides on a modified block-on-ring sliding wear apparatus. The ring was manufactured from steel and the tests were conducted under dry sliding conditions. The test conditions were as follows: 2.2 m/s sliding speed and a normal load of 40N. Engqvist [***18***] placed two self-mated cemented carbide-sliding rings face-to-face to study sliding wear. One of the disks was rotated while the other disk was kept stationery. The study was done under dry sliding conditions and other conditions are as follows: sliding speeds equal to 7.9 and 3.8 m/s for the larger ring, and 3.1 and 1.6m/s for the smaller ring. The normal load was varied between 40 – 350N. All previous mentioned studies show that WC-Co cemented carbide shows high-quality wear resistance under dry sliding conditions.

1.1. Project Scope

The *purpose* of the project is to assess dry sliding wear of the titanium alloy Ti6Al4V in contact with different counterface materials. Considering that maintenance for aircrafts take up a large portion of the operating costs, the project aims to understand the reactions of specific material contact couples. A better understanding of materials couples could possibly reduce the costs of maintenance, through preventing wear, rather than replacing parts. The project focuses on dry sliding wear between materials that are predominantly used in aircraft and exposed to harsh environments. The two main causes of wear on machine parts can be attributed to adhesive and abrasive wear [***19***]. During sliding changes in the material influence the wear of the material and a better understanding is needed to be able to control the wear [***19***]. The project aims to

understand wear of different aerospace contact material couples, as well as, specific cemented carbide couples. Cemented carbides are used mostly as coatings in aircraft application [***10***,***11***]. Using a custom built linear reciprocating sliding apparatus the wear properties of specific materials namely, an aerospace titanium alloy, Inconel 718 and different cemented carbides, were tested in different combinations using various normal forces.

The *first objective* of the project was to do a comprehensive literature review regarding friction, wear, dry sliding wear, and the materials mechanical and microstructure characterization. This provides a basis for the study and the understanding of the materials.

The *second objective* was to design the current sliding apparatus used in accelerated laboratory experiments. Included in this objective was to have the new machine parts manufactured and the apparatus commissioned.

The *third objective* assesses and compares spark-plasma sintered cemented carbides to conventionally sintered cemented carbide in terms of mechanical- and material characterization. Specific outputs were used to compare the materials and they included hardness, fracture toughness, elastic properties, SEM, and EDS,

The *fourth objective* was the evaluation of linear reciprocating sliding wear characteristics of current aircraft materials, Ti6Al4V and Inconel 718. The *fifth objective* was to compare specific outputs from the sliding experiments of Ti6Al4V self-mated couples with those of the Ti6Al4V coupled with the cemented carbides.

The *approach* was to have an experimental design for the different normal forces and the different material couples used for the study. Analysis of the friction coefficient, wear volume loss, wear scar analysis of both the pin, and counterface material were used as outputs. These outputs were used to understand the sliding wear behaviour of Ti6Al4V and determine the effects of the normal force on the various contact couples.

The *goal* of the thesis was to understand the impact of materials in contact after sliding with different normal loads. The materials experimented with were coupled in different configurations and normal loads.

Chapter 2 presents a literature review of friction, sliding wear and the materials used in this study. Chapter 3 describes the materials and methods used in the study. The chapter describes the mechanical and microstructure characterization experiments performed on the SPS cemented carbides, the design of the sliding apparatus and the methodology and process used in the sliding experiments. The results from the mechanical and material characterization experiments on the SPS cemented carbides and the results from the sliding experiments are presented in Chapter 4. Conclusions and recommendations are presented in Chapter 5.

2. Literature Review

The current chapter presents the literature review. In the review the different sections are discussed and are as follows; friction, sliding wear and the wear mechanisms involved, the materials Ti6Al4V, and Inconel 718. Understanding the different concepts of friction and wear, coupled with understanding of the materials are integral to assessing how materials can possibly react under certain conditions and in different combinations.

2.1 Friction

According to Smithells Metals Reference Book [***20***], "*Friction is the resistance to motion when two bodies in contact slide on one another*".

Friction is described by Hutchings [***21***], as "*the resistance encountered by one body moving over another"*. According to Hutchings [***21***], there are two classes of relative motion: sliding and rolling [***21***]. In rolling, there is also a case of sliding in most instances. The two classes are not mutually exclusive [***21***]. Figure 2.1 illustrates the two different contacts that may occur.

Figure 2.1: Illustrations of a rolling contact and a sliding contact with frictional force F (adapted from [***2***,***21***])

There two types of friction that are encountered and these are dry friction and fluid friction. Dry friction is also known as Coulomb friction and is described as the tangential component of the force when two bodies move relative to each other. Fluid friction is described as the tangential component of the force when between adjacent layers in a fluid that are moving relative to each other at different velocities. An example of this would be a liquid or gas between bearing surfaces. [***2***] Only dry friction will be considered in this document. It must be noted that friction is not a material property, but a system response [***2***].

The Laws of Sliding Friction, also known, as Amonton's Laws are valid for many experimental conditions, and are described below [***20***,***21***]*:*

1. The first law states that the frictional force (F) between bodies is proportional to the normal force between surfaces.
2. The *second law states that the frictional force (F) is independent of the apparent area of contact.*

A third law [***21***] is added on occasion and attributed to Coulomb (1785). This law is normally an observation of the force needed to initiate sliding is higher than the force needed to maintain it.

3. The friction force is independent of sliding velocity

A model was developed by Bowden and Tabor (1930's – 1970's) for sliding friction. The model assumes that there are two forces that create the frictional forces: adhesion force that is developed at the real contact areas between the surfaces (asperity junctions) and a deformation force that ploughs the asperities of the harder surface through the softer of the materials surface. The frictional force is then the sum of the adhesion force and the deformation force [***21***]. This force is the cause of friction. Equation 2.1 shows how the coefficient of friction can be broken up into these components. [***20***]

$$\mu = \mu_a + \mu_d \qquad 2.1$$

At the asperity contacts, adhesion arises, caused by the attractive forces. This assumption holds when both surfaces are free from oxides and other surface films and absorbed gasses for example in an ultra-high vacuum environment. Under normal conditions, adhesion between two metal surfaces is not observed. There are two reasons for this. The first is the surfaces will most probably be covered with oxide and absorbed films. These oxides and films weaken the adhesion between the surfaces. The second reason is elastic strain around the asperities. The elastic strains, under load, generate stress to break the asperity junctions during the unloading process. If the metal is very ductile there is a chance that this will not happen. Adhesion will be observed if one of the materials is soft and ductile and oxide films are not present under ordinary conditions. When two metals slide against one another the asperity junctions formed will be stronger than the weaker of the materials. This can lead to plucking out and transferring of the softer material and can cause severe wear on the softer material. [***21***]

Equation 2.2 is an equation of equilibrium [***20***,***22***].

$$\mu = \frac{F}{N} \qquad 2.2$$

F is the force required to initiate/maintain motion, N is the normal reaction of one body on another and μ is the coefficient of friction or the proportionality constant. μ will be described as the coefficient of friction for further use in this document.

Up to the point of slippage or impeding motion as shown in Figure 2.2 (d), the region is called the range of static friction. For this range the value of the friction force is determined by the equations of equilibrium (Equation 2.1 and equation 2.2) [***22***]. At this point F_{max} is proportional to N. μ_s is known as the coefficient of static friction [***22***] as shown in equation 2.3.

$$\mu_s = \frac{F_s}{N} \tag{2.3}$$

Once slippage occurs, a condition of kinetic friction commences with the motion. Equation 2.4 describes this motion and μ_k is known as the coefficient of dynamic friction. In general, the coefficient of kinetic friction (μ_k) is less than that of the coefficient of static friction (μ_s) as shown in the equation 2.5 [***22***].

$$\mu_k = \frac{F_k}{N} \tag{2.4}$$

$$\mu_k < \mu_s \tag{2.5}$$

An increase of velocities of the surfaces causes a decrease of kinetic friction, and at relatively high velocities the decrease can be significant [***22***].

The solid block is resting on a horizontal surface, as shown in Figure 2.2 a). It assumed that both surface are rough. Force P is applied as shown in the figures below. This force continuously increases from zero until it can move the block at a notable velocity. Figure 2.2 b) is the free body diagram for any value of P. The tangential friction force is labelled F and will always be in the direction that opposes motion or impeding motion. The normal force N equals mg in the figures and R is the total force exerted by the supporting surface on the block resulting from F and N. [***22***]

Figure 2.2 c) depicts the irregularities of the two mating surfaces. The figure shows that support is irregular, and exists at certain mating humps on the surface. The bearing of each of these forces depends on two factors; 1) the geometric profile of the irregularities, 2) and also on the degree of local deformation. N is the sum of the n-components of the R's and F is the t-components of the R's. [***22***]

From Figure 2.2 d) it can be seen that when P is equal to zero, no friction force is required. If P is increased, the friction force is opposite and equal until the block slips. At a certain point the force P will cause the block to slip and move in the direction of the applied force. Once this point has been reached the friction force will decrease slightly and suddenly. As the velocity increases, so will the friction force over time. [***22***]

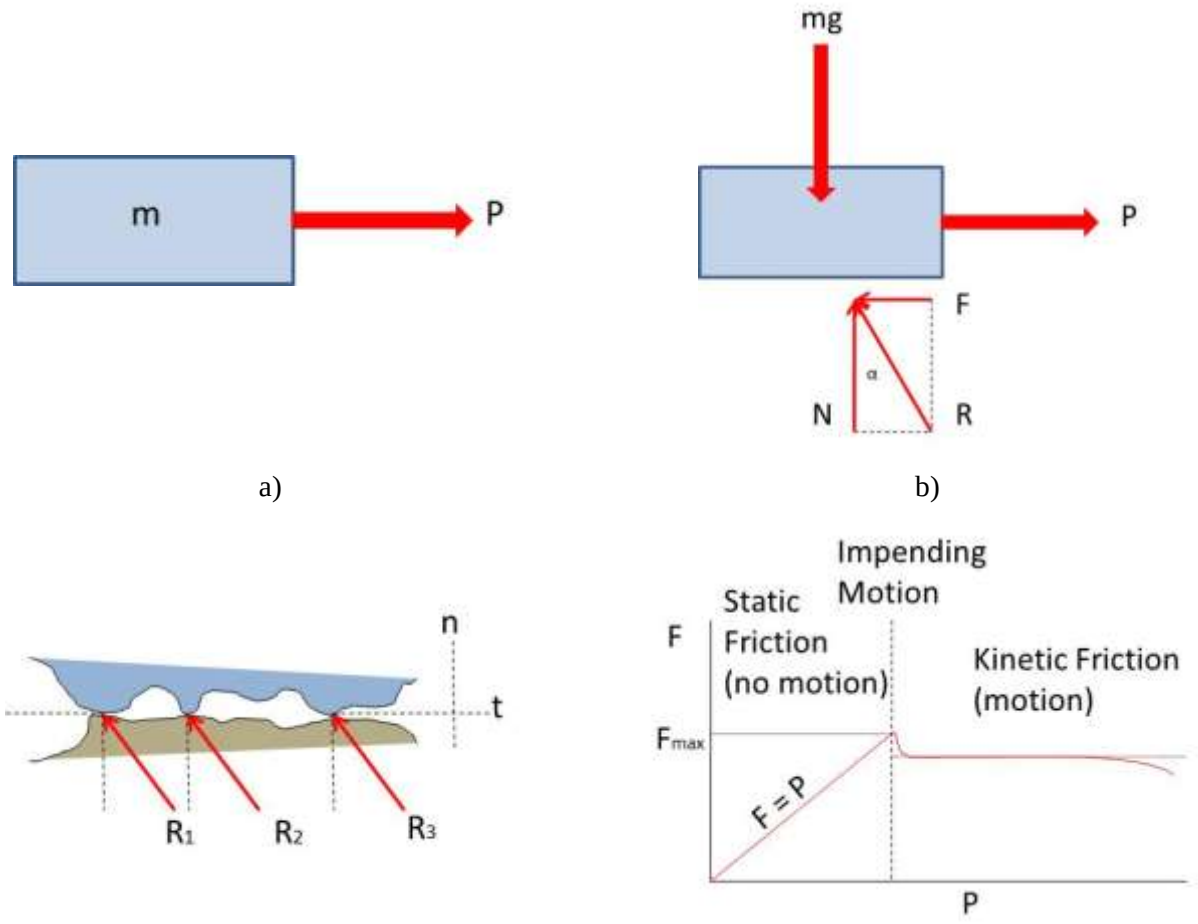

Figure 2.2: Mechanisms of dry sliding friction: a) Block with force P applied, b) free-body diagram, c) magnified irregularities of mated surfaces, d) graph of friction mechanism (all figures adapted from [***22***])

2.2 Sliding Wear

Sliding wear takes place if two materials slide over each other that are forced together. This is the most complex form of wear because different materials react differently to the sliding conditions. [***17***]

As described by Williams [***1***], "*Wear is the progressive damage, involving material loss, that occurs on the surface of a component as a result of its motion relative to the adjacent working parts; it is the almost inevitable companion of friction.*"

A distinction must be made between sliding and fretting wear to understand the minimum sliding amplitude for sliding wear to take place. Fretting wear occurs when two materials are interacting having an oscillatory slip of no more than 150 µm [***1***,***20***]. This form of wear has a typical pattern. The protective oxide layer is disrupted through mechanical action and the reactive metal is exposed. Oxygen in the atmosphere swiftly oxidizes the metal and on the return path, the oxide layer is once again disrupted. The cycle is thus repeated. Particles that are caught in the contact zone can contribute to abrasive wear because of their hardness. Adhesive wear may also be present if the areas of partly oxidized surfaces come into contact [***1***]. By eliminating slip through increasing contact pressure, separating surfaces, lubrication or by surface treatments fretting wear can be reduced [***20***].

Abrasive wear is caused by asperities of surfaces interacting by moving in opposed directions. Two forms of abrasive wear exist. The first is two-body abrasion illustrated in Figure 2.3; this is where two surfaces in contact move in opposite directions and were hard protuberances on the counter face cause wear [***1***,***20***,***21***,***23***]. The second form is three-body abrasion illustrated in Figure 2.4; this form occurs when there are particles between the two interacting surfaces moving in opposite directions that are free to roll and slide. Wear rates vary greatly for materials with different hardness, size and shape [***1***,***20***,***21***,***23***]. The particles that cause two- and three-body wear could possibly be originate from contamination or from the tribosystem itself [***23***].

According to Hutchings [***21***], if two-body wear takes place, the wear rate will be higher than the rate if three-body wear takes place [***21***].

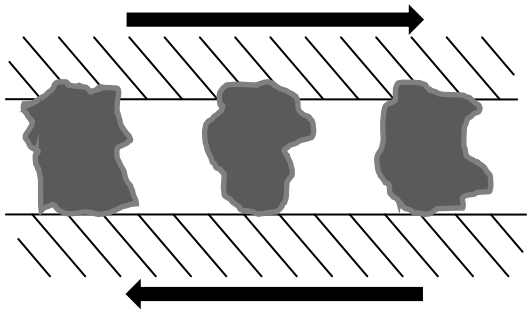

Figure 2.3: Two-body abrasion (adapted from [***21***])

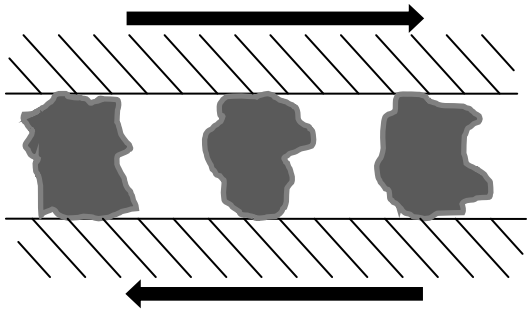

Figure 2.4: Three-body abrasion (adapted from [***21***])

Adhesive wear is a form of wear that occurs when two materials are forced into contact under high pressure and temperature. Welding or adhesion occurs between the two materials. [***24***]

Dry sliding wear takes place when surfaces slide over each other in air without lubricant. The humidity is usually substantial at the air ambient. A misleading term used for sliding wear is adhesive wear. This form of wear is one of the main types of wear, but not the only one that takes place in a sliding system. *Scuffing*, *scoring*, and *galling* are also associated with sliding wear. *Scuffing* describes the local surface damage caused by welding of solid-state sliding surfaces [***21***]. When the lubrication between the contact surfaces breaks down and adhesive wear takes place the term *scuffing* can be used to describe the situation [***1***]. The term *scoring* is a synonym by *scuffing*. These two terms are interchangeable and involve the scratching by abrasive particles [***21***].

A more severe form of wear known as *galling*, is also caused by localized welding, but is coupled with gross surface damage. Asperities that are in contact weld together and the softer tips are removed when adhering to the harder surface. These particles are an agent for wear and severe damage can be caused as a result of small bits of material being torn from the surface. This wear phenomenon is characterized by severely roughened surfaces and displacement of large fragments of material. The damage is usually a result of dry sliding at low speeds. Galling can possibly cause seizure of surfaces and failure of the sliding system [***1***,***21***]. If both materials are, of the same composition, this can be a particularly severe problem as well as when sliding speeds or temperatures are high and there is poor lubrication between the contact areas [***1***].

The work of Holm and Archard [***21***] provided a simple theoretical analysis for sliding wear. The analysis highlights the most influential variables of sliding wear. It also gives a method of describing the severity of wear by means of a wear coefficient.

The model uses the assumption that the where the asperities touch is the contact between the two surfaces. This in turn implies that the total contact area is equal to the sum of the individual asperity contact area. The sum of the areas will be closely relative to the normal load. For metals it can assumed, under the majority of conditions, the deformation of asperities will be plastic. [***21***]

Figure 2.5 shows a single asperity contact when sliding wear occurs. The asperity is assumed circular in shape. Figure 2.5 a) describes the start of the process, just before contact takes place between the asperities. Figure 2.5 b) shows the stage of the process before maximum asperity contact takes place as shown in Figure 2.5 c). As shown in the figure, this is where the contact is the largest [***21***]. The yield pressure of the deforming asperity will now be close to its Hardness value [***21***]. Figure 2.5 d) and e) show how the two asperities are displaced after maximum contact. The load carried by the asperity is progressively transferred to another asperity junction. The process described then takes place at other parts on the surface. In the case

of continuous sliding, individual asperity contacts are in a continuous process of being formed and destroyed [***21***]. In this case, fragments of the material that detached from asperities cause wear. The size of these fragments depends on the material and the size of the asperity junction. [***21***]

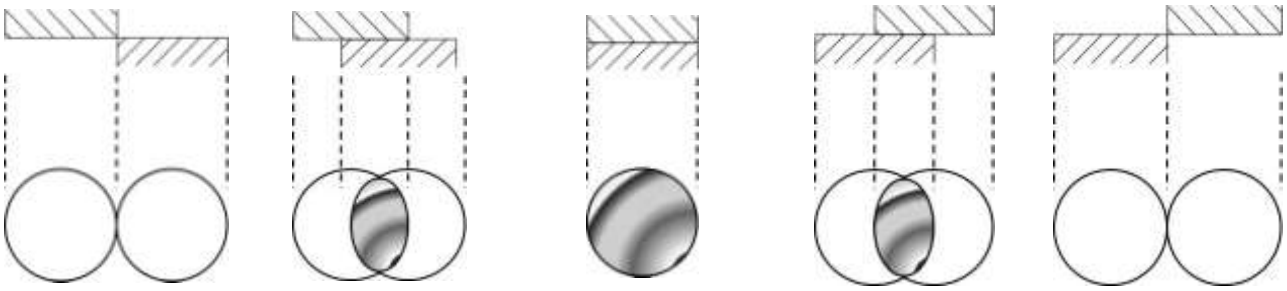

Figure 2.5: Diagram of two asperities moving over each other (adapted from [***21***])

In the interaction between two metals two forms of wear debris are observed. The first is oxide that is observed at high loads and the second is metallic that occurs at intermediate loads. A rapid increase in wear rate is observed in the transition from metallic to oxidative debris. [***20***]

Corrosive wear occurs under the action of repeated stress and chemical attack [***25***]. This form of wear is common in many industries and materials that normally have a high wear resistance, for instance metal matrix composites, might perform inadequately. The high wear rate is caused by break-away of the hard particles in the matrix because of accelerated dissolution of the material at interphase boundaries. [***20***]

In general the wear resistance of a material increases as the hardness increases, except when hardening was done through plastic deformation [***20***]. In conclusion, when wear resistance needs to be taken into account for materials, the most important factor is hardness. For this reason, various surface treatments are used to modify surfaces for enhanced wear resistance. Examples of these treatments are surface alloying, diffusion processes, and coating. [***20***]

Experimental results have shown that the wear (loss of material) is proportional to the sliding distance. These results have also shown that a running in period can take place. In this period, the wear rate could be higher or lower than when the surface conditions have reached a steady-state wear rate. Different systems have different running in processes. [***21***]

2.2.1 Wear of Metals in Unlubricated Conditions

When sliding conditions are varied, namely normal load, sliding velocity and sliding distance, dominant wear mechanisms and wear rate are affected. According to Hutchings [***21***], the main factors controlling the mechanisms are mechanical stresses, temperature and oxidation phenomena [***21***]. Sliding wear is extremely

complex because of the interrelation of these factors. These factors are influenced by sliding velocity and load. The influence of sliding velocity and load are depicted in Figure 2.6. The diagram illustrates how the combined influence of load and sliding velocity affect mechanical damage and the interface temperature. The product of this interaction is the power dissipated at the interface caused by the sliding speed and friction force. At low sliding velocities, heat generated will be removed rapidly and therefore a lower interface temperature will exist. At high sliding velocities, the heat generated will not be rapidly removed that can cause high chemical reactivity on the surfaces and this in turn can lead to the growth of oxide films. Mechanical strength of asperities can also be compromised and in extreme cases cause melting. Mechanical stresses take place. The normal stress takes place at the surface and the shear stresses below the surface. The friction coefficient determines the magnitude and position of these stresses. [***21***]

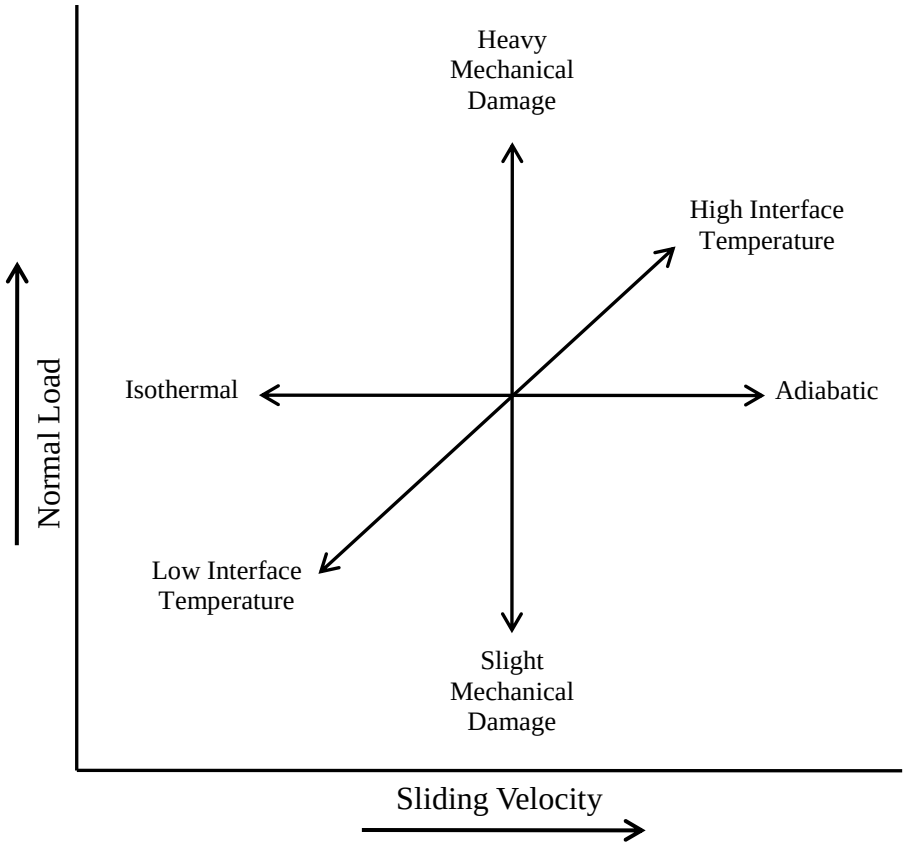

Figure 2.6: Diagram of the influence of sliding velocity and load on the wear process of metals (adapted from [***21***])

2.2.2 Experimentation Methods

A tribotester or tribometer is used to measure friction. Figure 2.7 depicts the different experimental configurations used for sliding wear experiments. The geometries described in the figure are divided into two groups. Asymmetric arrangements cause the wear rate of the materials, even if they are the same, to vary [***21***]. This is a more common experimentation procedure than the symmetric configurations [***21***]. The symmetric arrangements are those that cause the wear rate of the materials to be identical. Examples of the symmetric arrangements are Figure 2.7 a) and b). Figure 2.7 c) to d) depict the asymmetric arrangements.

Figure 2.7 c) is a pin pressed against a disk, d) is pin pressed against a rim of a disk, e) is block loaded against a ring, and f) is a pin on flat configuration. Figure 2.8 shows the different conformal and counter formal contacts.

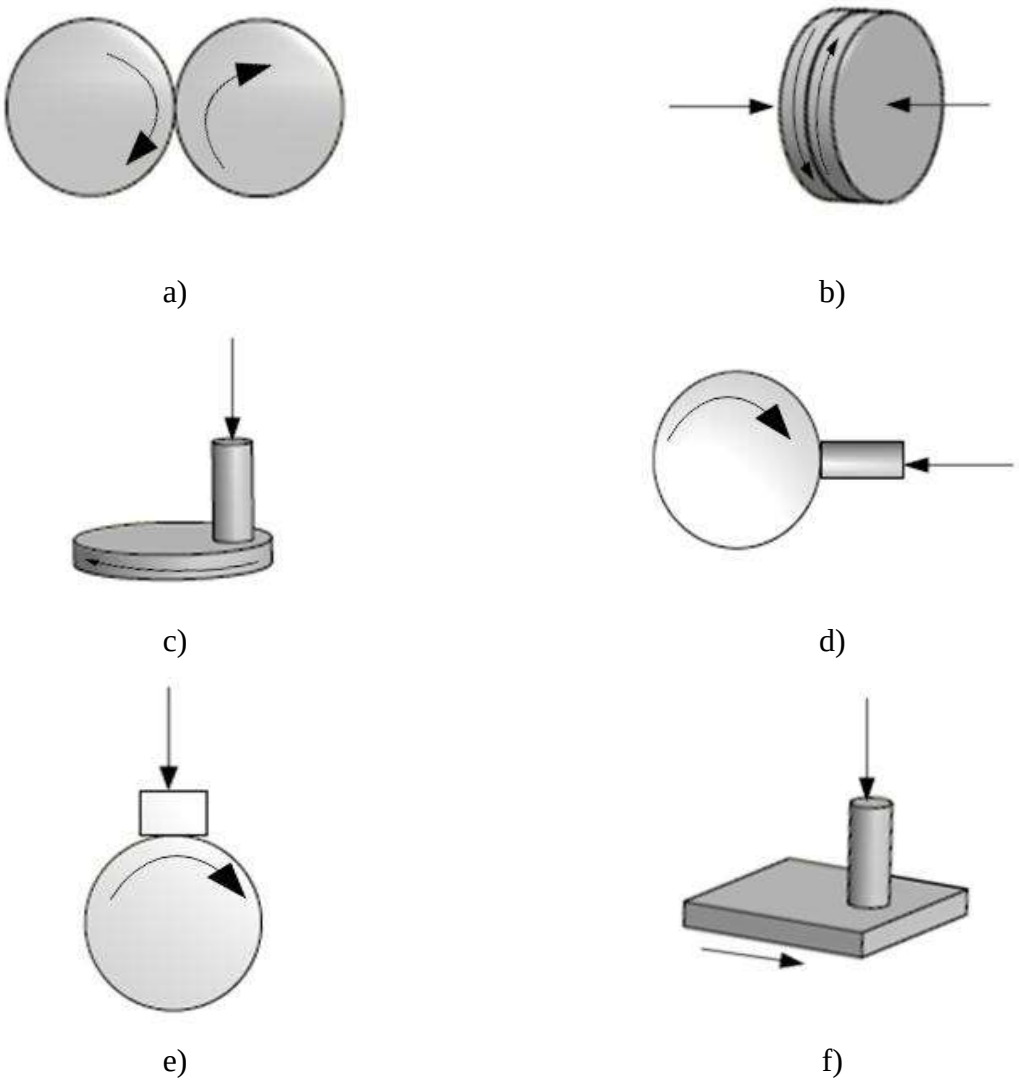

Figure 2.7: Sliding wear experimental configurations (adapted from [***21***])

Figure 2.8: Conformal and counter formal contacts (adapted from [***21***])

2.3 Ti6Al4V

Titanium alloys are used in highly corrosive environments because of its good erosion resistance [***26***]. The Ti6Al4V alloy is the most used titanium alloy used for manufacturing of biomedical devices [***27***].

The properties of the Ti6Al4V are compared to that of pure titanium in Table 2.1 and the composition of the alloy is shown in Table 2.2.

Table 2.1: Properties of titanium and Ti6Al4V at room temperature [***28***,***29***]

Property	**Titanium**	**Ti6Al4V**
Density [g/cm^3]	4.5	4.43
Hardness [HRc]	10-12 (equivalent)	30-36
Modulus of Elasticity [GPa]	116	113.8
Fracture Toughness [Mpa.m^{½}]	70	75

Table 2.2: Composition of Ti6Al4V (wt. %) [***30***]

Al	**V**	**Fe(max)**	**Si(max)**	**C(max)**	**N(max)**	**H(max)**	**O(max)**	**Titanium**
5.5– 6.8	3.5– 4.5	0.3	0.15	0.1	0.05	0.015	0.15	Balance

Pure titanium undergoes an allotropic phase transformation at 882.5°C changing from HCP α-phase to BCC β-phase. The transformation temperature is dependent on alloying elements. Titanium alloys are classified into four main groups: α, near α, α - β, and β, according to their metallurgical characteristics [***31***,***3***]

- **α-Alloys**

  These alloys contain α stabilizers, sometimes in combination with neutral elements. Ti-SAl2½Sn is available commercially and has excellent tensile properties and creep stability at elevated room temperature up to 300°C.

- **Near α-Alloys**
  These alloys contain both α and β phases. They behave more like α-alloys, but can operate at higher temperatures between 400 and 500°C.

- **α-β Alloys**
  Ti6Al4V is the most common and widely used of these alloys and accounts for over 45% of total titanium production [***3***]. It is mainly used for high-strength applications at elevated temperatures between 350 and 400°C.

- **β-Alloys**
  These alloys have good forgability and cold formability with high hardenability as well as high density. They are inferior to α – β alloys at elevated temperatures.

2.3.1 Wear Mechanisms of Ti6Al4V

The titanium alloy used in the experiments was Ti6Al4V. The alloy is the most widely used of the high strength titanium alloys. It falls into the α-β group [***32***]. The Ti6Al4V alloy shows excellent mechanical and chemical properties, but has poor wear resistance. There are two reasons for this of which the first is its low resistance to plastic shearing and the low work hardening. For this reason, the material does not counteract wear phenomena such as adhesion, abrasion and delamination very well. The second reason for its poor wear resistance is due to the low protection exerted by the surface oxide. The oxide is formed by high flash temperatures caused by friction during sliding. The reasons mentioned above contribute to the fact that the Ti6Al4V alloy is used as a structural material. [***13***]

Ti alloys have a high affinity for oxygen. The result of this is an adherent surface oxide, but a form of TiO_2 acts as a solid lubricant [***33***]. Qu [***33***] noted a large fluctuation of the friction coefficient when sliding against stainless steel and ceramics. The fluctuation was considered to be caused by formation and periodic, localized fracture of a transfer layer [***33***]. It has been noted by other researchers that titanium readily transfers material when sliding against other metals [***13***,***33***,***34***,***35***].

Deformation and readily transferring material to the counterface are tribological properties of titanium when sliding in unlubricated contact. An oxide surface layer easily forms as well and this layer readily adheres and transfers to both metallic and no-metallic surfaces. The reason for the oxide layer forming is titanium's attraction of oxygen. Severe adhesive wear is a result of the oxide layer. [***36***]

Molinari [***13***] found that the wear volume increases with increased normal force. Experiments done by Long [***34***] showed that adhesive wear took place with the larger debris, that ploughing caused the formation of smaller debris, and that friction was directly linked to localized asperity deformation and fracture. It was also

found that there was material transfer from the titanium to the counter surface [***34***]. Long [***34***] noted that during the first sliding pass that severe plastic deformation and transfer have been previously observed. This transfer is significant for the Ti6Al4V alloy and acts as a solid-film lubricant. The contact then involves a Ti/Ti contact. This can consequently decrease the coefficient of friction with increasing passes [***34***]. Long [***34***] concluded that the friction behaviours of titanium alloys are controlled by their surface deformation and transfer characteristics. Wear debris and the transfer layer are products of the nature of the surface tribo-layer [***34***].

It was reported by Nazarenko [***37***], that the coefficient of friction for titanium on titanium and other metals was 0.48 – 0.68 for dry contact. Straffelini [***14***] found that at lower sliding velocities (±0.3m/s) an oxidative mechanism had an influence on the wear.

The contribution of delamination at higher loads increases, and thus a subsequent increase in the wear rate. The effect of sliding velocity is less prominent on the wear rate. A decrease of wear rate is initially seen, and followed by a quick transition to sever metallic delamination wear at sliding velocities in the region of 0.01 to 1m/s. [***14***]

The literature described in the section explains why the Ti6Al4V has low wear resistance in sliding contacts.

2.4 Cemented Carbides

C. W. Scheele discovered tungsten in 1781, but it took another 150 years before researchers' labours led to the application of tungsten carbide in industry [***38***]. Moissan in 1893 was the first person to synthesize tungsten carbide and the commercial production of this material started 20 – 25 years afterwards [***39***]. Early in the 20th century, the incandescent lamp industry was attracted to tungsten carbide; so as to use it as a replacement for expensive diamond dies used for drawing tungsten wires [***40***]. According to The International Tungsten Industry Association [***38***], the production of tungsten carbide can be traced to the German electrical bulb company, Osram in the 1920's [***38***]. The combination of high melting point, high hardness and wear resistance made the material an excellent substitute [***40***]. The 1930's saw the launching of cutting tool carbide grades for steel milling by various companies and also the addition of carbides of titanium and tantalum [***38***].

Cemented carbides are utilized in applications were they require a combination of hardness and toughness [***41***]. Tungsten carbide is utilized in many applications in various industries from mechanical to chemical [***40***]. By far the largest use of tungsten carbide is as cemented carbide cutting tools [***20***,***25***,***40***,***42***,***43***]. It is also utilized as mining tools, blade tips, military components, construction [***44***], and wear parts in industries [***40***], and fine drill bits [***38***]. Tungsten carbide is widely used in applications where wear resistance is of paramount importance. For example it is used in abrasive cutting tools, inserts in valve systems, and sand

blast nozzles. The reason it is used in these applications is due to the materials high wear resistance and high hardness [***40***]. In many of the applications the material is exposed to conditions of dry sliding wear [***15***].

Of the many uses for tungsten carbide; the metal cutting parts account for 67%, the mining industry 13%, machining of wood and plastics 11% and construction 9% [***44***]. The most widely used and most basic of these carbide grades is tungsten carbide (WC) [***44***].

In industry today, larger amounts of hardmetals are being produced. This increase can be attributed to several factors that are listed below [***44***] :

- Availability of high-quality raw materials (WC, Co, WC-TiC, TaC, etc)
- High product reliability and standard of manufacturing
- High strength and rigidity, outstanding thermal conductivity, and low thermal expansion insuring excellent adhesion to other materials (ideal coating substrate)
- Able to customise the substrate by creating variations in powders or in sintering technology
- Material reclamation through well-developed recycling processes

Tungsten carbide is used extensively in cutting tool applications as discussed earlier in the chapter. The cutting tools are used in various machining applications for instance, milling, grooving, threading, drilling, and boring. Tungsten carbide material is also used to make solid drill bits for the machining of printed circuit boards. [***44***]

In the aerospace industry tungsten carbide is used as an erosion resistant coating for components [***9***]. Thermal spray coatings of tungsten carbide are used to lessen the effects of midspan damper wear on jet engine fans and compressor blades [***10***].

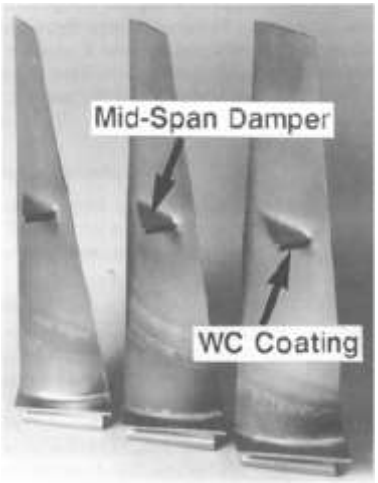

Figure 2.9: Midspan dampers on fan blades [***10***]

New industry applications are being researched for example, tungsten carbide replacing noble metals like lead (Pb), platinum (Pt) and iridium (Ir) in the catalysis industry [***40***]. Tungsten carbide is also in use in the

making of a lead-free bullet in use on certain shooting ranges. In the bullet, lead is being replaced by different metals as it poses certain health threats and environmental risks. Tungsten carbide is one of the principle materials used in the bullet. [***45***]

Within the woodworking industry tungsten carbide is used as circular saw blades, routers, milling cutters. Cutting tools are subjected to high impact forces when cutting wood and for this reason toughness is the most important property of the tooling material. [***46***]

The dental industry uses tungsten carbide in the tools they use for drilling and shaping. These tools have a carbide coated tip. Many of the tools that are used have fine and sharp cutting edges that must be wear resistant and tough. The reason for this is to prevent high cutting forces and heat build-up. [***46***] Tungsten carbide makes a perfect material for these applications as it possess the properties of toughness and wear resistance.

Cemented carbides replaced steel cutting tools in the paper and magnetic tape industry in the 1970's. The reason for this replacement was that steel tools have less wear resistance and thus have to be replaced every few weeks. Cemented carbide tools on the other hand only have to be reground once every year. [***46***] This is another example of the wear resistance of tungsten carbide in industry.

In many industries, cemented carbides are used as chipless forming, blanking and piercing tools. Carbide tools with a binder content of 15 – 20% are 5 – 10 times more wear resistance than high speed tools and can match the toughness. [***46***]

There are many applications for tungsten carbide in industry. Companies are able to make thousands of different shapes with the material and so the uses extend far beyond the applications that have been mentioned. As discussed, the application of this material as cutting tools is by far the greatest.

Hardmetals consist of fine, hard and brittle carbide particles bonded with a tough binder phase which is metallic [***20***]. Tungsten monocarbide (WC) was the original hard phase and the favoured binder phase was cobalt [***20***]. Tungsten carbide provides the hard phase and the binder (ductile matrix) used is cobalt [***41***]. These materials are described as cemented carbides [***20***]. Other carbides besides tungsten can be added and also materials other than cobalt can be used in the binder phase [***20***]. For instance nickel can be used as a binder and TiC and TaC can be used as a different combination carbide [***40***].

Carbides are mainly used as cutting tools [***20***,***24***,***40***,***42***,***43***], oil drilling tools or mining tools today [***20***]. Cemented carbides are mass-produced as tool materials and wear resistant parts [***40***]. No other cost effective substitute material has been developed for the WC/Co hardmetal where wear resistance is the primary requirement, this includes the machining of non-ferrous materials [***20***].

WC is the most important carbide pertaining to cutting tools and according to Koc [***40***] a total of 20 million kilograms of WC-Co composite powders are produced per year [***40***].

Surface coatings for these materials have made a dramatic improvement in tool life when used as cutting tools [***20***].

2.4.1 Liquid Phase Sintering (Conventional Sintering)

Liquid phase sintering is used to produce cemented carbides. This means that powders of WC and cobalt are pressed and sintered at a temperature above the eutectic temperature. Tungsten carbide is produced by mixing tungsten metal and carbon black that is then carburized at high temperatures. The powders of the two materials are wet milled to coat each carbide particle with cobalt, and in order to do this the cobalt particles must be incredibly small. [***20***] This process is followed by spray drying and compaction of green bodies [***41***].

A problem occurs with these small particles as these forms of powder do not flow easily, but a solution for this problem has been implemented and is known as granulation. Granulation means the production of agglomerates [***20***]. The aim of this heterogeneous mixture is to combine the strength and toughness of this binder (cobalt), with the hardness and thermal resistance of the ceramic (tungsten carbide) [***1***]. Figure 2.10 is a schematic for the production of hardmetals.

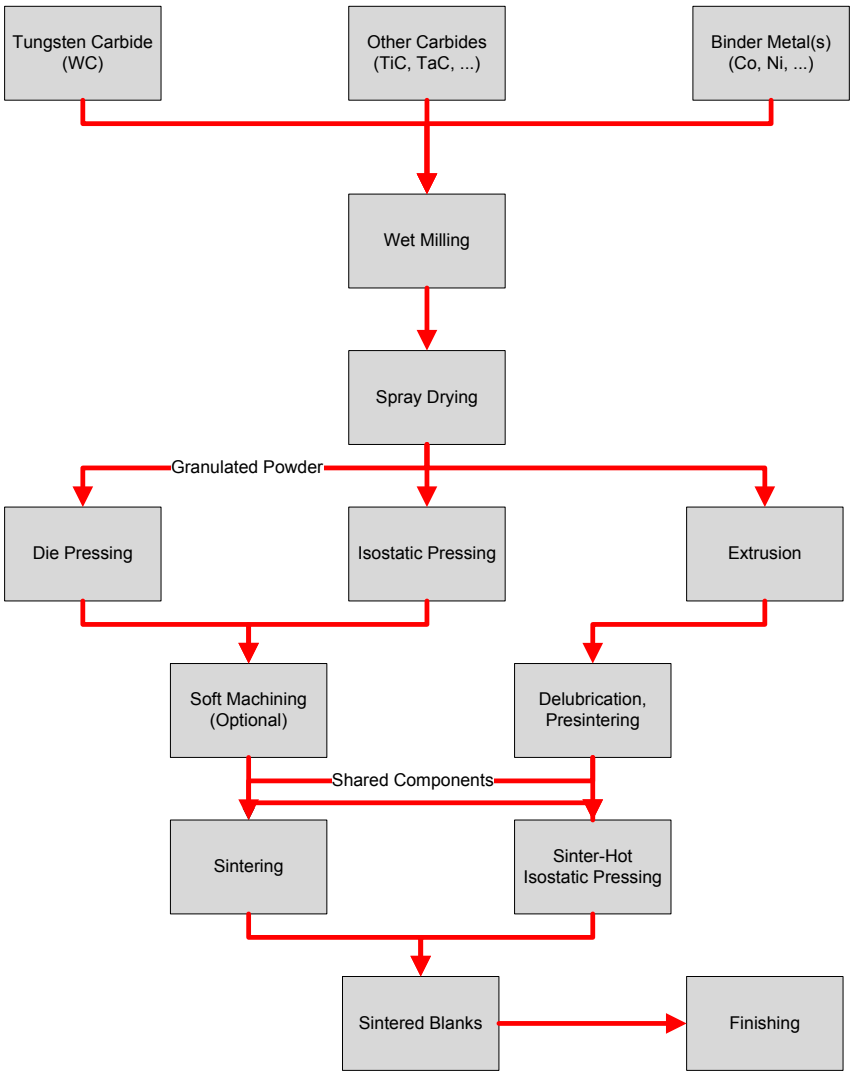

Figure 2.10: Schematic for the production of hardmetals (Cemented carbide) (adapted from [***38***])

The sintering process, performed as liquid phase sintering, is done at temperatures varying between 1400°C and 1600°C [***1***,***41***] or even higher for certain compositions containing materials including, titanium, tantalum, niobium and low contents of cobalt. The temperature varies as the composition varies. [***20***] The liquid phase sintering at these temperatures with an adequate amount of binder as well as a not too large grain size allow for a pore-free body [***41***]. Other factors that affect the properties of cermets are the grain size of the hard element and also the composition and percentage of the binder. The material becomes tougher or less brittle, the higher the proportion of binder material. By increasing the proportion of binder, there will generally be a decrease in hardness [***1***,***41***], density, and wear resistance of the material. In saying this it shows there is a trade-off between hardness and toughness or resistance to impact damage [***1***]. As shown in Figure 2.11 a compromise must be achieved between wear resistance and toughness through variations of the amount of binder phase. From the figure it can be seen that binder content has an influence on wear resistance. The figure also depicts that with less binder phase the carbide becomes more brittle [***20***]. The shrinkage that takes the material to full density is normally half the volume of the green compact.

Heterogeneous shrinkage is caused by spatial variation in green-compact properties like relative density. These factors must be taken into account when tools and parts are manufactured. [***41***]

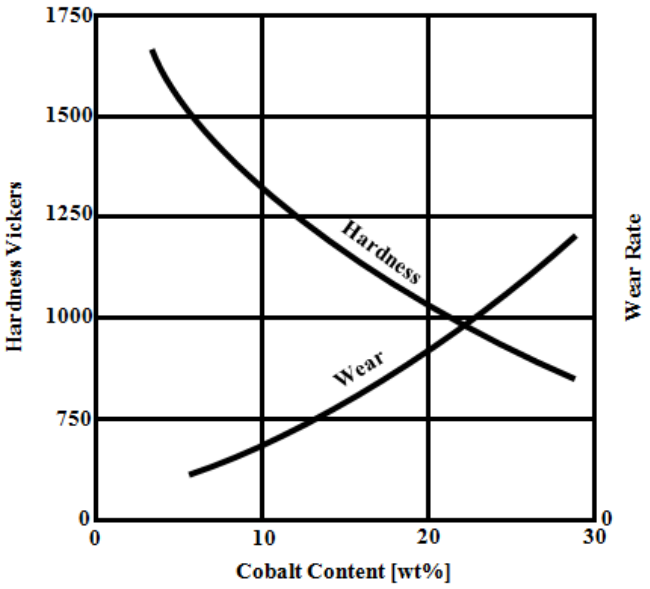

Figure 2.11: Relationship between cobalt content, hardness and wear of WC-Co(adapted from [***20***])

2.4.2 Spark Plasma Sintering

Spark plasma sintering (SPS) or pulse electric current sintering (PECS) is a technique that allows for rapid densification results with minimal grain growth in a short time. In industrial application where it is difficult to obtain high performance materials, SPS processing is utilized [***47***]. According to Mamedov [***47***] significantly more research is required in this field for extensive industrial application.

The process consists of pulsed electrical current combined with rapid heating and pressure to complete final sintering in a short time. Figure 2.12 depicts the basic process of SPS. As shown in the figure the powders are loaded into a graphite die, because the die is made of graphite the applied pressure is limited to a maximum of 100 MPa. This limit also applies to the punches as graphite is used in their construction. [***47***]

Rapid heating, and cooling rates, short sintering time and controllable pressure are advantages that the SPS method has over conventional sintering methods [***48***]. According to Zhao [***48***], WC-Co materials were found to have good hardness and toughness that were sintered using the SPS method [***48***]. Ostwald ripening causes WC grain growth during liquid phase sintering. High temperatures and long holding times cause the dissolution-reprecipitation procedures and this is when considerable grain growth occurs [***48***]. The SPS method is able to reduce these times considerably compared to that of conventional sintering and thus reduce grain growth.

Sintering environments differ for specific applications and commonly used environments are vacuum, argon, hydrogen, or air environments. An electric pulse is applied and the densification process takes place. The

pulse has values of 30 V and 600 – 1000 A and lasts between 1 – 300 ms. Densification is achieved through the application of external pressure. The pressure is able to remain constant or can take a gradual increase throughout the process. [***47***]

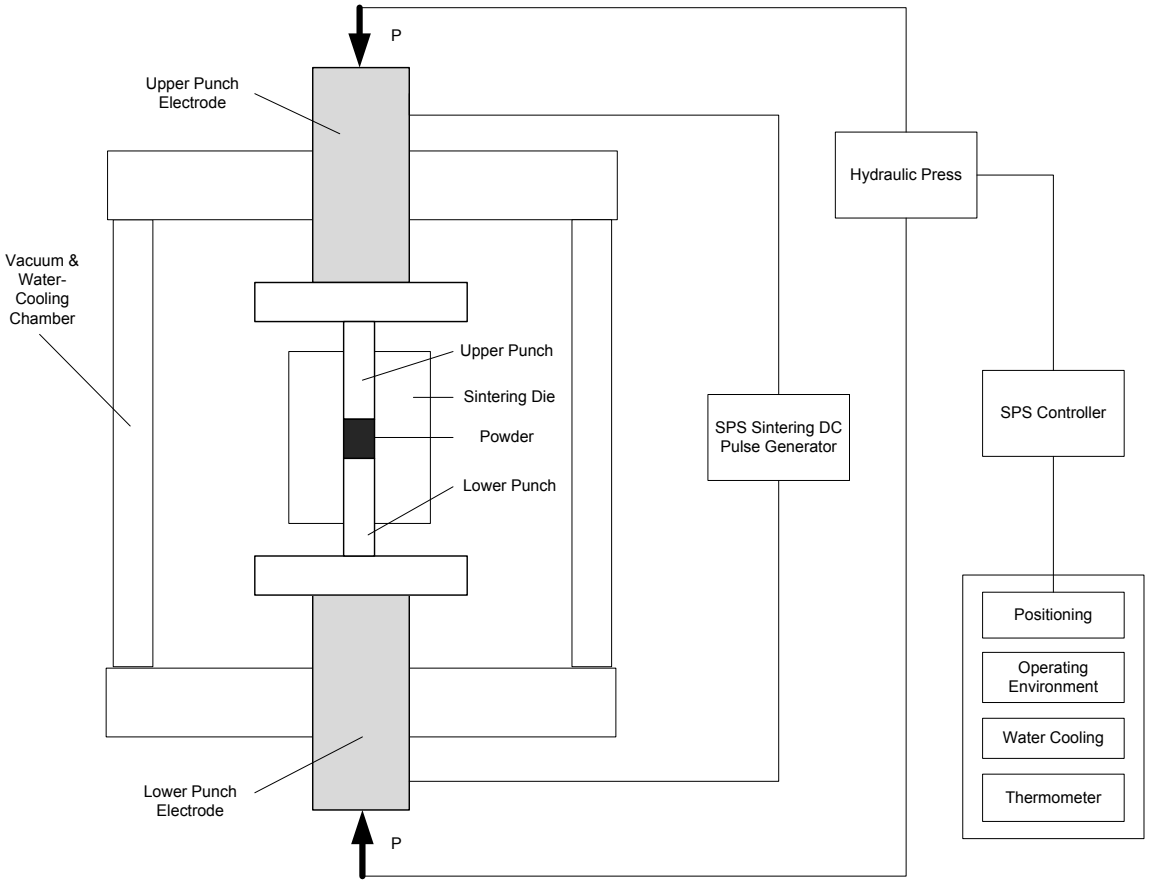

Figure 2.12: Basic process of Spark Plasma Sintering (adapted from [***47***])

2.4.3 Material Properties & Characterization

Cemented carbides possess certain properties that make them promising materials for new uses in various technology fields. These materials have high melting temperature, high chemical resistance, electrical and thermal conductivities of a metallic character and have great hardness. [***40***] The melting point of tungsten carbide is between 2600°C and 2850°C. The material has high hardness, high fracture toughness ($28 MPa.m^{1/2}$) and is the hardest binary carbide at elevated temperatures (~1000 kg/mm^2 at 1000°C). The material shows high resistance to oxidation and corrosion and as a high compressive strength (5GPa at 20°C) [***40***]. Table 2.3 below includes certain properties of cobalt-bonded tungsten carbide. Different grades of this material are available on the market.

Table 2.3: Properties of cobalt-bonded tungsten carbide (WC) [***1***]

Property	Unit	Cobalt-bonded tungsten carbide
Elastic Modulus [E]	GPa	~450 – 650
Poisson's Ratio [υ]		0.22
Vickers Hardness [H_V]	GPa	~13 – 18
Density [ρ]	$kg.m^3 \times 10^3$	~13 – 15

WC, which is known as the hard phase makes up the largest proportion of a cemented carbide. The proportion within a specific composition can range from 99wt% to 70wt%. The crystal structure is a hexagonal close-packed (HCP) single crystal. For this reason the hardness of tungsten carbide materials is dependent on the crystal structure [***49***,***50***]. Figure 2.13 is a SEM micrograph of the WC-Co material. The dark parts are the cobalt binder and the bright areas are WC.

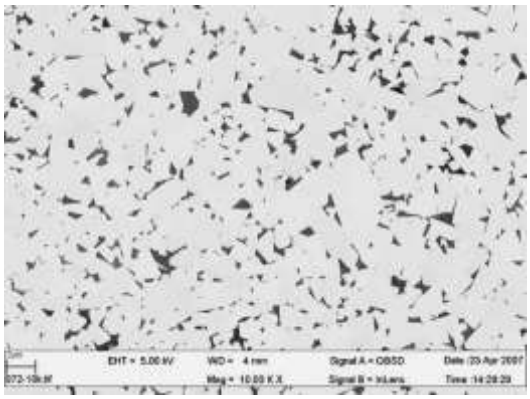

Figure 2.13: SEM micrograph of the WC-Co material [***42***]

Hardness of these materials is between $1300H_V$ to $2300H_V$ and depends on the grain size. Cemented carbides with a finer grain generally are harder than those containing more coarse grains. Table 2.4 contains the range of values of grain sizes. [***49***,***50***]

Table 2.4: Grain size found in cemented carbides [***49***]

Type	Grain Size
Ultra-Fine	< 0.5 µm
Medium	1.4 – 2 µm
Extra Coarse	>5 µm

Coated carbide tools are used in various applications due to their high wear resistance. In machining it is of paramount importance to have quality lubrication at the tool-chip and tool-workpiece interfaces. It is also important to reduce temperatures and friction at the cutting edge. Coated carbide tools provide improved

lubrication at the above mentioned interfaces. These coated tools are also able to produce lower temperature, lower cutting forces and higher wear resistance. For these reasons coated carbides outperform uncoated carbides [***51***].

2.5 Inconel 718

The material is used in aircraft engines because of high temperature properties, corrosion resistance, and high strength-to-weight ratio. The Nickel-based alloys account for about 50wt% of the superalloy usage in an aerospace engine. Inconel 718 accounts for 25% of the production of cast products and 45% of the annual production wrought nickel-based alloys [***8***]. The alloys are also used in industries such as the marine, nuclear, pertrochemical and food processing. [***52***]

There are also many uses for these superalloys that are used to manufacture equipment for industries. These industries include electronics, defence, dental, orthopaedic and paper and pulp [***53***].

Superalloys can be broken up into three groups, iron-nickel-base, nickel-base and cobalt-base [***8***,***54***]. The descriptions and examples of these categories are listed below. For a full list of the different alloys in each category refer to [***8***,***55***].

- Iron-Nickel Based
  These alloys are strengthened by intermetallic compound precipitation in an austenitic fcc matrix. The alloys are used in the wrought condition.

  Alloys: Inconel 718, Inconel 601, Inconel 617

- Nickel-Bases
  These alloys are strengthened by intermetallic compound precipitation in an fcc matrix. The alloys are used in both the cast and wrought condition.

  Alloys: Incoloy 800, Incoloy 827, Haynes 556

- Cobalt Based
  These alloys are strengthened by a combination of carbides and solid solution hardners.

  Alloys: Haynes 188, Elgiloy, Stellite 6B

The Inconel alloy chosen for the experiments is Inconel 718. This superalloy falls into the nickel-base category [***8***]. Inconel plays an important role in the manufacture of jet aeroengines due to its high-strength, thermal-resistance (HSTR). This Nickel-based alloy is known for its exceptional corrosion resistance [***56***].

Other important properties are its oxidation-resistance, and that it can be used in environments with temperatures in the range of -217°C – 700°C. The material is also non-magnetic. [***57***]. The hardness of the material is 412 H_V [***58***] and has a density of 8.47g/cm^3 [***58***]. The chemical composition of the material is shown in Table 2.5.

Table 2.5: Composition of Inconel 718 [***59***]

C	**Mn**	**Si**	**Ti**	**Al**	**Co**	**Mo**	**Nb**	**Fe**	**Cr**	**Ni**
0.08	0.35	0.35	0.6	0.8	1	3	5	17	19	52.82

2.6 Conclusion

The literature study discusses many of the aspects that are involved in the thesis. The study is used as background to the different studies conducted. The forms and mechanics behind friction and sliding wear were discussed in detail as these two topics are of paramount importance to the project. A large part of the project is dedicated to carbides and especially SPS carbides. The metal alloys that are discussed are used in a study of sliding wear in the aerospace industry.

3. Materials & Methods

The materials and methods chapter discusses the different methods used for obtaining results in the proceeding chapter. In the chapter three distinct sections are discussed. The first section discusses the different mechanical and material characterization techniques used to evaluate the SPS carbide materials. The next section discussed the sliding apparatus and its design. The last two sections discuss the sliding experiments and the equipment used to obtain results.

3.1 SPS Carbides

The market is currently dominated by cobalt that is being utilised as a binder. When compared to cobalt, nickel is being used as an alternative binder to a much smaller extent. Nickel as a binder is only used for very specialized applications where there is a need for high thermal cracking resistance or corrosion resistance. The need for materials with a nickel binder relates to the drawbacks that cobalt possesses. Cobalt's disadvantages relate to its hexagonal close-pack structure and the fluctuations in the market price. [***60***]

According to Almond [***61***], WC-Ni materials have lower hardness and fracture toughness than WC-Co materials [***61***]. It was noted by Guo [***62***], that WC-Ni carbides have lower hardness than those that have a Co binder. The lower hardness and the inferior properties of WC-Ni carbides can possibly be due to higher percentage plastics as well as the absence of β-α phase transition of the Ni binder. This is possibly one of the reasons why WC-Ni carbides have restricted use in applications [***62***].

Niobium carbide has many promising properties and so is used in the manufacturing of refractory carbides. The material has a high melting point 3600°C, a density of 7.79g/cm^3, a Vickers hardness of 19.6GPa, and a Young's modulus of 338-580GPa. Comparing the density of WC (15.68g/cm^3), to that of Niobium carbide, it can be seen that the later density is close to half of that of WC. [***63***]

NbC-Co hardmetals showed notable grain growth when pressure less sintering was done for 1 hour at 1360°C. This grain growth can be suppressed by using spark plasma sintering (SPS). These materials have shown that they do not possess the same application potential as WC-Co based hardmetals and this could be due to their relatively low hardness and fracture toughness. [***64***]

By reducing the grain size of WC cemented carbide the strength, hardness and wear resistance can be improved [***65***]. NbC is a poorly sinterable material and SPS is a possible method to address this problem. The low temperature and short holding time can suppress the grain growth within the carbide material [***66***]. Due to the high solubility and mobility of Cr_3C_2 at low temperatures within the cobalt phase, it is a very

effective grain growth inhibitor. Grain growth inhabitation can be related to the slowing down of the solution/re-precipitation reactions at the WC-Co interfaces [***65***].

Haung [***64***], describes a decrease in hardness with an increase of NbC content in a material [***64***]. The literature attributes the decrease in hardness to the WC-Co fraction decreasing. It is also important to note that a smaller grain size means a harder material [***42***].

TiC has proven that it is an effective grain growth inhibitor. The hardness of the material increases with additive, but reaches a maximum were it has no further affect. [***60***] Data for the solubility of TiC in Ni is scarce [***67***]. According to Wittmann et al [***67***], a 0.2wt% TiC addition showed low solubility in Ni. In addition to this plate like WC structures are formed that are imbedded within a smaller WC fine-grain matrix. These forms are depicted in Figure 3.1 taken at a magnification of 4000X.

Mo_2C has been shown to increase the wettability between the hard phase (TiC) and binder phase (Ni). The same hardness as WC-Co carbides can be achieved using Mo with a Ni binder. [***60***] Mo has been shown to act as a grain growth inhibitor in materials with a Ni binder [***67***].

In the results, TiC and Mo_2C additives are discussed. These additives are used to attempt to enhance the properties of Ni-bonded cemented carbides.

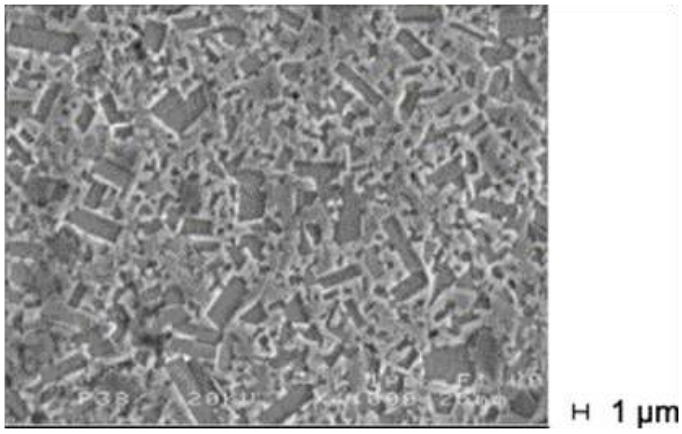

Figure 3.1: Microstructure of a WC–1wt%TiC–10wt%Ni material; sintered at 1480 °C for 1 h; magnification: 4000X [***67***]

A study was conducted to ascertain the mechanical- and elastic properties as well as the material characterization of specific SPS carbides. The materials were manufactured at the Department of Materials and Environmental Chemistry, Stockholm University, Sweden. The goal of the study was to determine if these carbides are comparable to carbides manufactured through conventional methods and to assess if using a Nickel binder is feasible.

Table 3.1 and Table 3.2 describe the powders and the sintering process used to create the materials used in this study.

Table 3.1: Original powders used to produce the SP carbides (Stockholm University)

Materials	**Particle Size [µm]**	**Purity [%]**	**Supplier**
WC	1.2	>99	H. C. Starck GmbH Germany
NbC	< 10	>99	Alfa Aesar USA
TiC	1.4	>99.5	Alfa Aesar USA
Mo_2C	44	>99	Alfa Aesar USA
Co	1.6	~99.8	Alfa Aesar USA
Ni	10	>99.5	Sigma Aldrich

Table 3.2: Sintering process for original SPS carbides (Stockholm University)

Composition	**PCP Consolidation Temperature (°C)**	**Heating Rate (°C/min)**	**Pressure (MPa)**	**Holding Time (min)**
WC-1%NbC-10%Co	1140°C	200 °C/min to 600°C then 108 °C/min to 1140°C	50	5
WC-3%NbC-10%Co	1140°C	200 °C/min to 600°C then 108 °C/min to 1140°C	50	5
WC-10%NbC-10%Co	1140°C	200 °C/min to 600°C then 108 °C/min to 1140°C	50	5
WC-6.25%TiC-9.3%Ni	1140°C	200 °C/min to 600°C then 108 °C/min to 1140°C	50	5
WC-6.25%TiC-9.3%Ni-3.5%Mo_2C	1140°C	200 °C/min to 600°C then 108 °C/min to 1140°C	50	5

The original materials and their quantity that were received from the suppliers are listed in Table 3.3. Table 3.4 is the list of samples and their reference numbers after EDM cutting was completed.

Table 3.3: Materials and composition after sintering

Original Materials and Composition	Quantity
WC – 10wt%Co – 1wt%NbC	3
WC – 10wt%Co – 3wt%NbC	1
WC – 10wt%Co – 10wt%NbC – 0.3wt%Cr_3C_2	2
WC – 9.3wt%Ni – 6.25wt%TiC	1
WC – 9.3wt%Ni – 6.25wt%TiC – 3.5wt%Mo2C	1

Table 3.4: Reference Number and composition of materials after EDM

Reference Number	Original Materials and Composition
1.1	WC – 10wt%Co – 1wt%NbC
1.2	WC – 10wt%Co – 1wt%NbC
1.3.1*	WC – 10wt%Co – 1wt%NbC - 0.3wt%Cr_3C_2
1.3.2*	WC – 10wt%Co – 1wt%NbC - 0.3wt%Cr_3C_2
1.4	WC – 10wt%Co – 3wt%NbC - 0.3wt%Cr_3C_2
1.5.1*	WC – 10wt%Co – 10wt%NbC - 0.3wt%Cr_3C_2
1.5.2*	WC – 10wt%Co – 10wt%NbC - 0.3wt%Cr_3C_2
1.5.3*	WC – 10wt%Co – 10wt%NbC - 0.3wt%Cr_3C_2
1.5.4*	WC – 10wt%Co – 10wt%NbC - 0.3wt%Cr_3C_2
3.1	WC – 9.3wt%Ni – 6.25wt%TiC
3.2	WC – 9.3wt%Ni – 6.25wt%TiC – 3.5wt%Mo_2C

* Materials with triple digit reference numbers have been cut in two. E.g. 1.3.1 and 1.3.2

Specific equipment was used to prepare the carbide materials for the microstructural and mechanical characterization. The preparation equipment is listed in Table 3.5. After sintering the carbide material was coated in graphite that has been released from the dies. This coating was removed through use of grinding equipment. Once the carbide was exposed, the thicker samples were cut in half. The reason for this was that only a few samples were manufactured and the amount of samples had to be maximized. The carbides were moulded into a thermo-plastic setting resin and lapping took place to remove the largest marks and make the two surfaces parallel to each other. Lapping speeds varied between 30 and 60 m/s. Once the lapping was completed, the materials were polished. The polishing procedure is listed in Table 3.6. The polishing of the materials is very important as many of the materials tests cannot be performed on an unpolished surface, for example Vickers Hardness.

Table 3.5: Material preparation equipment

Machinery/Equipment	Purpose
Fanuc Robocut α-oíA (EDM) with Fanuc Series 18í-W software	Cutting carbides
Leco PR 32	Thermo-plastic setting
Peter Wolters 3R380-GR	Lapping
Imptech 20DVT Grinder Polisher	Grinding/Polishing

Table 3.6: Polishing procedure for cemented carbides using the Imptech 20DVT Grinder Polisher

Wheel/Abrasive Medium	Lubricant	Sample Rotation [CW/ACW]*	Pressure/Force [kPa]	Wheel Speed [rpm]	Time [min]
Grinding					
Resin bonded diamond wheel	Water	ACW	Fixed at 225kPa	100	10
Polishing					
Metlap pattern - 9 µm	9 µm slurry	CW	Fixed at 225kPa	120	5
Metlap Pattern - 6 µm	6 µm slurry	CW		120	5
Metlap Perforated - 6µm	6 µm slurry	ACW		200	5
Lecloth - 1 µm	1 µm slurry	ACW		250	3

* CW – Clockwise rotation and ACW – Anti- clockwise rotation

The following equipment was used to measure the mechanical- and elastic properties of the SPS carbides are listed in Table 3.7.

Table 3.7: Equipment used to determine mechanical and elastic properties

Machinery/Equipment	Purpose
Vickers' Hardness machine – Crayford Kent	Determine hardness and fracture toughness
Mass balance scale – Vibra	Determine density
Krautkramer Branson USIP 12	Speed of sound – elastic properties
Forster-Koerzimat CS 1.096	Obtain Coercivity values
Magnetic saturation machine	Obtain Magnetic saturation values

Hardness and fracture toughness are very important as these two properties are used to judge what materials should be used in a specific application. Hardness is defined by Groover [***68***] as "*its resistance to permanent indentation"*. In general, this is a measure of how scratch and wear resistant a material is.

For hardness and fracture toughness measurements a load of 30kg's and a diamond pyramid indenter were used. The indenter was used to indent the material and then the indented diagonals were measured as depicted in Figure 3.2. The values are inserted into equation 3.1 where H_V is the Vickers Hardness, N is the applied load (kg), and D is the length of the diagonal of the impression (mm). [***68***]

$$H_V = \frac{1.854N}{D^2} \qquad 3.1$$

Equation 3.2 states a value with a unit of $kg.mm^2$ that can be converted to GPa. Equation 9 is used to convert the Vickers Hardness (H_V) to Hardness with a unit of GPa.

$$Hardness(GPa) = \frac{9.8}{1000} Vickers Hardness(H_V) \qquad 3.2$$

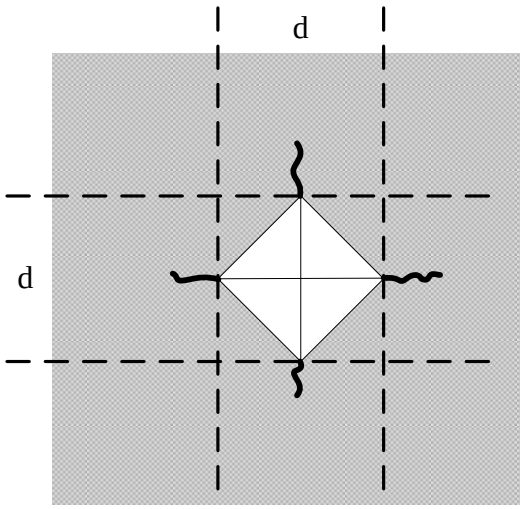

Figure 3.2: Vickers Hardness indentation showing how the diagonals are measured

Fracture toughness is the measure of a material to resist brittle fracture when a crack is present [***25***]. The fracture toughness was measured during the hardness tests with the same machine. The crack lengths were measured that originated at the corners of the Vickers indentation. Equation 3.3 (Shetty equation) was used. H_V is the hardness, N is the indentation load, and l is the crack length. There are two ratios to take into account when using the equation; they are c/a and l/a ratios. Figure 3.3 depicts the Vickers hardness indentation and how the cracks are measured. 2a is the diagonal measurement of the indent and 2c is the measurement of the crack length. [***69***]

$$K_{1C} = 0.0889\left(\frac{H_V N}{4l}\right)^{1/2} \quad 3.3$$

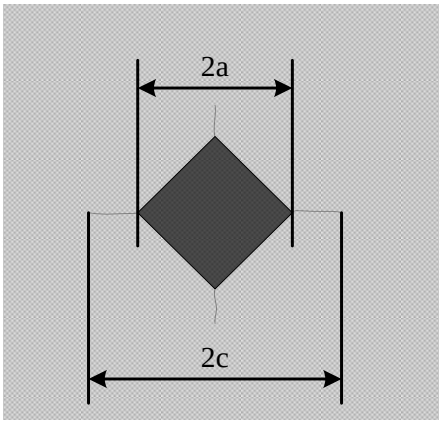

Figure 3.3: Vickers hardness indentation and annotations describing the method to determine fracture toughness

Young's modulus (E) is also known as the modulus elasticity and is defined by the ASM Handbook Volume 8 [***70***] as the *"measure of rigidity or stiffness of a metal; the ratio of stress, below the proportional limit, to the corresponding strain"* [***70***]. The value of E was calculated using a Speed of Sound Machine. The longitudinal speed of sound (υ_L) and the transverse speed of sound (υ_T) are measured. The values are combined in the following equations. Equation 3.4 is used to calculate Poissson's ratio (υ). Equation 3.5 is used to calculate the Shear Modulus (G). Combining these two values gives the Young's Modulus of the carbide material as shown in equation 3.6.

$$\mu = \frac{\nu_L^2 \quad 2\nu_T^2}{2(\nu_L^2 \quad \nu_T^2)} \quad 3.4$$

$$G = \rho \nu_T^2 \quad 3.5$$

$$E = 2G(1+\nu) \quad 3.6$$

According to Roebuck [***71***], magnetic saturation is the term used to describe "*the saturation (maximum) value of magnetic induction that can be obtained in a test piece in a strong magnetic field"* [***71***]. Cobalt is ferromagnetic and is contained in certain hardmetals as a binder. For this reason the measurement of magnetic properties can be very valuable to ascertain certain properties instead of using destructive experimental procedures. The binder phase in the materials contains tungsten and carbon in solution. To assess how much tungsten has dissolved into the cobalt-binder phase magnetic saturation can be used. The

saturation of cobalt decreases linearly with the addition of tungsten. Carbon has no effect on the saturation value when dissolved in solution [***71***].

Depending on the grain size of the material, with large grains the coercivity value is small and vice versa for small grains. The values are inversely proportional. Coercivity is the intensity of a magnetic field that is needed to reduce the magnetization of a ferromagnetic material (cobalt) to zero after it has reached saturation (maximum). To obtain the coercivity value for the WC-Co carbides, a Forster-Koerzimat CS 1.096 was used. The units for coercivity are Ka/m and the term is donated by the symbol H_c.

The material microstrucural characterization was done using the equipment listed in Table 3.8. For the material characterization, two different SEM's were used because of technical difficulties. The two different machines are listed in Table 3.8. The SEM was used for material characterization and EDS analysis. EDS is a non-destructive technique that is used as an elemental qualitative analytical tool [***72***]. The images and EDS analysis allowed for a better understanding of the material. Area and spot analysis was done.

XRD is a non-destructive technique that is used in material characterization to identify phases present in samples [***72***]. The XRD tests for the samples were conducted on a Philips X'Pert with a Cobalt tube instead of a Copper tube.

XRF is a non-destructive emission spectroscopic technique used to determine what elements are present within a sample. The measurement is quantitative and for the results in this report are in wt%. [***72***]

Table 3.8: Equipment used for material characterization

Machinery/Equipment	**Software**	**Purpose**
Philips XL30 ESEM-FEG	EDAX Genesis Imaging/Mapping Version 4.52	Analyze content, composition of carbides (SEM)
Joel JSM-7500F Field Transmission SEM	Microanalysis Suite Issue 17b with Inca Suite Version 4.09	Analyze content, composition of carbide samples (SEM)
Philips X'Pert (Cobalt tube)	X'Pert Highscore plus 2.1b	Identify phases in carbide (XRD)
Philips PW2400 X-Ray	SuperQ XRF Measure & Analyze and IQ+ 3.0k	Determine elements present in carbide samples (XRF)

3.2 Sliding Apparatus

The Sliding Apparatus depicted in Figure 3.4 below is based on a machine used by the Brunel University in London, UK. The design was decided upon because it was a more robust design and for this reason would last longer [***73***]. The test apparatus was designed partially by a student, E.Oosthuizen, as part of her final year project, under supervision of N.Treurnicht from the Department of Industrial Engineering and G.Akdogan from the Department of Process Engineering at Stellenbosch University.

The original apparatus consists of a test table, rotating arm, motor, weight and counterweight all mounted on a steel table that can be bolted to a floor to ensure stability. A worm gear and motor (Figure 3.4 d) are positioned below the machine at an angle of 90° degrees to the table top. This in turn drives a shaft that connects to a crankshaft at 90°. Through a crank mechanism the motor is able to move the table forward and backward, thus creating the sliding motion needed for testing. A link exists between the rotating shaft and the sliding interface and is shown in Figure 3.4 b) and c). The displacement of the table can be adjusted through two screws moving in slots on the crank arm. The table allows for a plate to be mounted and the chuck above it allows for a rod to be clamped. The materials then slide against each other. To create the normal force, a weight and counterweight system is used, shown in Figure 3.4 a). [***73***]

Two load cells are mounted to measure the friction forces that take place; both load cells are shown in Figure 3.4 c) and have been circled. These load cells are connected to an amplifier, which in turn is connected to a computer, thus the load cell readings are recorded to be presented graphically [***73***]. The load cell that is on the crank mechanism moves with the forward and backward motion. This was found to be a problem, as the load cell's reading had a dynamic component that was not wanted. The issue was resolved by placing the load cell in such a way that it did not move with the crank mechanism. It still needed to have the ability to measure the friction.

The 3-phase motor's speed was controlled an AC drive. The top speed of the AC drive is 50 Hz, and which is equal to 50 rpm.

a)

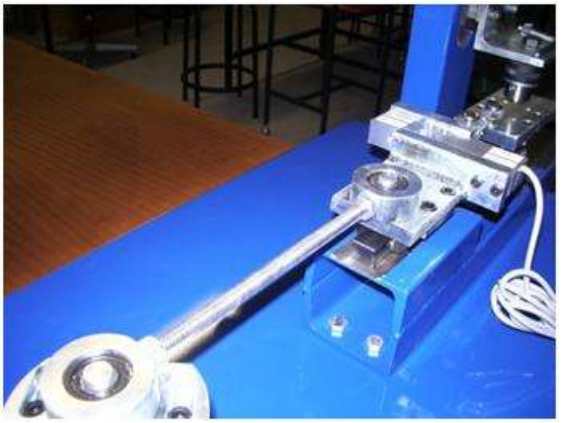

b)

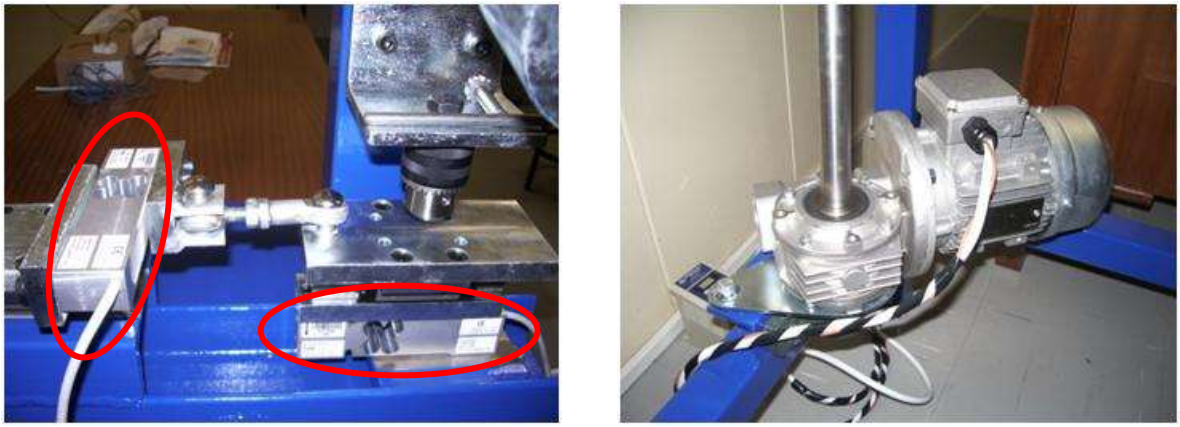

c) d)

Figure 3.4: Original sliding apparatus before new design

a) front view; b) crank mechanism; c) load cells; d) 3-phase motor

3.2.1 Design

As described previously there was a need to move the load cell that measures the tangential force. Different conceptual designs were considered, but for the purpose of this report, the following will describe the final design that was decided upon.

Figure 3.5 illustrates an exploded CAD view of new parts designed to move the load cell (G). To be able to place the component at the specific position new links had to be created. Figure 3.6 are images taken of the apparatus after the load cell was moved. In both figures the components are labelled from A to H and these letters are referred to when the specific component is discussed.

From Figure 3.5 and Figure 3.6 it is seen that the existing linear bearing (A) was bolted to the vertical stand in a position parallel to the base plate. A connection block (B) was added to this to hold the load cell that measures the tangential force. Connected to the block is a pillo-ball (F) that links the load cell (G) to the block. The pillo-ball and load cell are connected by a connecting block (H). The connecting block looks rectangular except with a piece cut-out to allow for the pillo-ball to connect. The load cell is in turn connected to the vertical stand through two plates (E), creating a linkage. Connected to the block is another linear bearing at an angle of 90° (C) to the previous mentioned linear bearing. This linear bearing was installed so that the weight and counter-weight system could move up and down. Connected to the previously mentioned linear bearing, is another steel block (D) that holds the chuck used for clamping the pin specimen. As can be seen from the images and the illustration, the new design stands out further from the vertical stand (I) than the original. The solution to this problem was to place spacers on the vertical stand so that the chuck and the platform aligned.

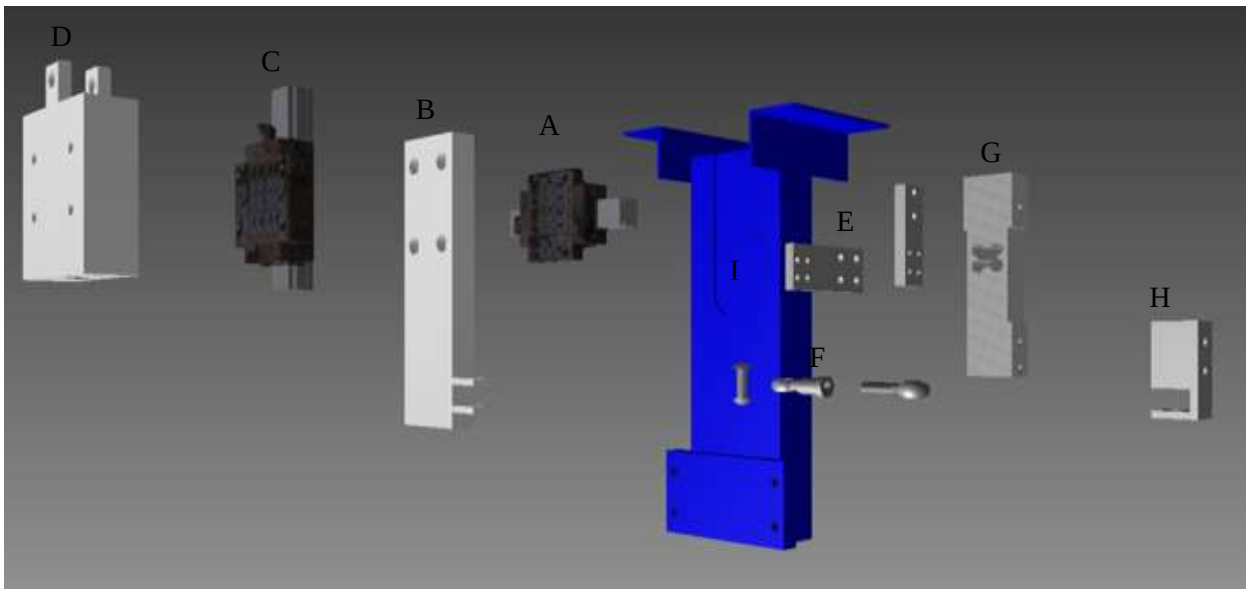

Figure 3.5: CAD view of the new components

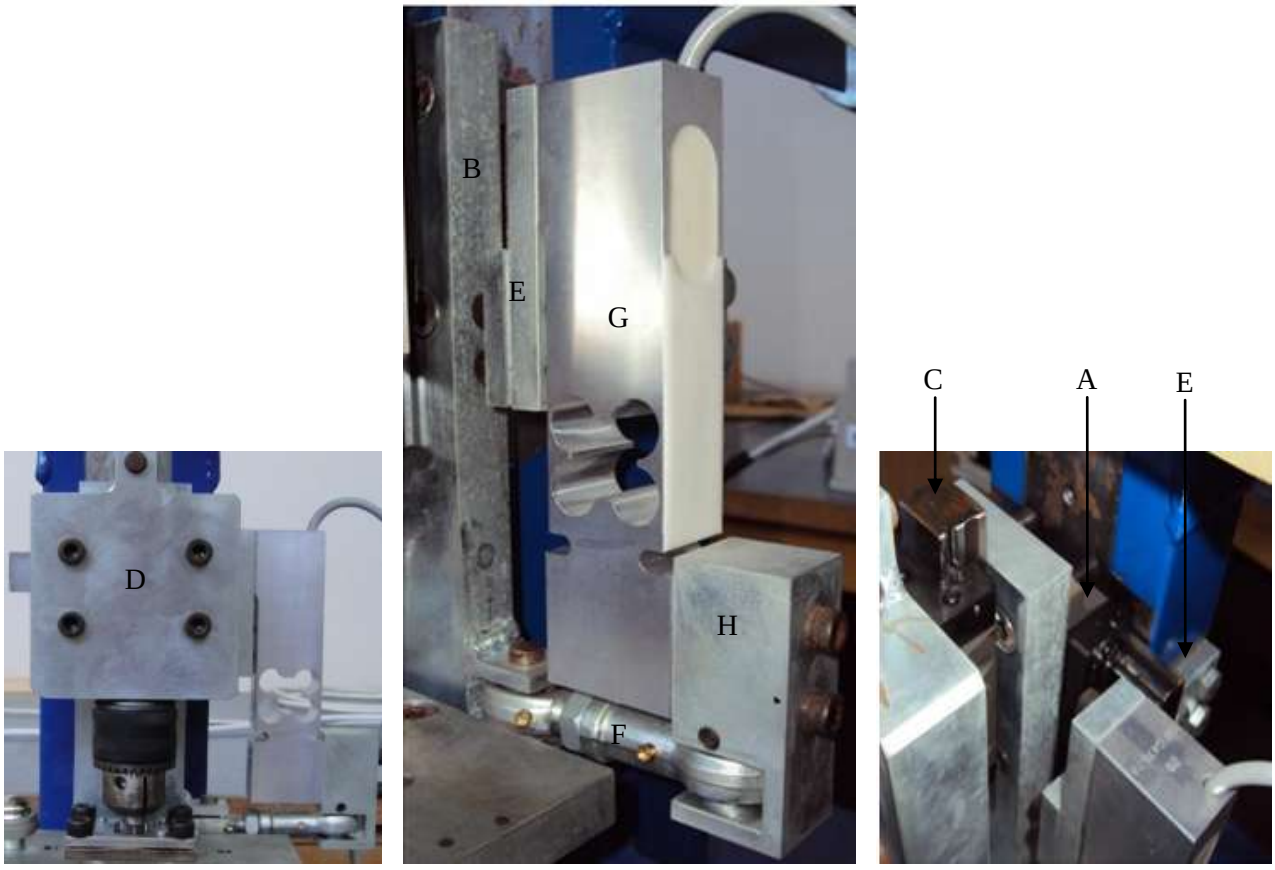

Figure 3.6: Pictures showing the new position of the load cell measuring the tangential force

A link was created were the load cell measuring the tangential force was removed. To do this a threaded rod was inserted between the two ends of the pillo-ball. This was an easier design as the existing parts of the machine could be used and are shown in Figure 3.7.

Figure 3.7: Image depicting the new linkage

3.2.2 Operation of Sliding Apparatus after New Design

The apparatus has the ability to measure the normal- and tangential forces when the machine is running. The 3-phase worm gear motor with a shaft connected to it was used to drive two linear bearings causing a platform to move in a linear reciprocating motion. The linkage discussed in the previous section connects the two linear bearings. On the platform, the clamping system is attached for the flat specimen and above this is the chuck holding the pin specimen. This part of the apparatus is the sliding interface. A sophisticated logging device is used to read tangential loads and displacement amplitude. Figure 3.8 is a detailed schematic of the sliding interface shown as a section view.

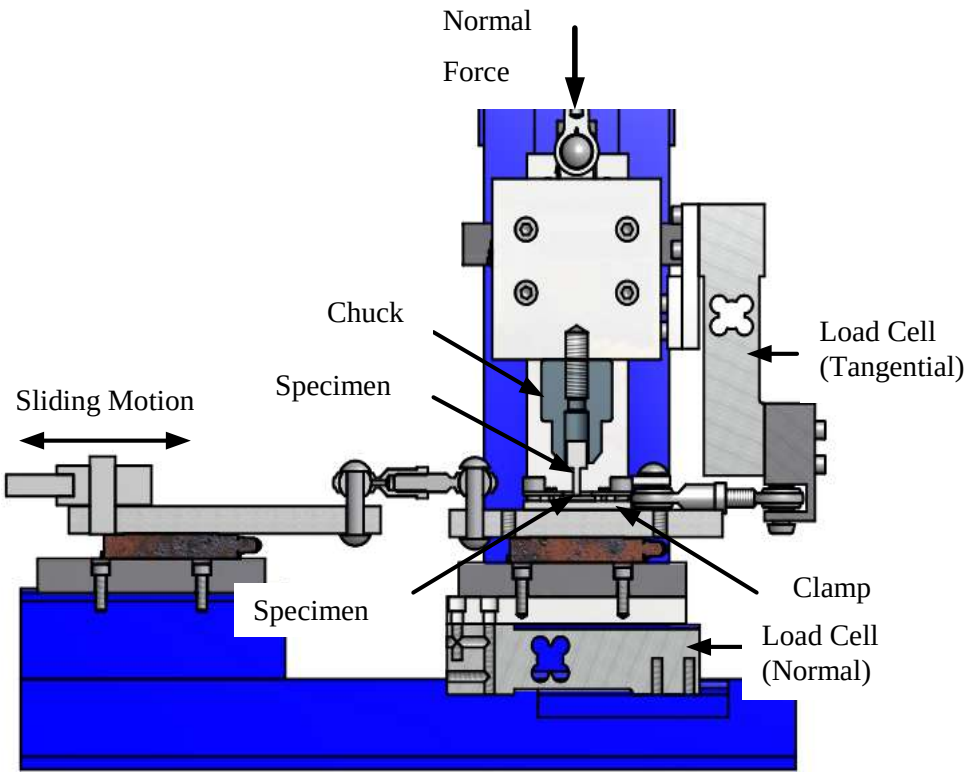

Figure 3.8: Section view of the sliding interface

Table 3.9 describes the different parameters on the apparatus and their minimum and maximum values. The motor speed specified in Table 3 is converted to average sliding speed (m/s) and this value depends on the peak-to-peak amplitude that is used.

Table 3.9: Parameter variations for the sliding apparatus

Specification	Variable	Variation
Amplitude (peak-to-peak) [mm]	δ	0 – 35
Normal load [N]	N	0 – 196
Motor Speed [rpm]	ω	0 – 50
Sliding distance [m]	S	Fully adjustable
Sliding configuration		Various

The apparatus has been divided into different sub-assemblies and each is discussed in turn.

- **Clamping Systems and Material Specimen Geometries**

To hold the different specimens two clamping systems were used. The two systems are depicted in Figure 3.9 and the clamping system used for flat specimens is illustrated using CAD in Figure 3.10. The chuck (a) was used to clamp the different geometries as shown in Figure 3.11. For most of the experiments, a flat pin (b) was used, but as shown in later sections a round pin (b) was also used. The second clamping system (b) was used to hold the flat specimens. The two systems can hold a variety of tool geometries.

a) b)

Figure 3.9: Clamping systems a) chuck holding pin and b) clamp holding flat specimen

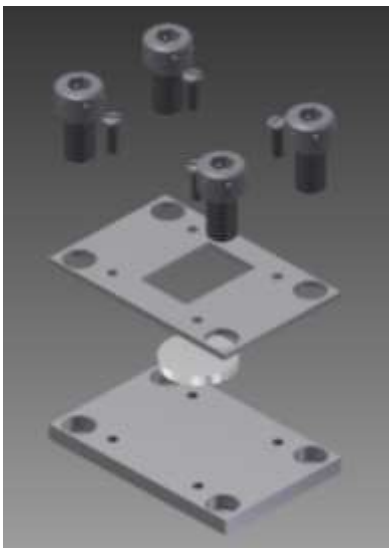

Figure 3.10: Exploded CAD view of the clamp system for the flat specimen

a) b)

Figure 3.11: Different pin geometries a) flat pin and b) round pin

- **Drive System & Speed Control**

The drive system for the sliding apparatus is shown in Figure 3.12. A geared motor is positioned below the machine at an angle of 90° to the tabletop. This in turn drives a shaft that connects to a crankshaft at 90°. The shaft is linked to the first of two tables that slide on linear bearings. An AC speed controller is used to change the speed of the machine, and this allows for different sliding speeds. The AC speed controller allows for a maximum motor speed of 50 rpm and increase/decreases in values of 0.01. The different sliding amplitudes can be set by adjusting two screws on the top of the crank mechanism that move in slots. The worm geared motor and AC drive are listed in Table 3.10. The specifications of each component of the electric drive system can be found in [***74,75***]. The speed (rpm) of the motor can be converted to m/s, but the value differs for different sliding amplitudes.

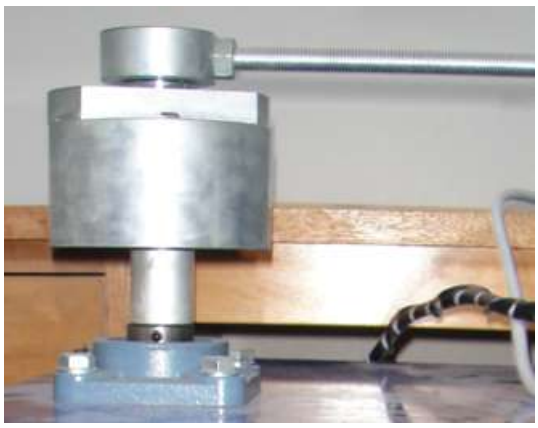

a)

b)

c)

Figure 3.12: Drive system for sliding apparatus a) & b) drive system with geared motor and c) AC drive system (speed controller)

Table 3.10: Electronic and mechanical drive system components [***74,75***]

Type	**Manufacturer**	**Specification**	**Amount**
Motor	Bonifiglioli	EML 220 V, 1370 rpm	1
Worm Gear	Bonifiglioli	VF 49 P (24:1)	1
AC drive	Bonifiglioli	Vectron Synthesis (SYN10 220 03 AF)	1

- **Weight & Counterweight System**

The weight and counterweight system is used to create the normal force used in the sliding interface. It can be adjusted for a specific force by moving the weights around. The limitation of the system is that the load cells are only rated for a maximum load of 20kg (196N). The system is depicted in Figure 3.4 a).

- **Measurement System**

As shown in fig there are two load cells. The one is used to measure the normal force (1) and the other the tangential force (2). As described in section 3.2.1, the load cell was moved to a stationery position closer to

the two clamping systems. The load cells are rated to take a maximum load of 20kg (196N) and specifications are described in Table 3.11.

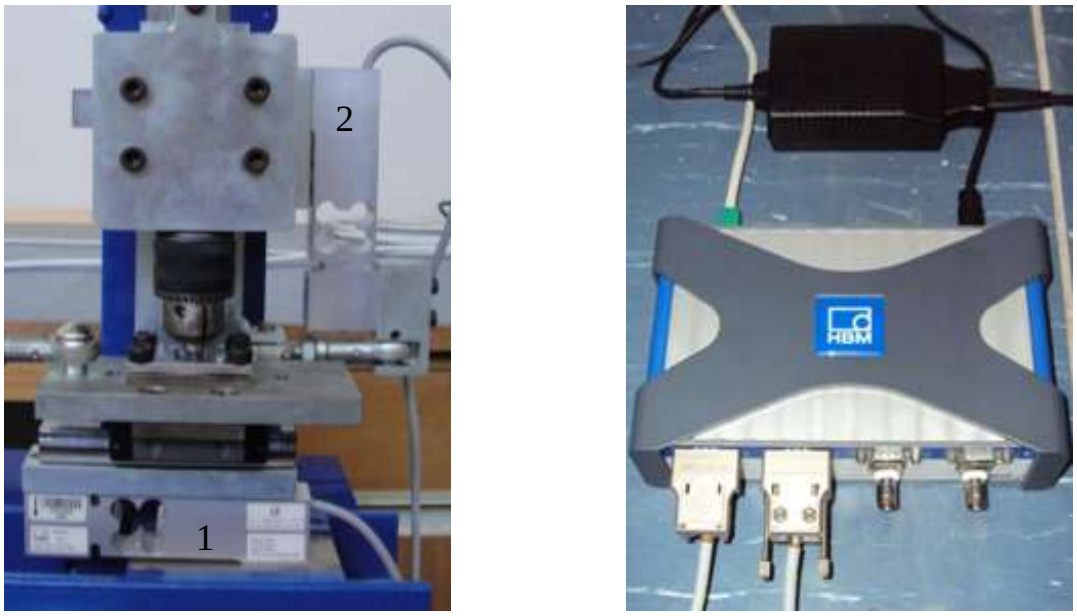

a) b)

Figure 3.13: Measuring equipment for sliding apparatus a) load cells and b) data acquisition unit

To be able to measure data from the load cells a data acquisition unit (DAQ) was needed to read the data. Through various discussions, it was decided to use a HBM Quantum MX410. The unit has four channels for reading data and is able to sample at a high frequency. The unit is shown in Figure 3.13 with two cables from the load cells plugged in. The software used with this DAQ is CatmanEasy-AP that was provided by the manufacturer. Figure 3.14 is a screenshot of the software when the DAQ is acquiring data from the load cells. The two real-time graphs shown in the figure are the normal force on the left and the tangential force on the right. For the specifications of each component in the measuring system see [***76***,***77***]

Table 3.11: Measurement equipment [***76***,***77***]

Type	Manufacturer	Specification	Amount
Load cell	HBM	SP4C3 (20kg)	2
Data Acquisition Unit (DAQ)	HBM	Quantum MX410	1

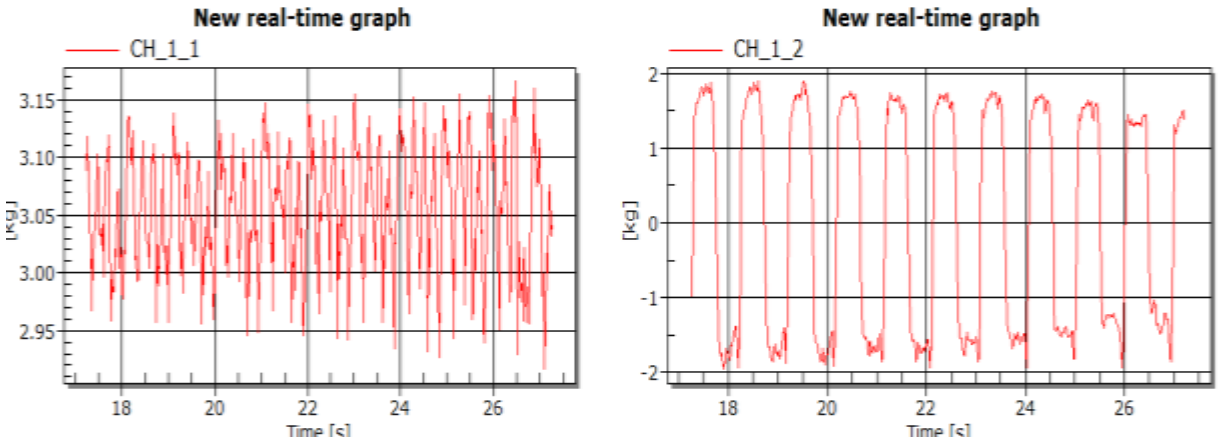

Figure 3.14: Screenshot of CatmanEasy-AP software when sliding apparatus was running and DAQ taking measurements

3.2.3 Conclusion

The sliding wear apparatus design was one of the objectives of the project. From experimentation, it was noted that the machine was able to create a sliding motion to cause wear and was able to measure friction between the test materials.

3.3 Sliding Experiments

A study of the titanium alloy, Ti6Al4V, was conducted to assess the dry sliding wear in different contact couples with different normal forces.

The SPS carbides had a limited amount of specimens and for this reason it was decided not to change the sliding speed of the experiments, and it was kept constant at 0.02m/s. Peak-to-peak amplitude of 12mm was chosen due to the size of the materials. The constant parameters for the experiments are shown in Figure 3.16. For the experiments, a 5 level 2 factor full factorial design (2^5) was chosen due to limitations on the number of materials available. A full factorial design means that all possible combinations are tested.

A flat pin-on-flat sliding configuration was used as shown in Figure 3.15. In the figure, the flat pin is labelled A and the base material B.

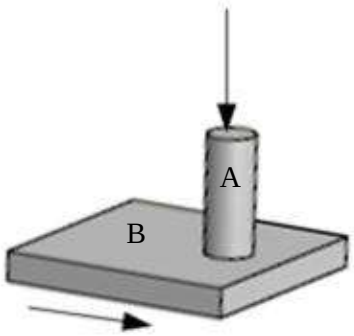

Figure 3.15: Experimental configuration

Figure 3.16 depicts how the experiments were designed. The experiments conducted were used to assess the material contact couples, as well as, what effects the variation of normal force had on the contact. A Ti6Al4V pin was used (label A in Figure 3.15). The pin was subjected to dry sliding contact with various base materials (label B in Figure 3.15).

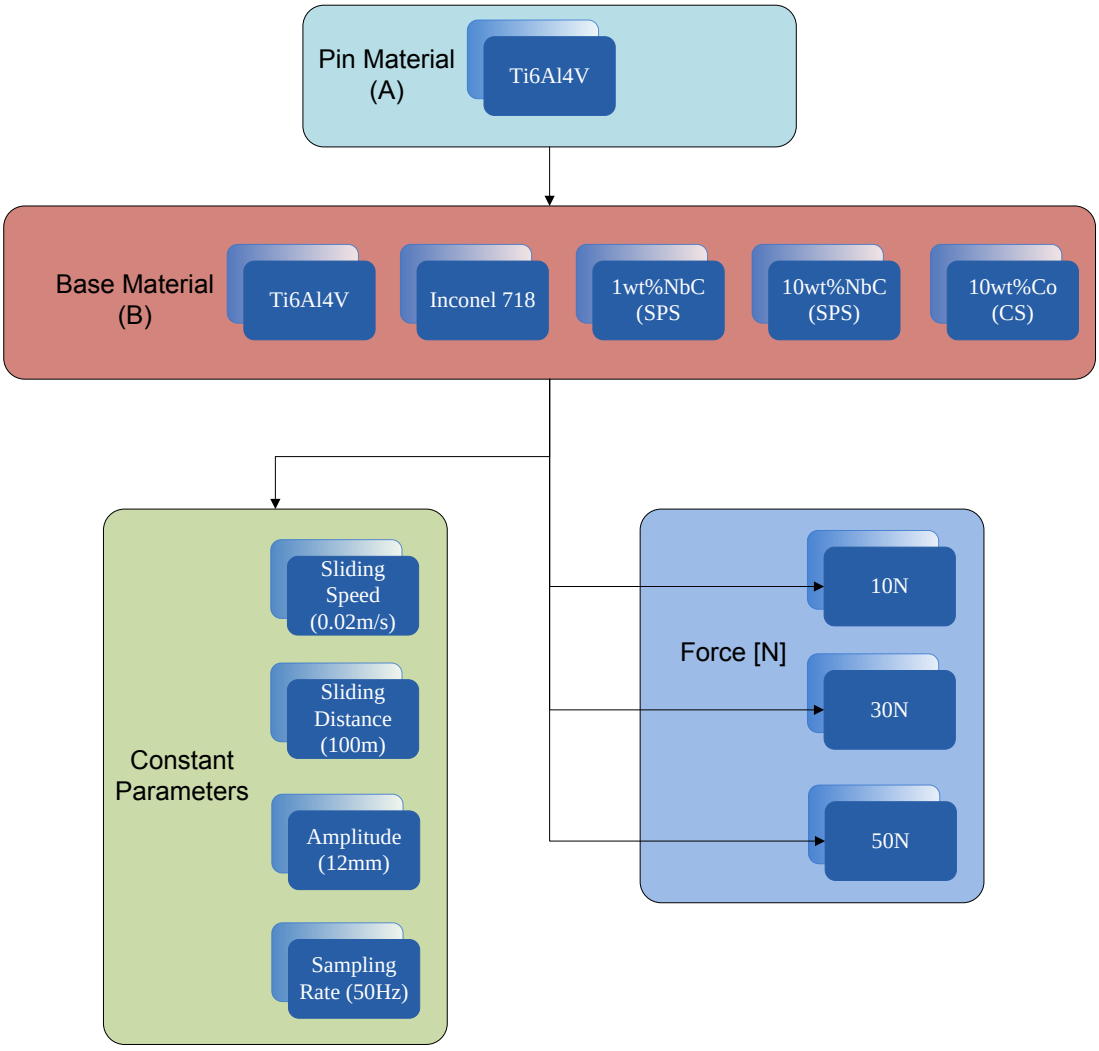

Figure 3.16: Experimental design for sliding experiments

The two aerospace materials chosen were Ti6Al4V and Inconel 718. The pin material was never changed, but rather coupled with a different base material for comparative purposes. The three carbides chosen were; WC-10wt%Co-1wt%NbC-0.3wt%Cr_3C_2 (SPS), WC-10wt%Co-10wt%NbC-0.3wt%Cr_3C_2 (SPS) and WC-10wt%Co (CS) was used for comparison purposes. The properties of these materials, as well as, Ti6Al4V and Inconel 718 are listed in Table 3.12.

Table 3.12: Properties of carbides and Ti6Al4V used in the experiment

Property	**1wt%NbC (SPS)**	**10wt%NbC (SPS)**	**10wt%Co (CS)**	**Ti6Al4V**	**Inconel 718**
Density [g/cm^3]	13.7	14.51	14.57±0.4	4.43	8.47
Hardness [GPa]	14.48±0.14	13.51±0.09	16.96±0.21	3.21	4.04
Fracture Toughness [Mpa.m$^{1/2}$]	14.75±0.73	15.17±0.32	9.87±0.01	75	120

Table 3.13 illustrates the methods and equipment used for examination of the sliding tests that were completed.

Table 3.13: Equipment used in final experiments

Equipment/Machinery	**Software**	**Purpose**
Zeiss EVO MA15	INCA	Analyze content, composition of carbides (SEM)
Olympus GX51 Inverted Optical Microscope	analysis 5.0 (Build 1210) Olympus Soft Imaging Solutions GmbH	Capturing images of worn surfaces
Sliding Apparatus	CatmanEasy-AP	Create sliding motion and determine friction coefficient
Micrometer		Measure length of pin

3.3.1 Experimental Procedure

Figure 3.17 depicts the experimental procedure followed for the sliding study. The first step is the preparation of the materials; these steps have been discussed in sections 3.1 for the carbides and Inconel 718). The Ti6Al4V material was polished using a Struers system. The procedure can be found in Struers Application Notes [***80***]. The other steps involve setting up the sliding apparatus. The pin and base material are clamped into their respective systems, the sliding speed is set, the load cells are zeroed, and the normal force is set to the specific value for the experiment. The final steps are to set the Catman software and to recheck that all the parameters are correct. The next phase as described as the experimentation phase. The apparatus is started and run for a specific period of time that is converted into a distance travelled.

Depending on the measurement strategy, the machine will be stopped and a measurement of the pin will be taken and documented. The data from the time period is recorded and saved. These steps can be repeated as many times as the experimental strategy requires. The final phase of the experiment involves data conversion, microscopy, SEM and EDS analysis. Data from the experiment is converted to graphs that can easily be understood and interpreted. The Ti6Al4V pin is inspected using an optical microscope and the base material is analysed using a SEM. To further understand the interaction of the materials EDS is used to produce quantitative data.

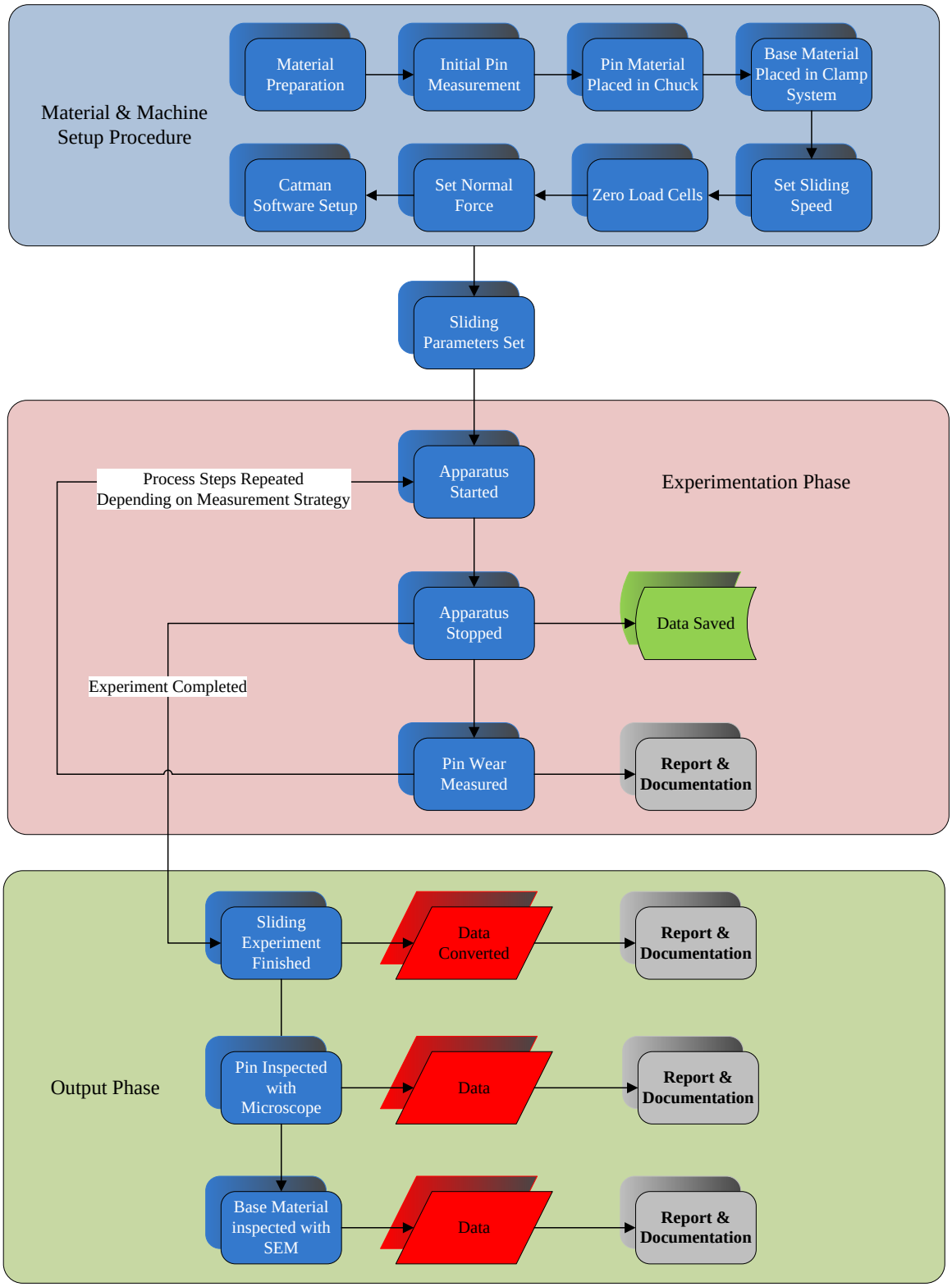

Figure 3.17: Experimental procedure for sliding experiments

3.3.2 Data Collection

A DAQ was used for data acquisition from the two load cells as described in section 3.2.2. The data was collected at a sampling rate of 50Hz. This frequency described means that 50 data points where taken every second. As the maximum sliding speed of the apparatus was not very high, this sampling rate was adequate.

Figure 3.18 is used to describe the sliding reciprocating motion used for the experiments. As shown, in the figure, the start position of the flat pin is located in the middle of the flat sample. On the clamping system the zero point for the sliding amplitude was marked. The table then moves to the left and reaches a maximum value or turning point at position B. The load cell measuring the tangential force is placed in such a way that this direction is seen as a positive force. Once the maximum positive amplitude is reached, donated as δ/2, the table starts moving in the opposite direction. The force is positive for a certain distance, but becomes negative as the table reaches its maximum value or turning point in the negative direction. The table then moves back and forth between the two positions B and C. The distance between these two point is described as the peak-to-peak amplitude of the sliding cycle and is denoted by δ. One full cycle is two times the value of this amplitude and is denoted as 2δ.

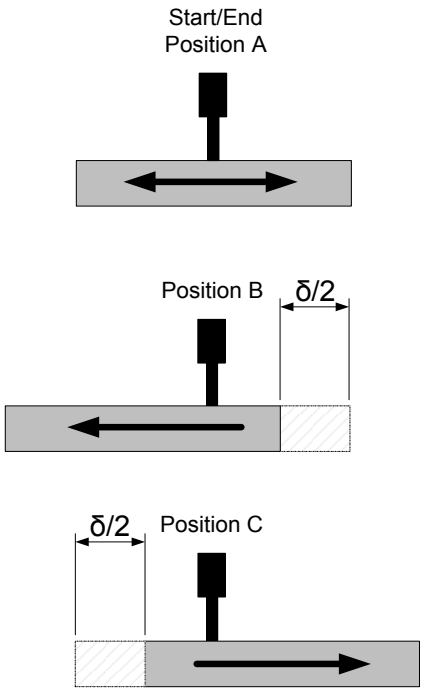

Figure 3.18: Schematic description of the sliding reciprocating motion

Data is collected in sections because the machine is stopped at certain intervals to measure the Ti6Al4V pin wear. The different sections have to be placed together and this was conducted using a program written in Matlab.

Figure 3.19 shows a typical output from the load cells over a sliding distance of 10 m and a normal force of 50N. The normal force is shown to be in the region of 50N. The tangential force goes from positive to negative because of the reciprocating motion. From this graph the friction coefficient can be determined.

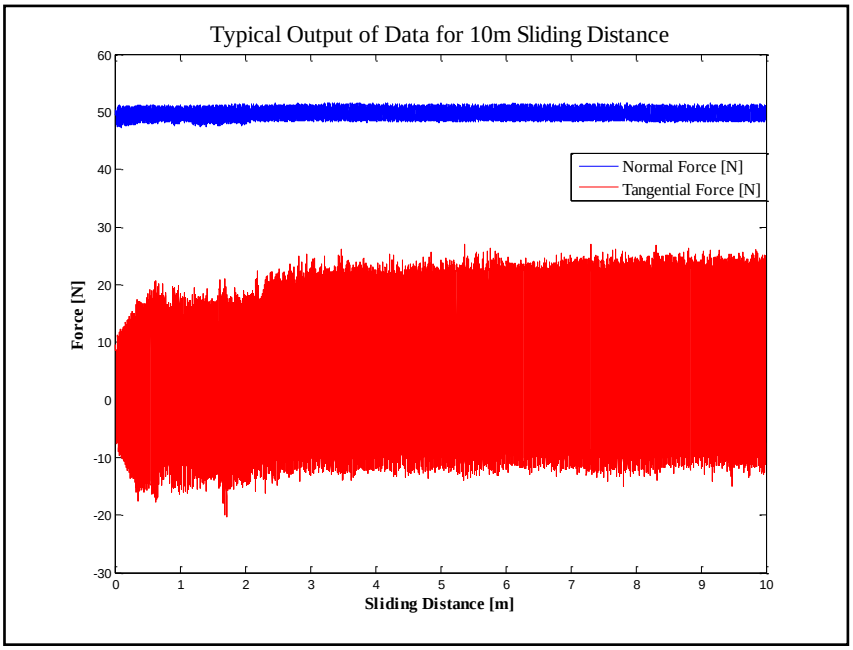

Figure 3.19: Typical graph of normal and tangential force over 10m sliding distance with a force of 50N

Figure 3.20 is a typical graph for a single sliding cycle. The graph goes from positive to negative over a specified distance.

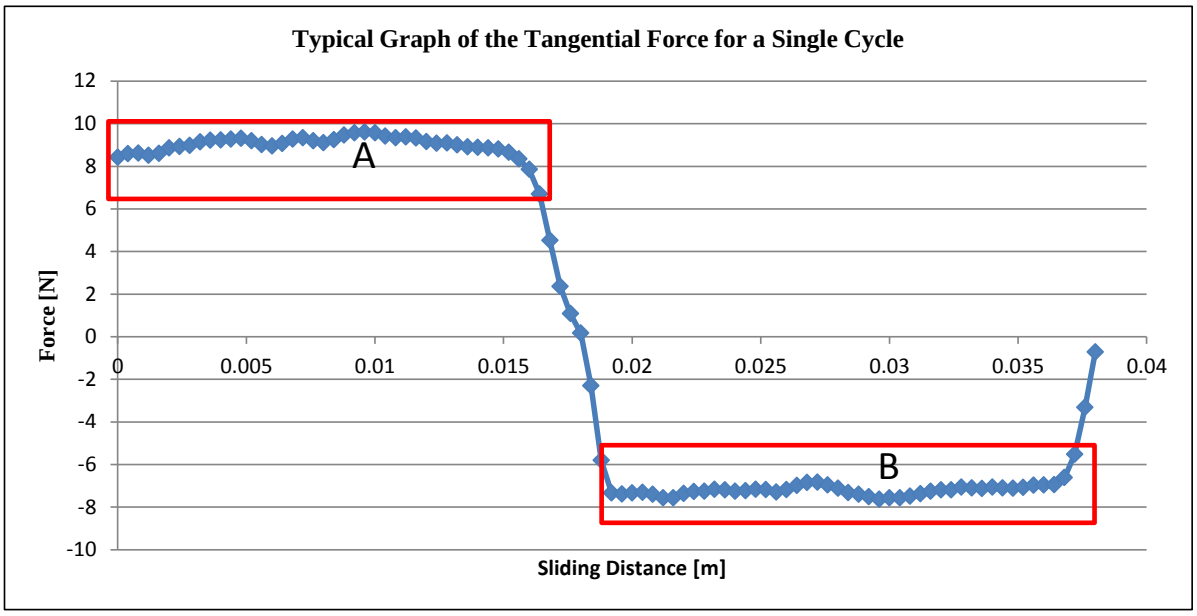

Figure 3.20: Typical graph of friction for a single cycle

Obtaining data that can be interpreted is vital to understanding friction in a sliding process. A program was created to convert the data measured by the load cells to graphs that were meaningful to the study.

The program is based on the gradient between two points on the graph shown in Figure 3.20. Using a gradient allows a certain set of data to be isolated. In this case the data isolated is marked as region A, positive, and region B, negative. The data contained in region A and B is inserted into equation 3.7 and a

value is calculated. The process is continued until all the data measured has been run through and all the values stored. $F_{positive}$ refers to region A, and $F_{negative}$ refers to region B on the figure. The variable *i* is used as a counter for which cycle the program is calculating. An average value of each region is calculated and then averaged again with the average from region B.

$$F_i = \frac{\frac{\sum|F_{positive}|}{n} + \frac{\sum|F_{negative}|}{n}}{2} \tag{3.7}$$

Equation 3.8 is used to obtain the average of the normal force [*N*] of the cycle. The values are summed and divided by the number of points, *n*.

$$N_i = \frac{\sum T_i}{n} \tag{3.8}$$

The values obtained in equations 3.7 and 3.8 are used to calculate the coefficient of friction as shown in equation 2.15. A more in depth description of equation 3.9 is available in Section 2.1.

$$\mu_i = \frac{F_i}{N_i} \tag{3.9}$$

The data conversion discussed, is used to produce a coefficient of friction graph, discussed in the following chapter. Figure 3.21 is a graphical depiction of the entire data conversion process used in the sliding experiments.

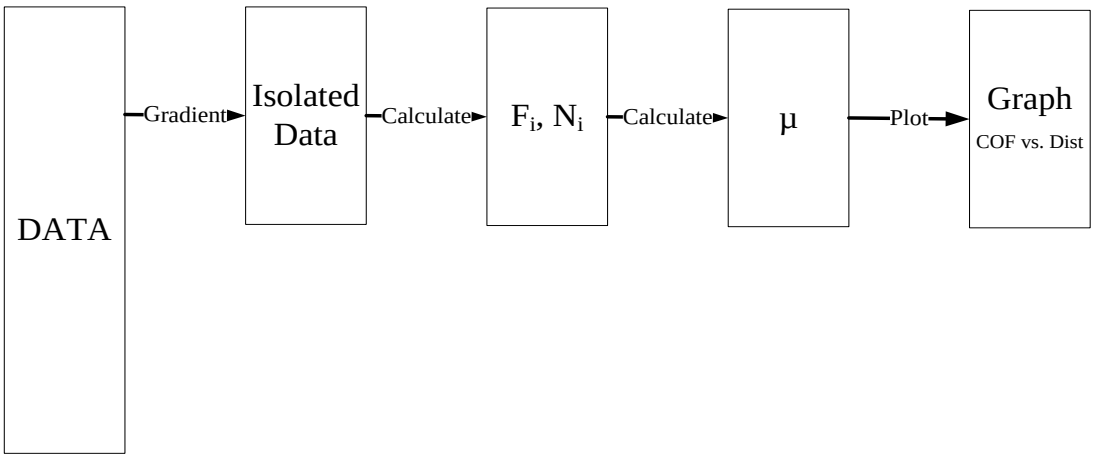

Figure 3.21: Graphical depiction of data conversion

3.3.3 Wear Measurement

Wear measurement was done using a micrometer. Equation 3.10 describes the volume of a cylinder. V_{loss} is the volume loss in mm^3; r is the radius of the cylinder in mm and length is the change in length of the pin in mm. The initial length was measured and then, after a specific distance, another measurement was taken of the length. The difference between these two values was the length described in equation 3.11.

$$V_{loss} = \pi r^2 \times length \qquad 3.10$$

3.3.4 Outputs of Sliding Experiments

The experimental design and procedures described in this section are an integral part of the project. The background studies laid a foundation for the sliding experiments. The outputs of the experiments are listed below:

- Pin wear measurement
- Coefficient of friction
- SEM & EDS on base material
- Optical microscopy on Ti6Al4V pin
- Comparison of the severity of using V_{loss}

3.4 Conclusion

Correct methods and procedures allow for accurate and correct data gathering. Deciding on how the data will be measured, what the outputs are and how it will be depicted are important. The chapter has outlined all these methods and the sliding apparatus. The following chapter discusses the results and findings of these experiments in detail.

4. Results & Discussion

The chapter consist of three sections. Results of the SPS carbide mechanical and material characterization, initial sliding experiments and the sliding experiments using varying loads. The experiments are discussed in detail and results are shown graphically or otherwise stated.

4.1 SPS Carbides – Mechanical & Material Characterization

This section discusses the results from specific set of materials tests as described in section 3.1. Table 4.1 is used as a reference table for the results discussed in this chapter. For instance 1.1 refers to the WC – 10wt%Co – 1wt%NbC cemented carbide.

Table 4.1: Reference numbers of cemented carbides (Co-binder)

Reference Number	Materials Composition
1.1	WC – 10wt%Co – 1wt%NbC
1.2	WC – 10wt%Co – 1wt%NbC
1.3.1	WC – 10wt%Co – 1wt%NbC - 0.3wt%Cr_3C_2
1.3.2	WC – 10wt%Co – 1wt%NbC - 0.3wt%Cr_3C_2
1.4	WC – 10wt%Co – 3wt%NbC - 0.3wt%Cr_3C_2
1.5.1	WC – 10wt%Co – 10wt%NbC - 0.3wt%Cr_3C_2
1.5.2	WC – 10wt%Co – 10wt%NbC - 0.3wt%Cr_3C_2
1.5.3	WC – 10wt%Co – 10wt%NbC - 0.3wt%Cr_3C_2
1.5.4	WC – 10wt%Co – 10wt%NbC - 0.3wt%Cr_3C_2

Figure 4.1 depicts the different hardness values of the SPS carbides and the CS carbide is used as a baseline to compare the SPS to. The hardness of samples decreases with the addition of NbC this is in accordance with Haung [***64***]. The literature attributes the decrease in hardness to the WC-Co fraction decreasing. Considering Figure 4.1 it is seen that the hardness of the SPS carbides have lower values than that of the CS carbide, except for the first two samples. From the graphs it can be seen that the when the hardness decreases the fracture toughness increases this was also observed by Haung [***64***].

It is important to note that a smaller grain size means a harder material [***42***]. Table 4.2 contains the summary of all the property values for each specific material. The coercivity value is used to compare grain size of the samples. The higher the coercivity value the smaller the grain size of the specific sample. A strong relationship can be seen by looking at Table 4.2 and Figure 4.1.

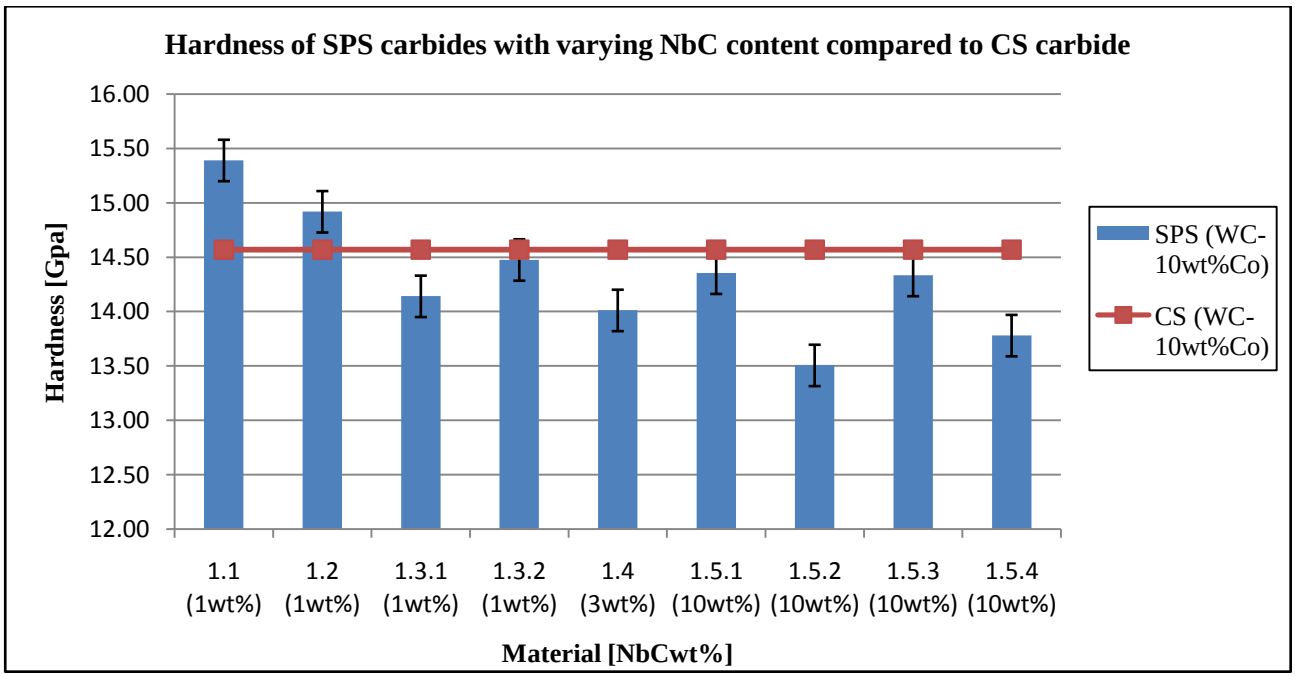

Figure 4.1: Hardness [GPa] of SPS carbides with increasing NbC content [wt%] compared to CS carbide

The fracture toughness of the samples is shown in Figure 4.2. Comparing the fracture toughness of the SPS carbides to that of a CS carbide it can be seen that the fracture toughness of the SPS material is lower than that of the CS carbide. There is a relationship between hardness and fracture toughness. For instance the harder the material the lower the fracture toughness will be. As described in section 3.1 fracture toughness is the resistance to further crack growth after a crack has been formed. With this reasoning can be noted that the relationship described above is accurate. Take for instance sample 1.1 that has a hardness of 15.39GPa and a fracture toughness of 12.83 $MPa.m^{1/2}$. Compare this to sample 1.5.4 and a relationship can be seen where the hardness is lower than sample 1.1 and the fracture toughness is higher.

Figure 4.3 shows the variation of all the carbides hardness and fracture toughness with increasing NbC content. Many of the points follow a pattern that with increasing hardness, there is a decrease in fracture toughness.

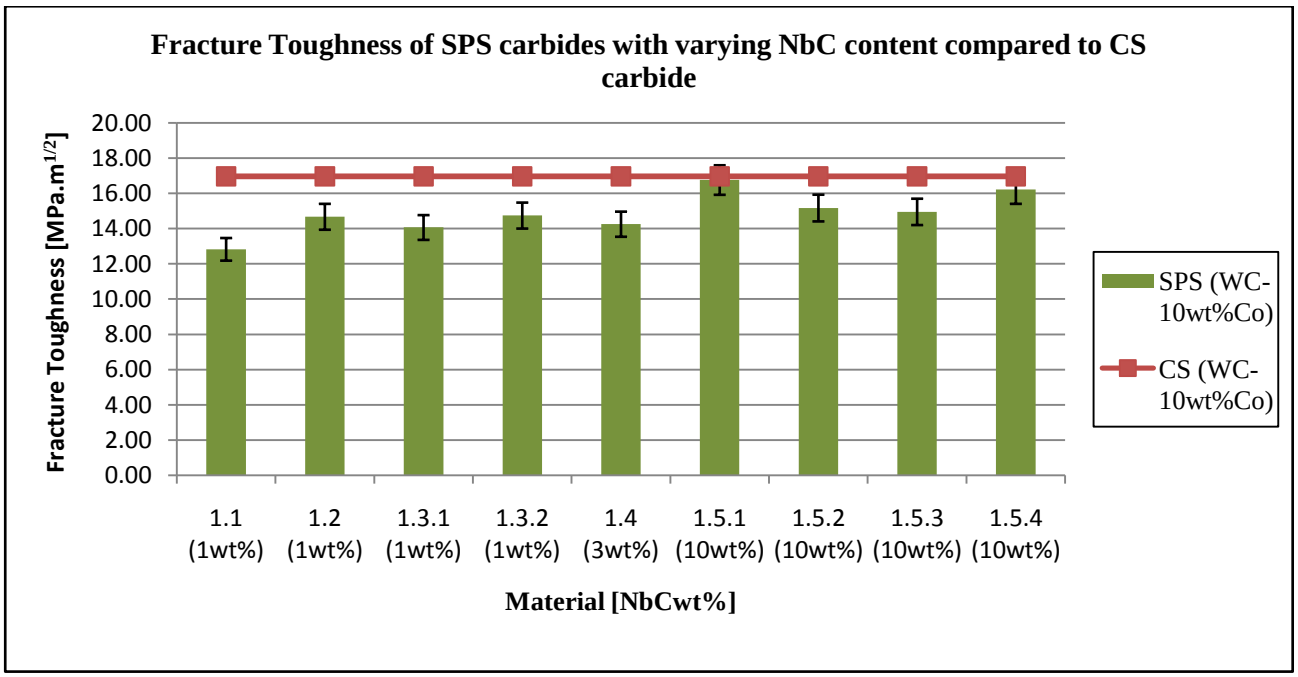

Figure 4.2: Fracture Toughness [MPa.m$^{1/2}$] of SPS carbides with increasing NbC content [wt%] compared to CS carbide

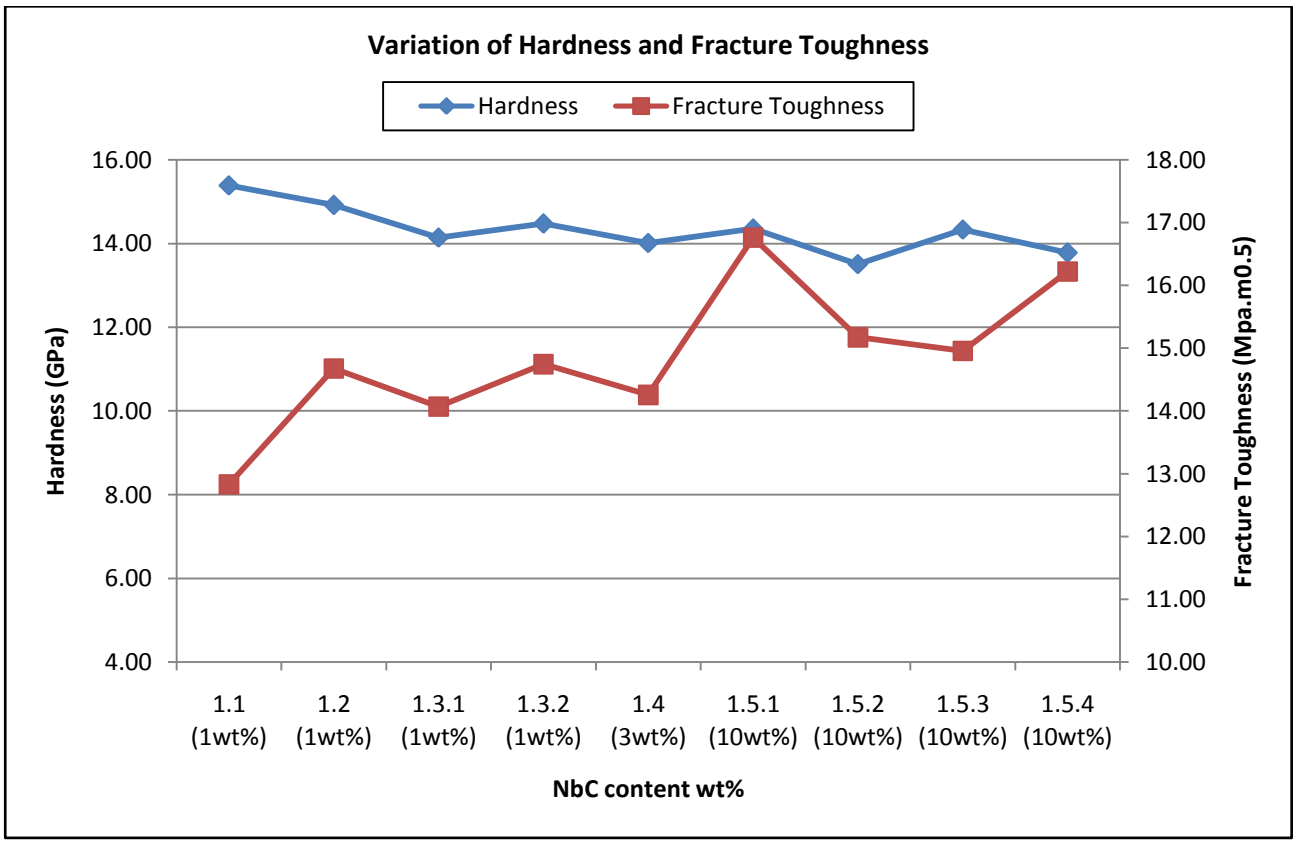

Figure 4.3: Variation of hardness [GPa] and fracture toughness [MPa.m$^{1/2}$] for varying NbC content [wt%]

Figure 4.4 shows hardness versus fracture toughness for all the materials described in this section. An optimum material for good wear resistance would lie to the top right hand corner of the graph.

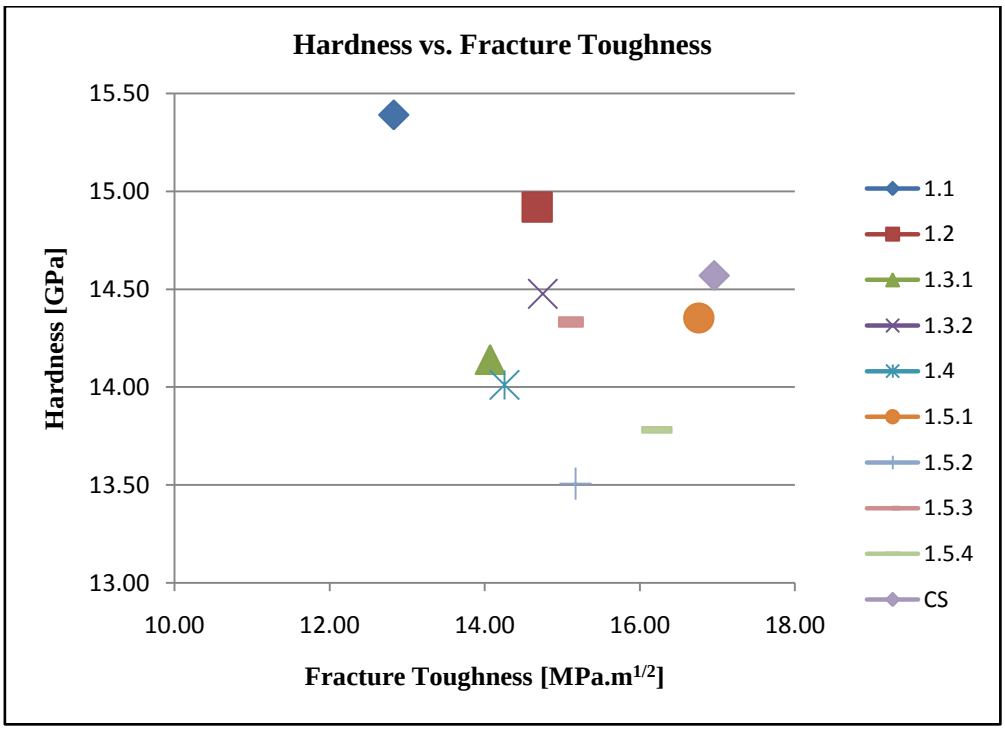

Figure 4.4: Hardness [GPa] vs. Fracture Toughness [MPa.m$^{1/2}$] of carbides

Figure 4.5, Figure 4.6, Figure 4.7 and Figure 4.8 contain SEM images and EDS analysis of the four different carbides present in the study. The first image of each figure is a lower level magnification image (2000X magnification) to show a larger surface are of the carbide.

Figure 4.5 is a compilation of SEM images and EDS analysis of a WC-10wt%Co-1wt%NbC SPS carbide. Figure 4.5 b) is an area analysis of the image shown. The analysis shows that all the elements are present and that the light grey areas are a combination of all the elements. W is the main element in this phase and it can be seen that the grains are smaller than those of the dark grey regions. The large dark grey phases are those of Nb(C, W) phases and are fairly large. Figure 4.5 c) is spot analysis of one of these areas. The EDS shows that Nb is the element present with the largest wt%. From the XRD report (Appendix B Figure B.1 and Table B.1) the dominant phases in the material were WC, NbC and Co, but in certain materials another Nb6C4.73 was picked up.

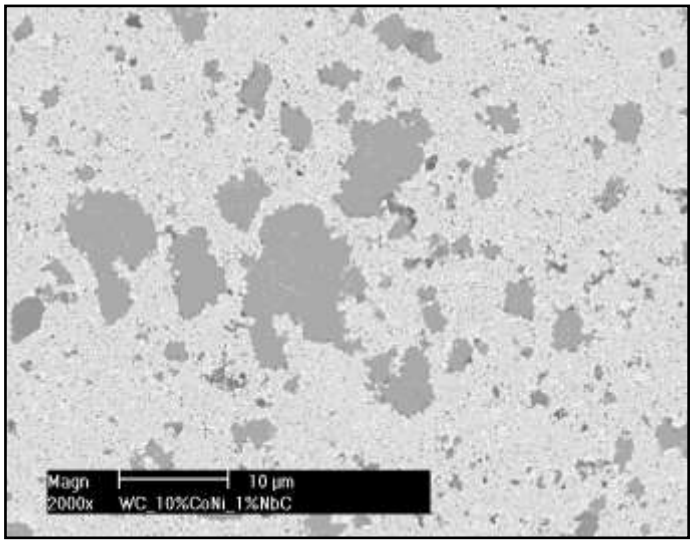

a)

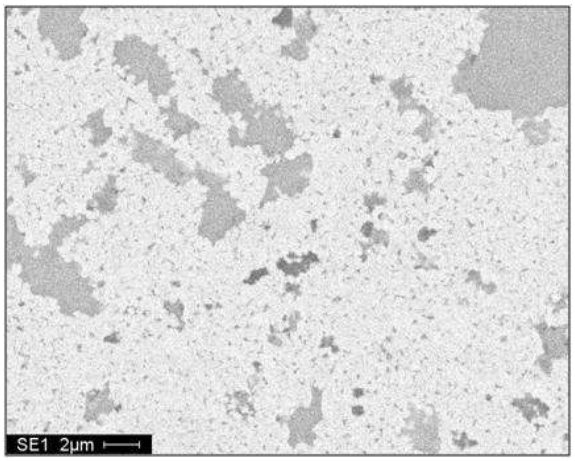

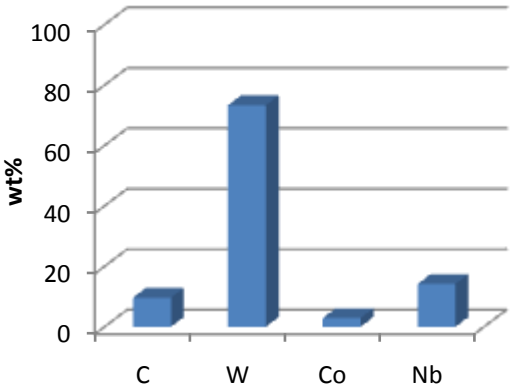

b)

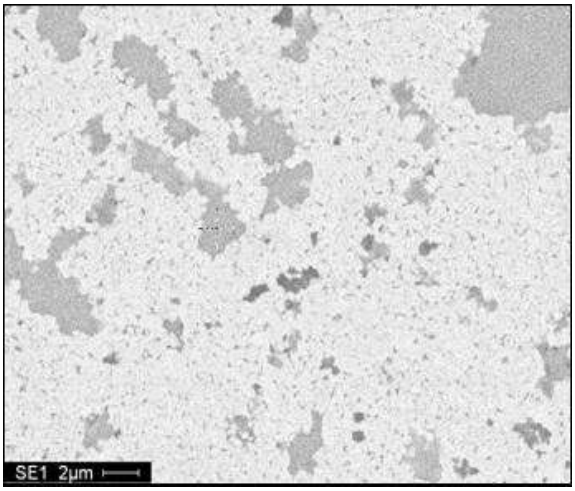

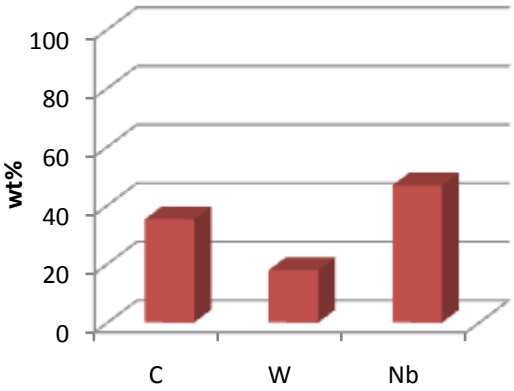

c)

Figure 4.5: SEM images and EDS analysis of WC – 10wt%Co – 1wt%NbC; a) image of surface, b) area analysis of surface, c) spot analysis on surface

Figure 4.6 is a selection of SEM images and EDS analysis of a WC – 10wt%Co – 1wt%NbC - 0.3wt%Cr_3C_2 SPS carbide. The analysis of image Figure 4.6 b) shows that the light grey area is a complex phase of W, C, and Co. As in the previous example, the light grey has smaller grains compared to the dark grey are. The

dark grey are areas are a phases of Nb(C, W). The analysis of Figure 4.6 c) illustrates that the very dark areas contain all the different elements of the material including oxygen. In this material Cr is also present. As described in the literature (Section 3.1) the Cr is used as a grown growth inhibitor for Nb. The XRD report (Appendix B: Figure B3 and Table B3) showed that the dominant phases were WC, NbC and Co.

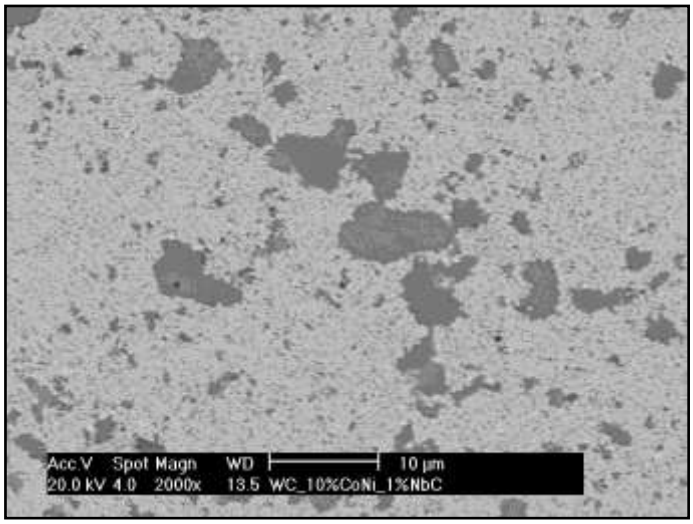

a)

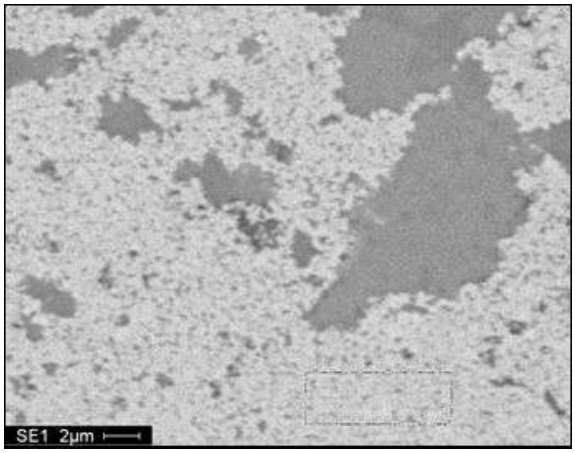

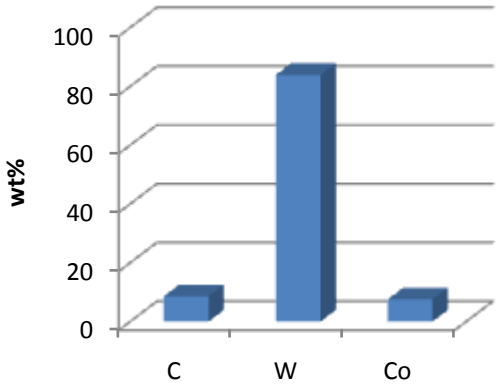

b)

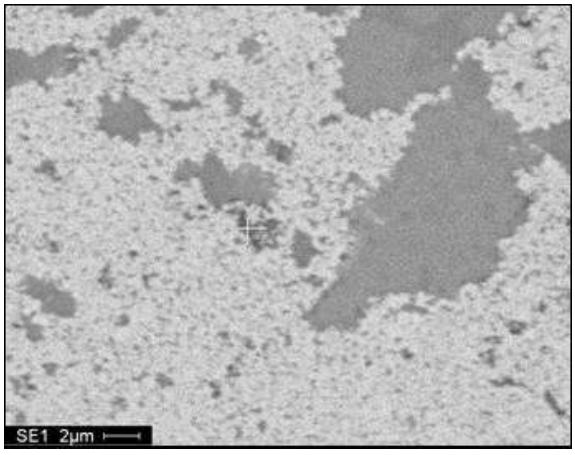

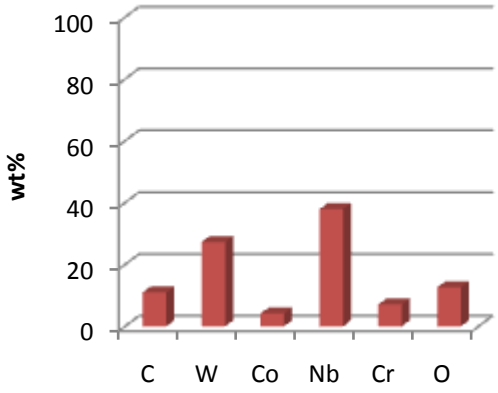

c)

Figure 4.6: SEM images and EDS analysis of WC – 10wt%Co – 1wt%NbC - 0.3wt%Cr3C2; a) image of surface, b) area analysis of surface, c) spot analysis on surface

Figure 4.7 includes and analysis of a WC – 10wt%Co – 3wt%NbC - 0.3wt%Cr_3C_2 SPS carbide. As in previous examples the light grey are is a complex phase of C, W, and Co, and is shown in Figure 4.7 b). The larger dark grey areas are made up of the previously named elements and include others such as Nb, and Cr, this is depicted in Figure 4.7 b). In this example it seems that the Cr forms around the NbC phase within the material, this is possible as Cr is used as a grain growth inhibitor. From XRD report (Appendix B: Figure B3 and Table B3) the three main phases identified were WC, Nb6C5, Cr23C6.

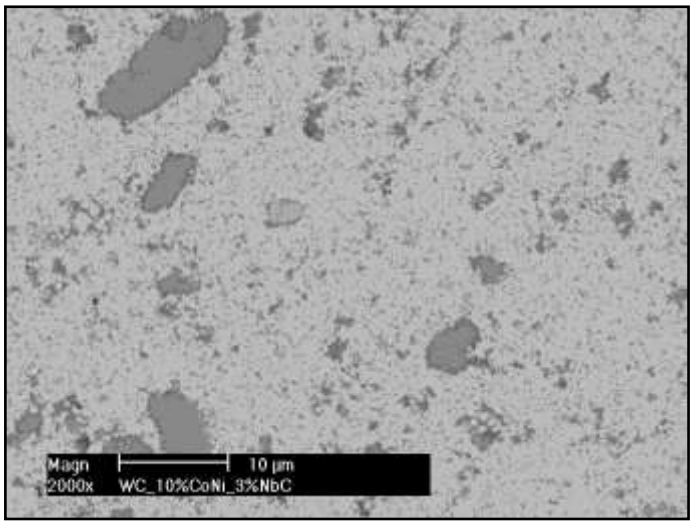

a)

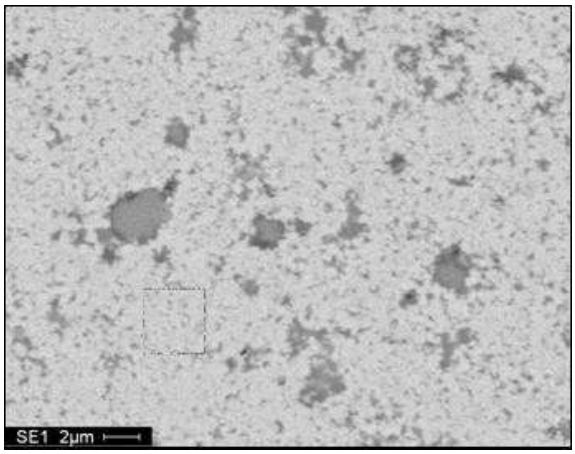

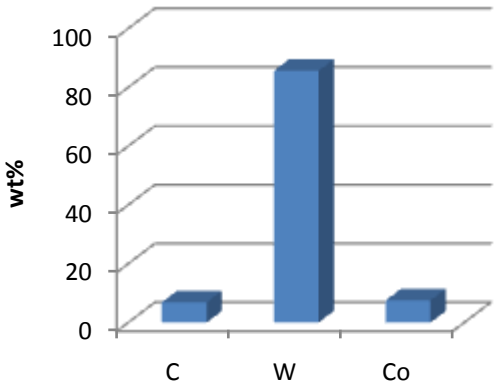

b)

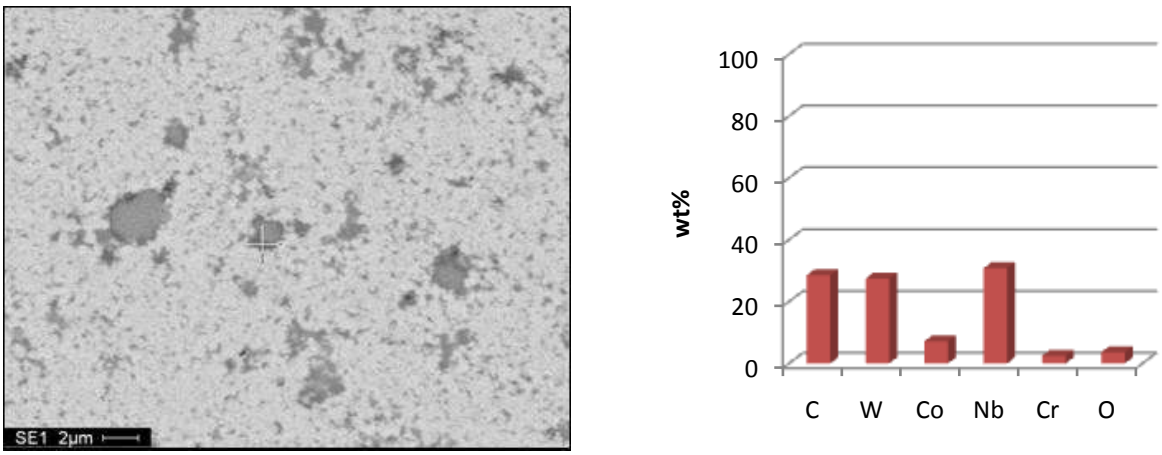

c)

Figure 4.7: SEM images and EDS analysis of WC – 10wt%Co – 3wt%NbC - 0.3wt%Cr3C2; a) image of surface, b) area analysis of surface, c) spot analysis on surface

Figure 4.8 is a collection of images and analysis results from a WC – 10wt%Co – 10wt%NbC - 0.3wt%Cr_3C_2 SPS carbide. The lighter grey areas a made up of W, C, and Co as shown in Figure 4.8 b). The darker grey areas are a complex phase of Nb, Cr, W, C, and Co as depicted in Figure 4.8 c). In this set of results, as in the previous, it seems that the Cr is forming around the NbC (dark grey) regions. The main phases identified by using XRD were WC, NbC and Co2Nb4C.

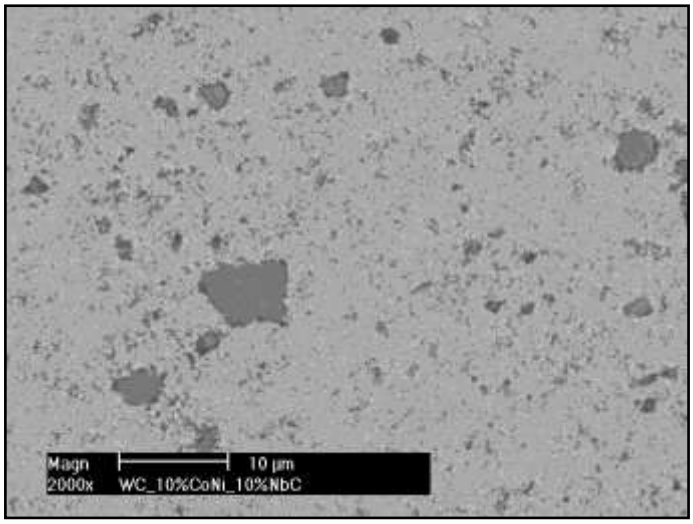

a)

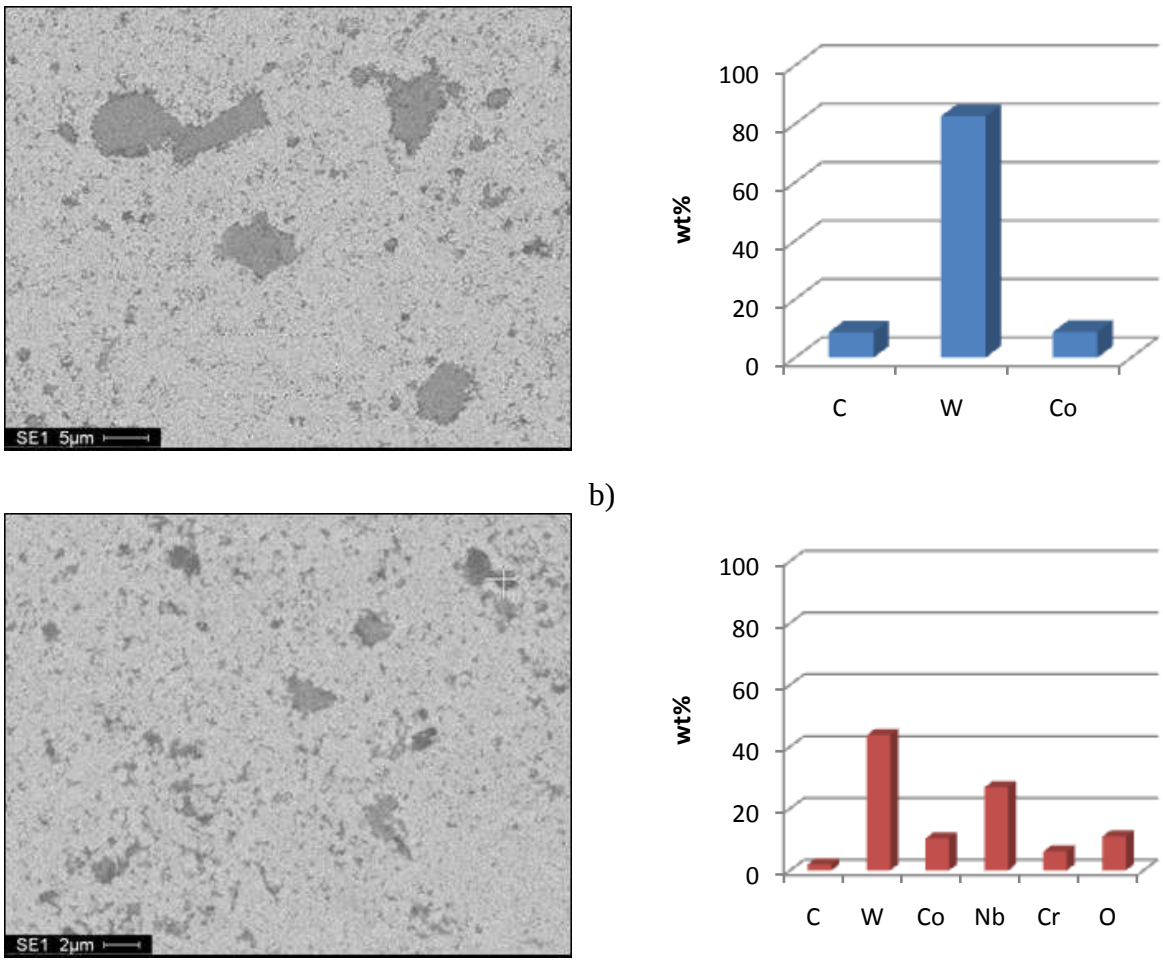

Figure 4.8: SEM images and EDS analysis of WC – 10wt%Co – 10wt%NbC - 0.3wt%Cr3C2; a) image of surface, b) area analysis of surface, c) spot analysis on surface

In samples 1.3.1 through to 1.5.4 Cr was picked up in increasing content, this was concluded using EDS and SEM analysis. In many of the samples it was seen that the Cr formed around the larger NbC regions. This is shown in Figure 4.7 and Figure 4.8. The large Nb(C, W) grains decrease in size with an increase in Cr, thus the concluding that Cr can be utilized as a grain growth inhibitor.

The different phases within the alloys were determined through XRD. In many of the samples it was a distinct Cr inclusive phase was not picked up. The pattern of a Cr23C6 phase could be fitted to the peaks of the XRD plot with two of the samples; one alloy containing 1wt%NbC and the other containing 3wt%NbC.

In all of the samples there was a definite NbC phase. The phase came forth in a couple of different forms; Nb6C4.73, NbC, Nb6C5 or a combination of NbC and one of the others. The samples with 10wt%NbC had a phase that was common to all of them, namely a Co0.23Nb0.77 phase.

Table 4.2: Summary of 10wt%Co SPS carbide properties

Ref Number	**1.1**	**1.2**	**1.3.1**	**1.3.2**	**1.4**	**1.5.1**	**1.5.2**	**1.5.3**	**1.5.4**
Material Composition	**WC-10wt%Co-1wt%NbC**	**WC-10wt%Co-1wt%NbC**	**WC-10wt%Co-1wt%NbC-0.3wt%Cr_3C_2**	**WC-10wt%Co-1wt%NbC**	**WC - 10wt%Co-3wt%NbC-0.3wt%Cr_3C_2**	**WC-10wt%Co-10wt%NbC-0.3wt%Cr_3C_2**	**WC-10wt%Co-10wt%NbC-0.3wt%Cr_3C_2**	**WC-10wt%Co-10wt%NbC-0.3wt%Cr_3C_2**	**WC-10wt%Co-10wt%NbC-0.3wt%Cr_3C_2**
Properties									
Hardness [GPa]	15.39	14.92	14.14	14.48	14.01	14.35	13.51	14.33	13.78
Fracture Toughness, K_{IC} [MPa.$m^{1/2}$]	12.83	14.68	14.07	14.75	14.26	16.76	15.17	14.96	16.22
Density, ρ [g/cm^3]	13.91	13.81	13.48	13.70	14.14	14.52	14.51	14.40	14.44
Poisson's ratio, ν	0.21	0.21	0.20	0.21	0.18	0.20	0.22	0.20	0.21
Shear modulus, G [Gpa]	246.62	240.45	237.14	243.16	243.25	257.42	237.10	247.39	246.54
Young's modulus, E [Gpa]	598.38	584.06	569.01	587.17	574.37	620.20	577.93	595.69	598.61
Bulk modulus, B, [Gpa]	347.69	340.98	315.81	334.45	299.73	349.98	342.47	335.34	348.87
Magnetic Saturation [%]	5.31	6.07	7.19	7.25	9.27	9.30	9.45	9.24	8.92
Coersivity, H_c [Ka/m]	28.05	30.62	28.25	28.35	20.81	23.91	22.74	23.45	24.41

Two samples were used that had a Ni binder. Table 4.3 is a reference table for the Ni-binder carbides. The reference number is listed as well as the composition of the material. The first sample had a composition of WC - 9.3wt%Ni - 6.25wt%TiC and the second WC - 9.3wt%Ni - 6.25wt%TiC – 3.5wt%Mo2C. The properties of the samples are listed in Table 4.4.

Table 4.3: Reference numbers of cemented carbides (Ni-binder)

Reference Number	Original Materials and Composition
3.1	WC – 9.3wt%Ni – 6.25wt%TiC
3.2	WC – 9.3wt%Ni – 6.25wt%TiC – 3.5wt%Mo_2C

Comparing the two SEM images of the two different samples it seems that the grain sizes slightly larger in the WC - 9.3wt%Ni - 6.25wt%TiC alloy. The literature already discussed, explains that Mo is a proven grain growth inhibitor. It can also be seen that the hardness of the WC - 9.3wt%Ni - 6.25wt%TiC alloy is not as hard as the alloy with 3.5wt%Mo_2C additive. Figure 4.9 shows the hardness of the two materials. The material containing 3.5wt%Mo_2C has a higher hardness. Figure 4.10 is a graph of the fracture toughness of the materials. In this case the material with 3.5wt%Mo_2C has higher fracture toughness. From these two graphs it can be concluded that the 3.5wt%Mo_2C has a positive effect on the composition and improves hardness and fracture toughness properties.

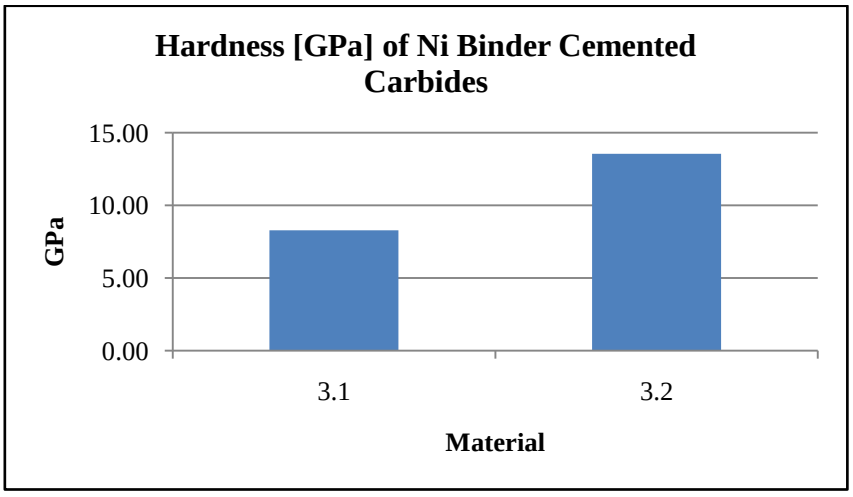

Figure 4.9: Hardness [GPa] of Ni binder cemented carbides

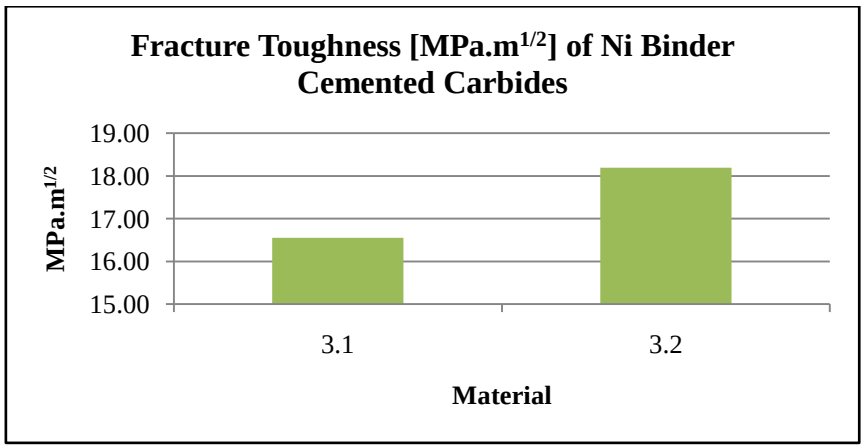

Figure 4.10: Fracture toughness [MPa.m$^{1/2}$] of Ni binder cemented carbides

Figure 4.11 and Figure 4.12 are a compilation of SEM images and EDS area and spot analysis. Figure 4.11 is a selection of images of a WC – 9.3wt%Ni – 6.25wt%TiC SPS carbide. Figure 4.11 shows an area analysis of the lightest region. This phase is made up of all the elements present in the material, namely, W, C, Ni and Ti. Figure 4.11 b) depicts a spot analysis of one of the darkest areas of the carbide. The analysis shows that the region is only made up of Ti and C. The grey phase within the images is complex phase made up of W, C and Ni. The spot analysis of the grey phase is shown in Figure 4.11 c). The XRD (Appendix B: Figure B.4 and Table B.4) report showed that the dominant phases in the material were WC, TiC0.981, NiC, Ni and C.

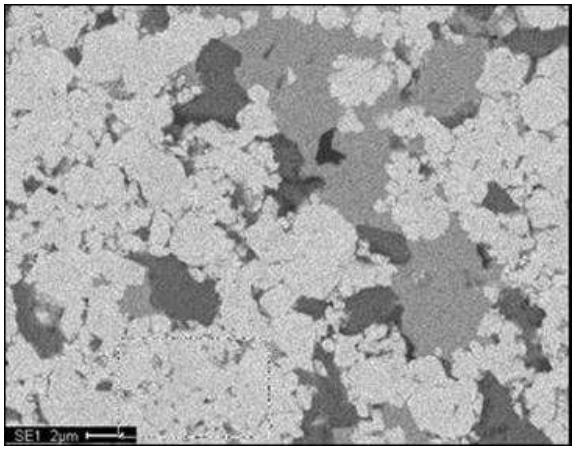

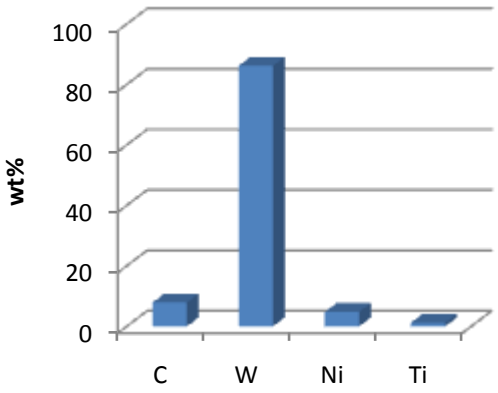

a)

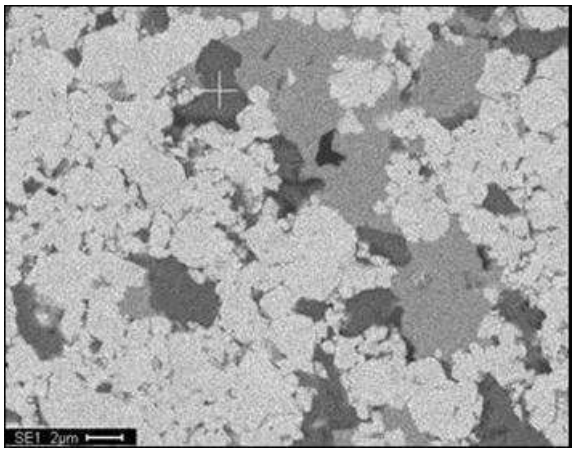

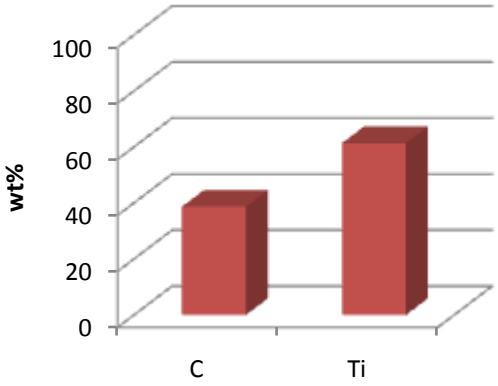

b)

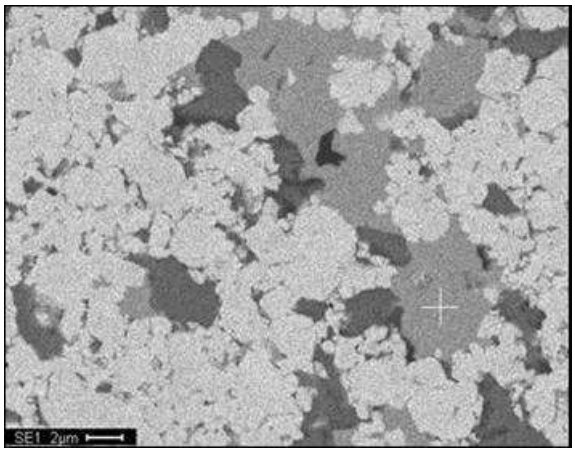

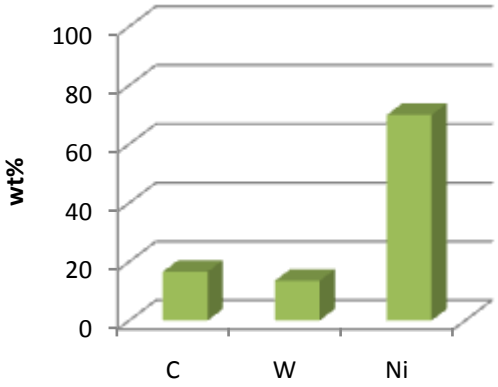

c)

Figure 4.11: SEM images and EDS analysis of WC – 9.3wt%Ni – 6.25wt%TiC

Figure 4.12 depicts the SEM images of a WC – 9.3wt%Ni – 6.25wt%TiC – 3.5wt%Mo_2C SPS carbide. The area analysis, Figure 4.12 a), shows that the elements W, C, Ni, and Mo are present, the exception is Ti. The next image, Figure 4.12 b) shows that the dark regions are a phase of Ti, C with a very small amount of W present. This coincides with the previous images of Figure 4.11 b) were the dark regions were found to be made up of Ti, as well as C. From the literature already discussed, this shows that TiC has low solubility in Ni. The grey regions within the material are a phase consisting of C, W, Ni, Ti, and Mo. The XRD report (Appendix B: Figure B.5 and Table B.5) for this material showed that four phases formed; WC, Ti5.73C3.72, C, and MoNi.

The XRD output for both materials showed that no Ti(C, Ni) phases had been formed and this is once again in accordance with the literature. The peaks of the specific phases were the nearest fit to those of the material that was being investigated.

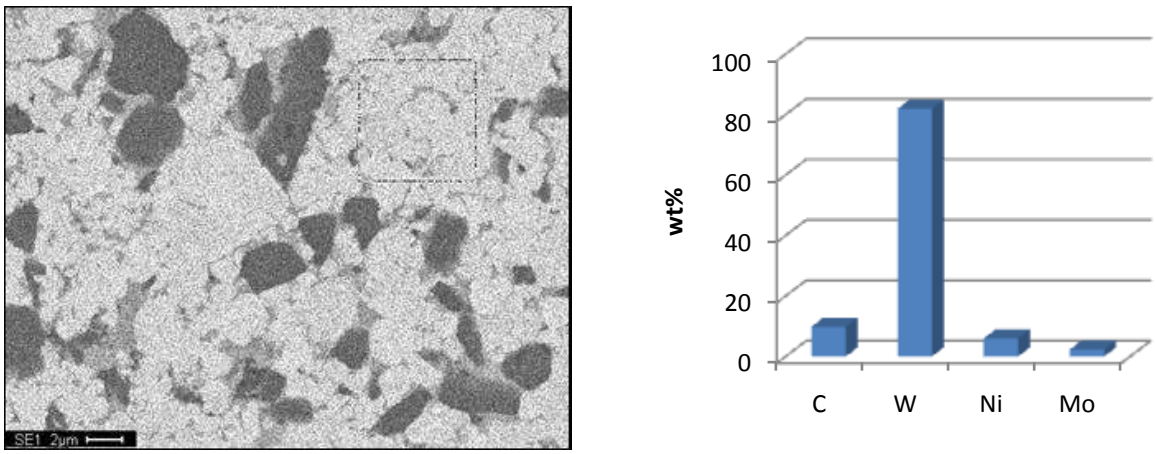

a)

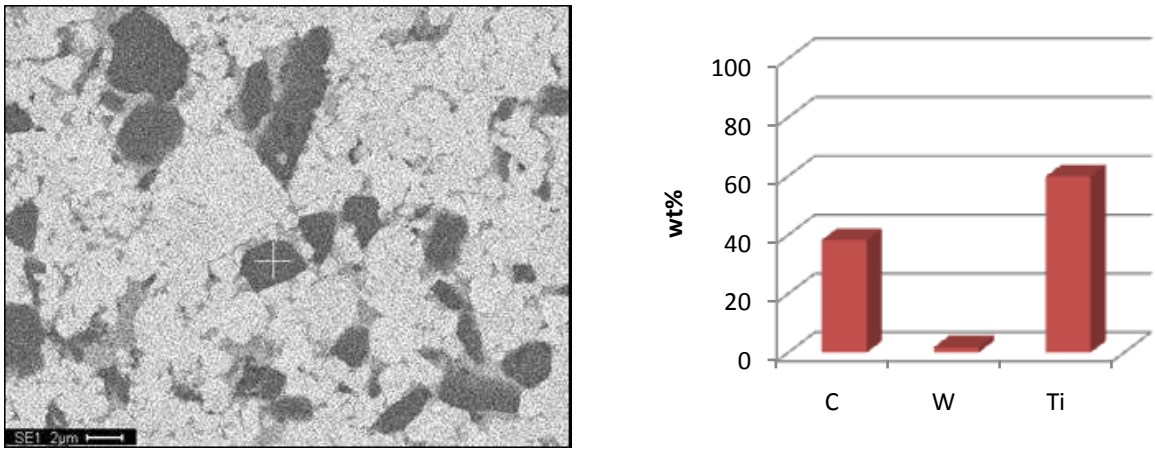

b)

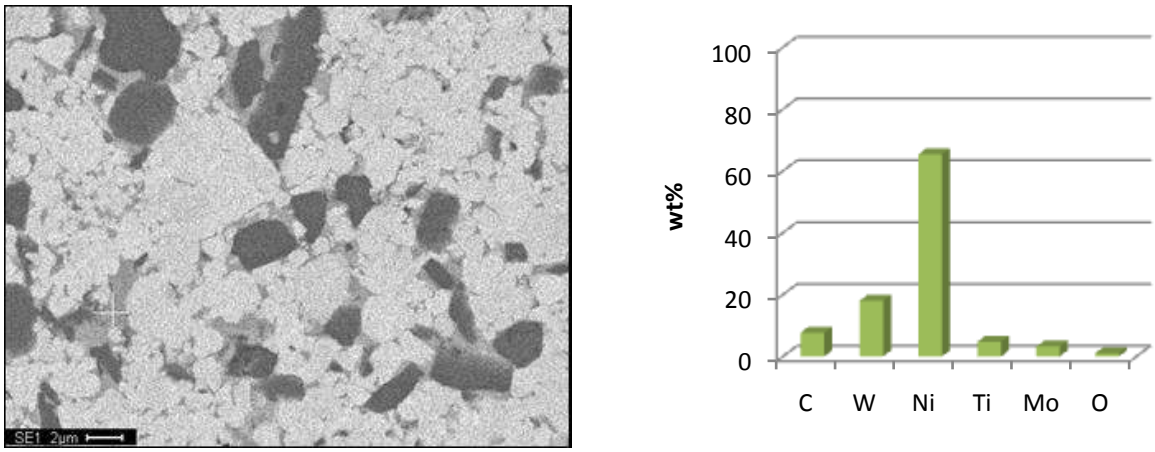

c)

Figure 4.12: SEM images and EDS analysis of WC – 9.3wt%Ni – 6.25wt%TiC – 3.5wt%Mo_2C

Table 4.4: Properties summary for samples with Ni binder

Ref Number	**3.1**	**3.2**
Material Composition	**WC - 9.3wt%Ni - 6.25wt%TiC**	**WC - 9.3wt%Ni - 6.25wt%TiC - 3.5wt%Mo2C**
Properties		
Hardness [GPa]	8.29	13.55
Fracture Toughness, K_{IC} [MPa.m$^{1/2}$]	16.55	18.19
Density, ρ [g/cm3]	12.39	13.19
Poisson's ratio, ν	0.26	0.21
Shear modulus, G [GPa]	190.48	242.28
Young's modulus, E [GPa]	480.19	588.24
Bulk modulus, B, [GPa]	334.10	342.77

4.1.1 Conclusion

The results discussed in this section pertain to the mechanical and material characterization of SPS carbides. It can be concluded that by increasing the niobium content, the hardness of the Co-binder SPS carbide, is decreased. The chromium within these carbides does act as a grain growth inhibitor for the niobium.

The SPS carbides with a Ni-binder and additions of TiC do not show particularly good results. The addition of Mo_2C has an effect on the carbide as both the hardness and fracture toughness increase.

4.2 Sliding Experiments

In this section the results of the sliding wear experiments between three carbides coupled with a Ti6Al4V pin are discussed. The friction graphs, pin wear, optical microscope- and SEM images are used to describe the mechanisms of the wear taking place.

The two aerospace materials used were Ti6Al4V and Inconel 78. The three carbides used in the experiments were a SPS WC-10wt%Co-1wt%NbC-0.3wt%Cr_3C_2 carbide that is referred to as 1wt%NbC carbide, a SPS WC-10wt%Co-10wt%NbC-0.3wt%Cr_3C_2 that is referred to as a 10wt%NbC carbide and a conventionally sintered WC-10wt%Co carbide, referred to as a CS carbide.

The wear volume loss of the Ti6Al4V pins was determined by measuring the change in length of the pins using a micrometer. The pins were measure after every 10 meters of the 100 meters sliding distance.

The R-square value is an indicator of how well the data fits the model. In this case, to a linear trend line fitted to each data set that originates at zero. The values calculated in Microsoft Excel showed that the data collected from the pin measurements fitted a linear trend line very closely. The majority of the values were above 0.97. A couple of values were slightly lower, but still above 0.9. Considering these values, it was concluded that the wear rate of the Ti6Al4V pins was close to linear.

Graphs depicting the friction coefficient are used for comparative purposes. The graphs are used to compare the friction coefficients of the different contract couples, and to that of the Ti6Al4V self-mated couple.

Optical microscopy was used to compare the wear on pins. Two images are used to analyse the wear; one at 100X magnifications and the other taken at 200X magnification.

SEM images and EDS analysis were used to investigate the wear mechanism taking place on the base materials used in the sliding experiments.

4.2.1 Ti6Al4V Self-mated Contact Couples

Figure 4.13 is a graph depicting the wear volume loss over sliding distance for the Ti6Al4V pins in contact with a Ti6Al4V base. The three lines are the wear volume loss for the various normal forces used in the study. The graph depicts the three line's final values in ascending order; 10N, 30N and 50N. In the case of the most wear volume loss the contact couple had a normal force of 50N applied. The increase in normal force, increase the wear volume loss, this is in accordance with the findings of Molenari [***13***]. The volume loss was in the region of 0.75mm^3 for the 100m sliding distance.

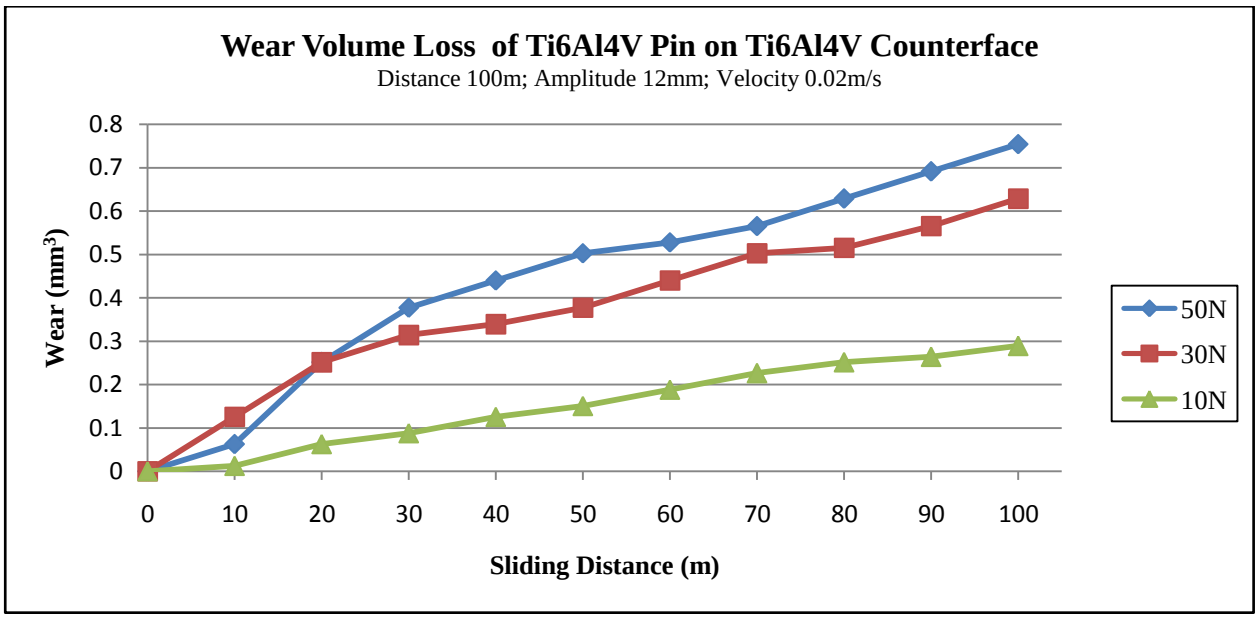

Figure 4.13: Wear volume loss [mm^3] of Ti6Al4V pins coupled Ti6Al4V with varying normal force

The three friction coefficients shown in Figure 4.14 represent the varying normal forces for self-mated Ti6Al4V contact couples. Two of the graphs, 50N and 30N, have run-in periods, smoothing out at a sliding distance of 10m for the 50N and 20m for the 30N graph. The 10N graph fluctuates over the entire 100m sliding distance. From this distance, the graphs follow each other till the end of the experiment. The steady state value of the 50N and 30 N graphs varies around the value of 0.32. The fluctuation of the graph depicting the contact couple with a 10N force can possibly be attributed to the force being too low and thus small vibrations moving through the apparatus.

The SEM and EDS analysis of the couple with a normal force of 10N, Figure 4.15, show that there are high levels of oxygen on the surface of the Ti6Al4V base material. As discussed in Section 2.31 titanium an its alloys have a high affinity for oxygen. The result of this is an adherent surface oxide, but a form of TiO_2 acts as a solid lubricant [***33***].

It can be concluded that an oxidative wear mechanism was present as described by various authors [***13***,***14***,***36***]. Further SEM, EDS and optical microscopy analysis was conducted on the Ti6Al4V self-mated couples with normal forces of 50N and 30N. The results were similar to those discussed and are available in Appendix A section A.1.

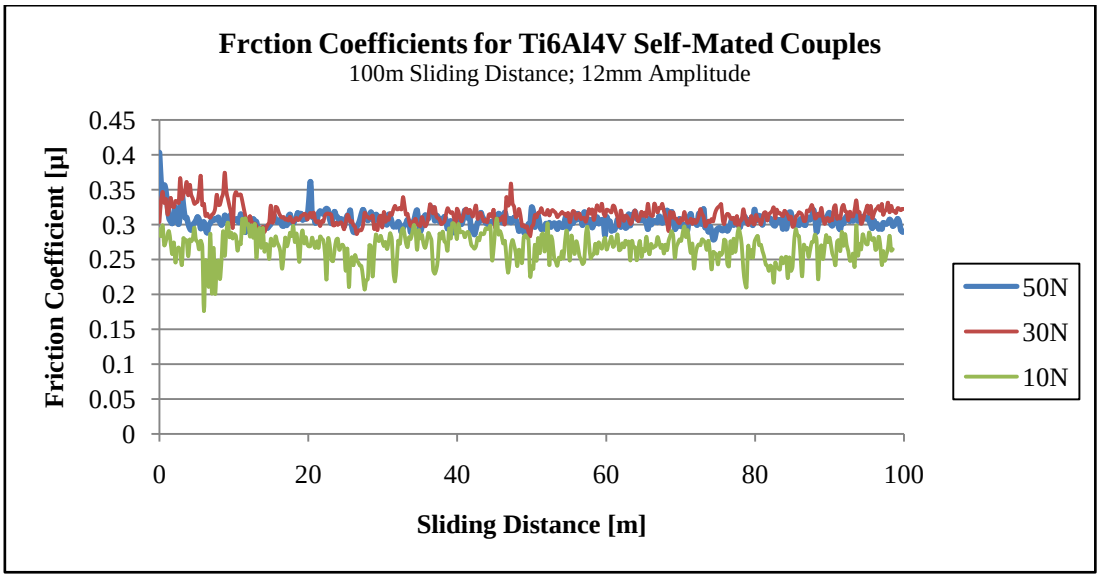

Figure 4.14: Comparison of friction coefficients of Ti6Al4V in self-mated couples with various normal forces

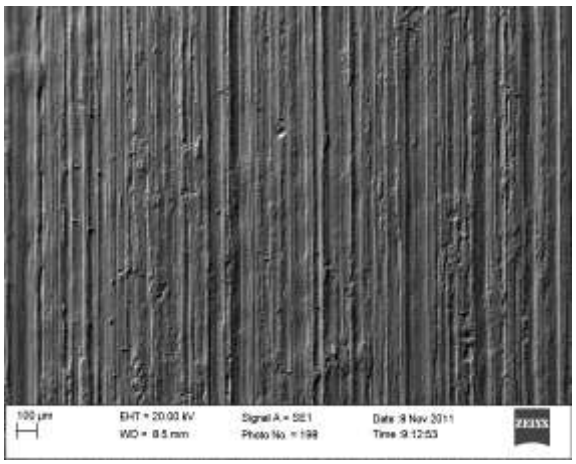

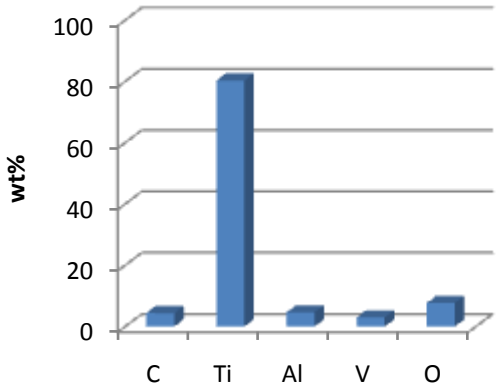

a)

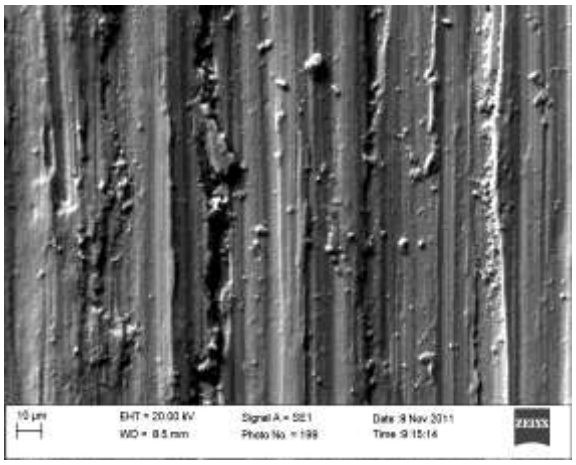

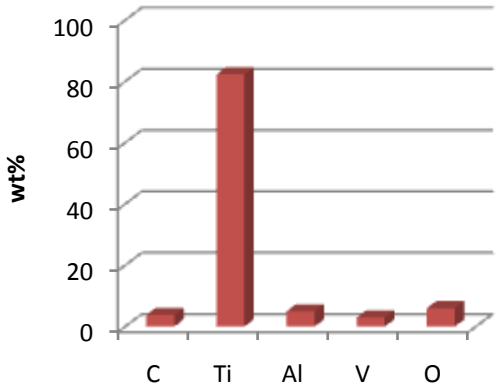

b)

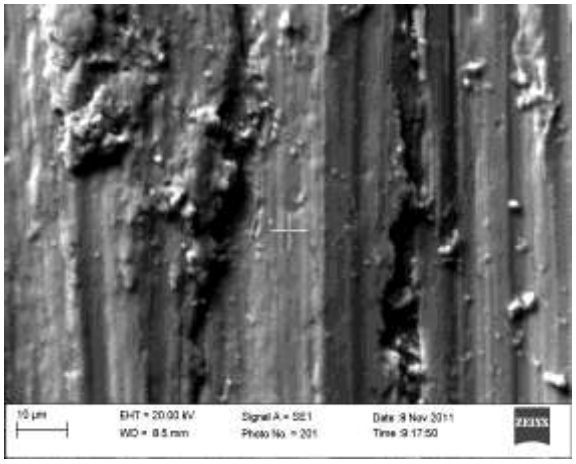

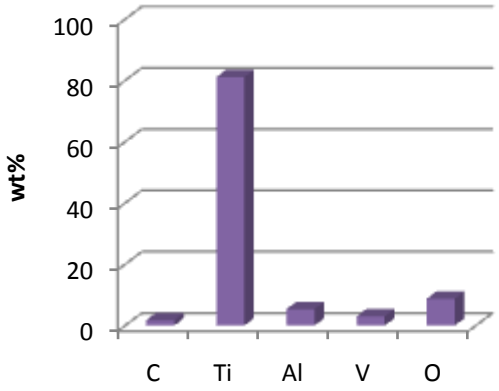

c)

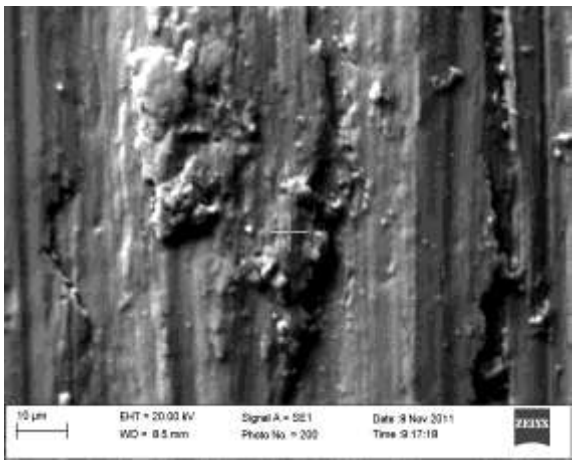

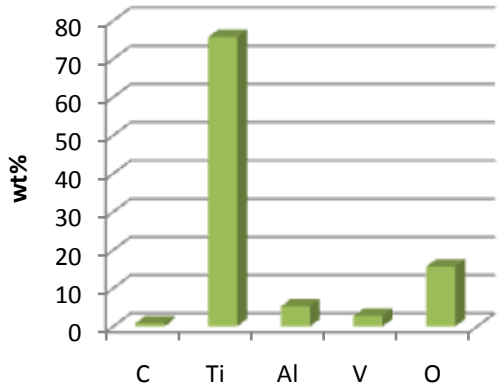

d)

Figure 4.15: SEM images of Ti6Al4V/Ti6Al4V contact couple with an applied normal force of 10N; a) 40X area analysis, b) 500X area analysis, c) 500X spot analysis of surface, d) 500X spot analysis of surface formations

Table 4.5: Quantitative results for Ti6Al4V/Ti6Al4V contact couple (Figure 4.15)

	Element [wt%]				
Figure 4.15	**C**	**Ti**	**Al**	**V**	**O**
a)	4.40	80.32	4.61	2.99	7.68
b)	3.75	82.33	4.97	2.94	6.02
c)	1.73	81.09	5.36	3.02	8.79
d)	0.78	75.66	5.20	2.71	15.64

a) b)

Figure 4.16: Microscope images of the Ti6Al4V pin couple on Ti6Al4V with a normal force of 10N; a) 100X MAG, b) 200X MAG

4.2.2 Ti6Al4V/Inconel 718 Contact Couples

Figure 4.17 are the wear volume loss graphs of the Ti6Al4V pins couples with Inconel 718. The wear volume agrees with the trend, that an increase in normal force leads to an increase in wear. The pin, on which a normal force of 50N was applied, showed the largest amount of wear with a value of around 2mm^3. At the other end, the pin coupled with a force of 10N was measured to have a wear volume loss of under 0.5mm^3. Comparing these graphs with those in Figure 4.13 (Ti6Al4V self-mated couple), it can be seen that the wear loss of the Ti6Al4V pin was much greater in the case of an Inconel 718 counterface. One reason for this could be that the Inconel is a harder material.

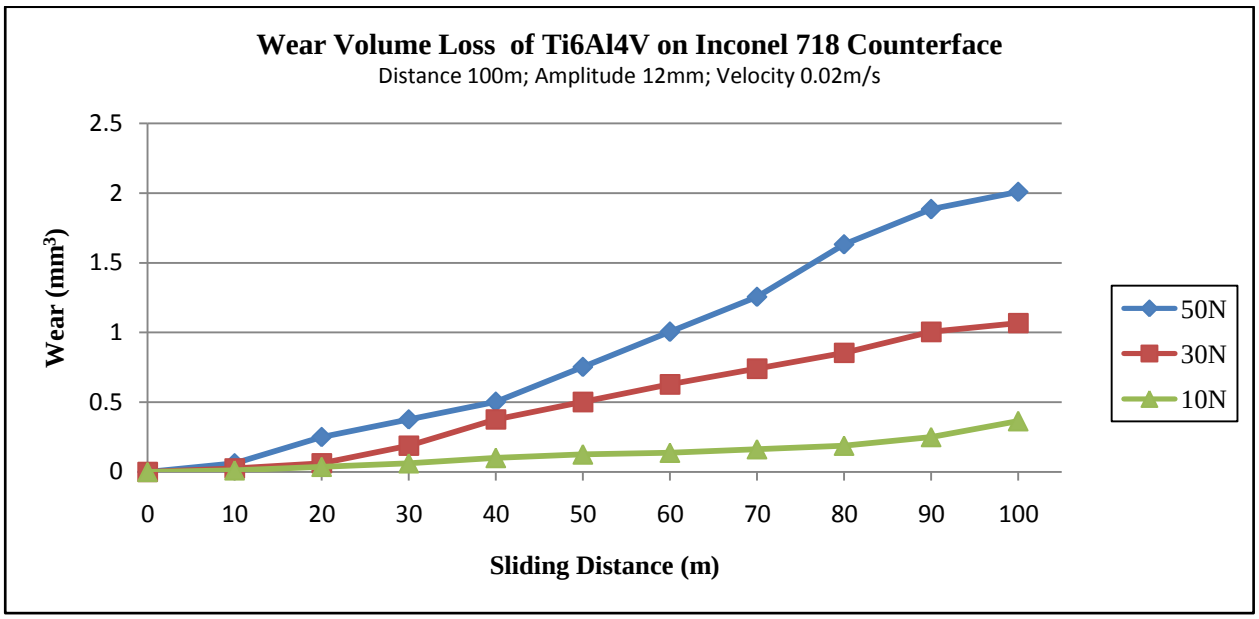

Figure 4.17: Wear volume loss [mm^3] of Ti6Al4V pins coupled with Inconel 718 with various normal forces

Figure 4.18 depicts the different coefficient of friction graphs for the Ti6Al4V/Inconel 718 contact couples with different normal forces. In each case, the Ti6Al4V pin coupled with Inconel has a higher friction coefficient than the Ti6Al4V self-mated couples. The fluctuations in the graphs are also more than those in the self-mated couple. As the force is increased the fluctuations decrease in all the graphs. In all three cases of the Ti6Al4V/Inconel 718 contact couple the coefficient is between 0.3 and 0.4. Only in the case of the 50N applied force on the contact couple is a run-in period present. The period ends at approximately 20m.

The SEM images and EDS analysis are recorded in Figure 4.19 and Table 4.6. On the surface of the Inconel 718 base material it seems like small droplets have formed, as well as, larger sections where material has been welded to the surface. A spot analysis was performed on one of these areas and from this it was confirmed that titanium did adhere to the surface. Oxygen was also found to be present in a large percentage. From this information it can be determined that oxidation took place. It is possible that an oxide layer formed that adhered to the Inconel base material.

Optical microscope images of the Ti6Al4V pin are included in Figure 4.20. The images show that material has been removed from the pins and this in accordance with the wear volumes measured. Scuffing, and the more severe form galling, took place on the surface of the pin.

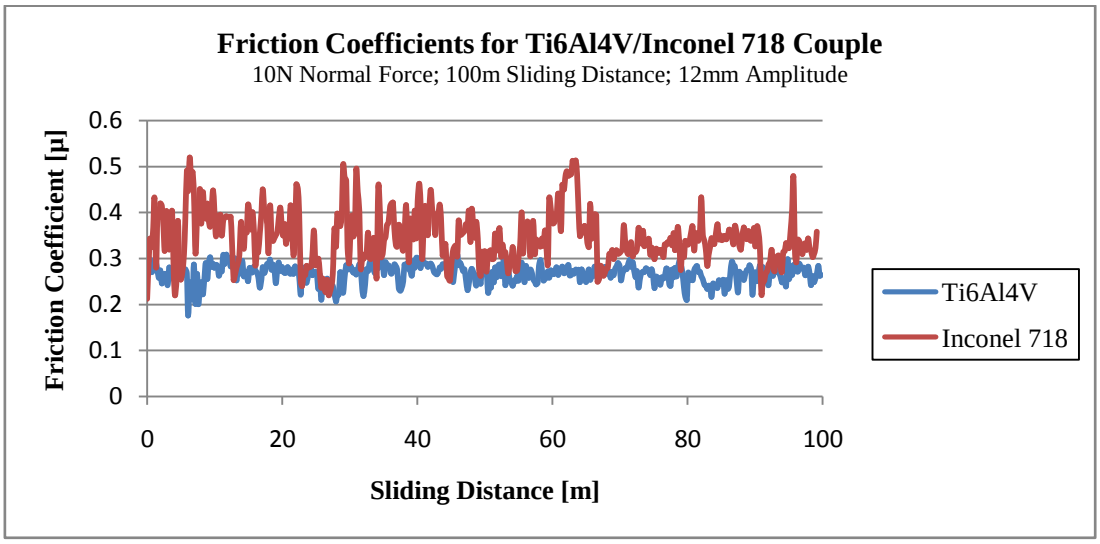

a)

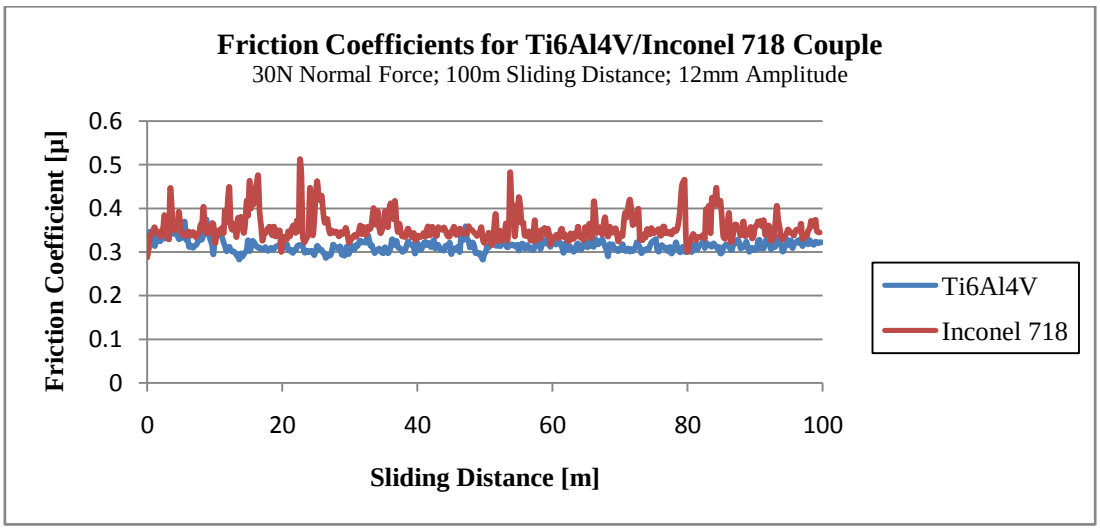

b)

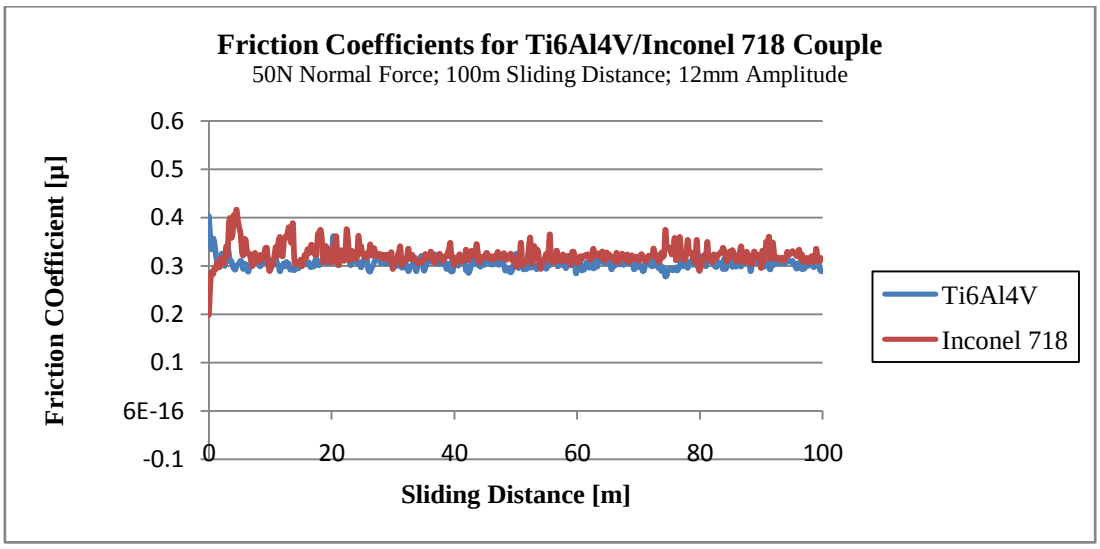

c)

Figure 4.18: Comparison of friction coefficients of Ti6Al4V sliding against counterface materials Ti6Al4V and Inconel 718 with normal forces a) 10N, b) 30N, and c) 50N

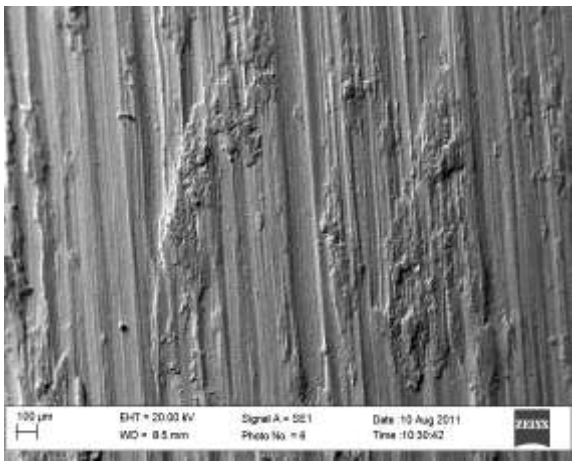

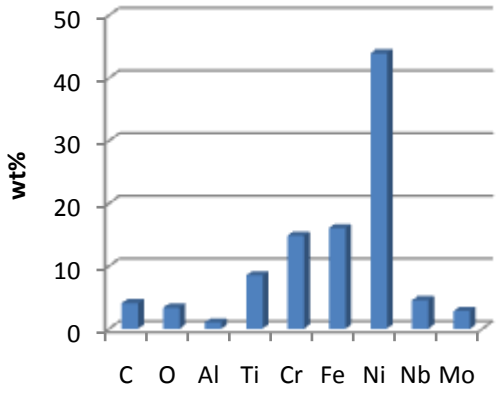

a)

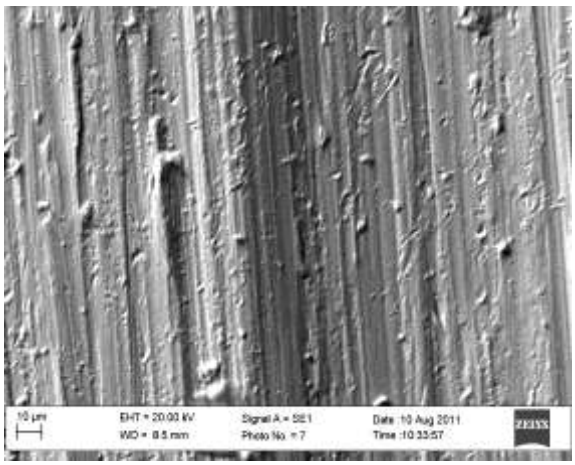

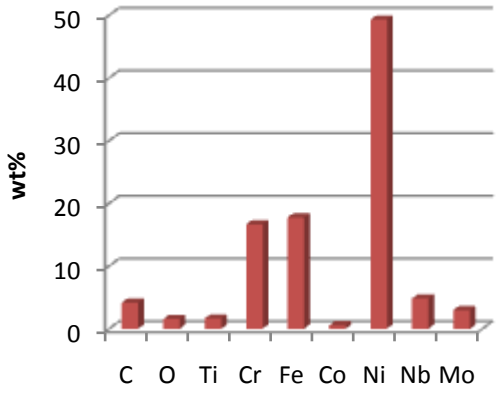

b)

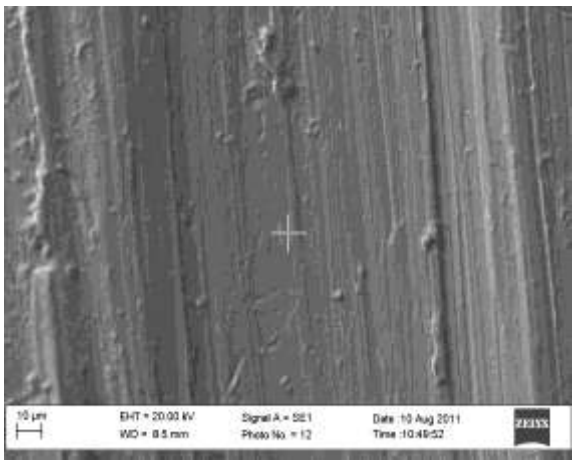

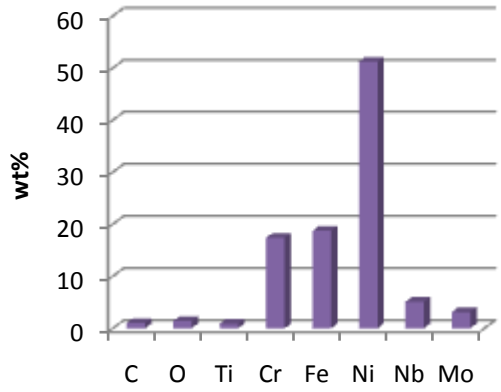

c)

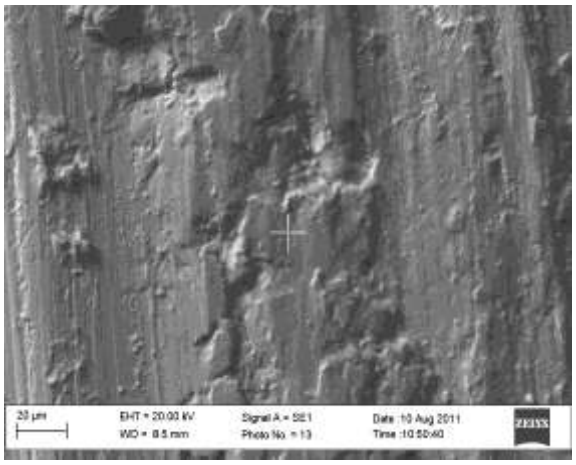

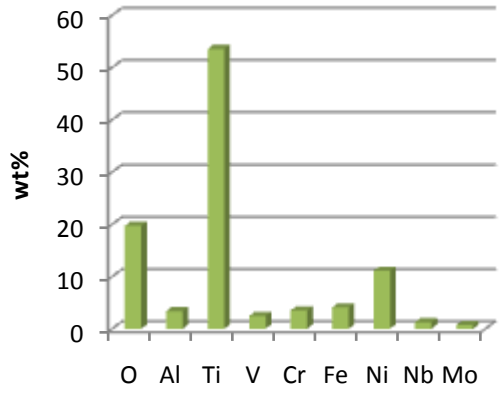

d)

Figure 4.19: SEM images of Ti6Al4V/Inconel 718 contact couple with an applied normal force of 30N; a) 40X area analysis, b) 500X area analysis, c) 500X spot analysis of surface, d) 500X spot analysis of surface formations

Table 4.6: Quantitative results for Ti6Al4V/Inconel 718 contact couple (Figure 4.19)

	Element [wt%]										
Figure 4.19	**C**	**O**	**Al**	**Ti**	**V**	**Cr**	**Fe**	**Co**	**Ni**	**Nb**	**Mo**
a)	4.06	3.35	0.98	8.49		14.83	16.04		44.89	4.55	2.81
b)	4.14	1.55		1.62		16.63	18.66	0.55	49.10	4.82	2.94
c)	1.04	1.4		0.90		17.39	19.29		51.76	5.09	3.12
d)		19.68	3.35	53.92	2.44	3.51	4.05		11.07	1.26	0.73

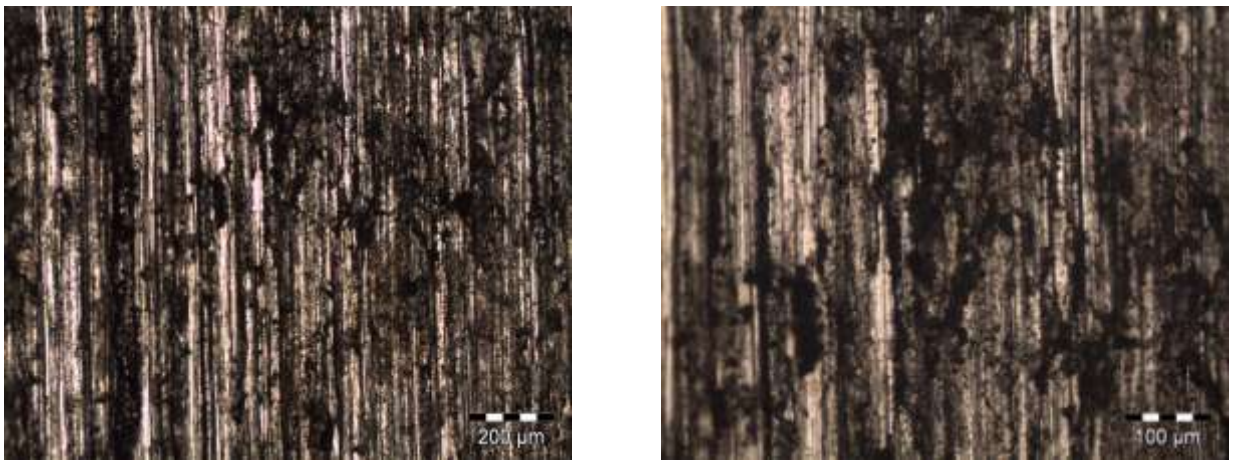

a) b)

Figure 4.20: Microscope images of the Ti6Al4V pin couple with Inconel 718 with a normal force of 30N; a) 100X MAG, b) 200X MAG

4.2.3 Ti6Al4V/Cemented Carbide Contact Couples

A polishing effect was found to occur at the start of the test, and was accompanied by a high frequency noise [***81***]. The experiments conducted by Bonny [***81***], with a carbide-on-carbide experimental setup, showed that the friction reached a stable, slightly fluctuating value for remainder of the experiment. The authors attributed this phenomenon to polishing in the initial stage of wear testing. A smooth wear track surface was formed by means of ploughing away the surface asperities or original surface roughness. In the later stages of the experiment, it was found that the wear track became smoother and that the coefficient of friction stabilized [***15***,***81***].

The fluctuating friction curve was attributed to the continuous breaking and regenerating micro-junctions. This indicated a continuously changing interaction (interlocking) at the pin-on-flat contact surface [***81***]. As described in the literature the origin of friction has two components; the first is one of adhesion and the second abrasion. The experiments performed by Bonny [***81***], the abrasion component was gain split into a micro- and macro component. The micro component was described in terms of asperity interaction and the macro in terms of the penetration of the pin into the counter surface. The macro component was considerable during the start of the test until the wear track was formed on the surface. The micro-component or micro-ploughing was more related to surface roughness. Rough surface in contact results in at least one of the surfaces becoming smoother. The smoother the surface the fewer obstacles that have to be overcome and this will decrease the tangential force needed to maintain sliding. In turn, this will decrease the friction between the surfaces. [***81***]

Bonny [***81***] found that the coarsest grained carbides caused the largest wear rate. From literature it was noted that wear resistance of a carbide increases with reduced carbide grain size and decreased binder content and thus with increased hardness.

The wear debris was found on the outer extensions of the wear track, occasionally inside, along and adjacent to the wear scar [***81***]. Due to plastic deformation exceeding the plasticity limit of the material wear debris was formed [***81***]. The cracks that initiated at sliding interface intersected with the cracks that propagate due to the sliding contact. From this, fine chunks of material were found to detach and were crushed into finer wear debris particles. The wear debris in a sliding contact has considerable influence [***81***].

Figure 4.21 is a graph depicting the wear volume loss over sliding distance for the pins at a load of 10N. The graph shows that the wear volume of all three pins were much the same. The most wear took place when the Ti6Al4V pin was in contact with the CS carbide. The volume loss was in the region of 0.7mm^3 for the 100m sliding distance. As previously stated all three wear volume graphs are close to linear in Figure 4.21.

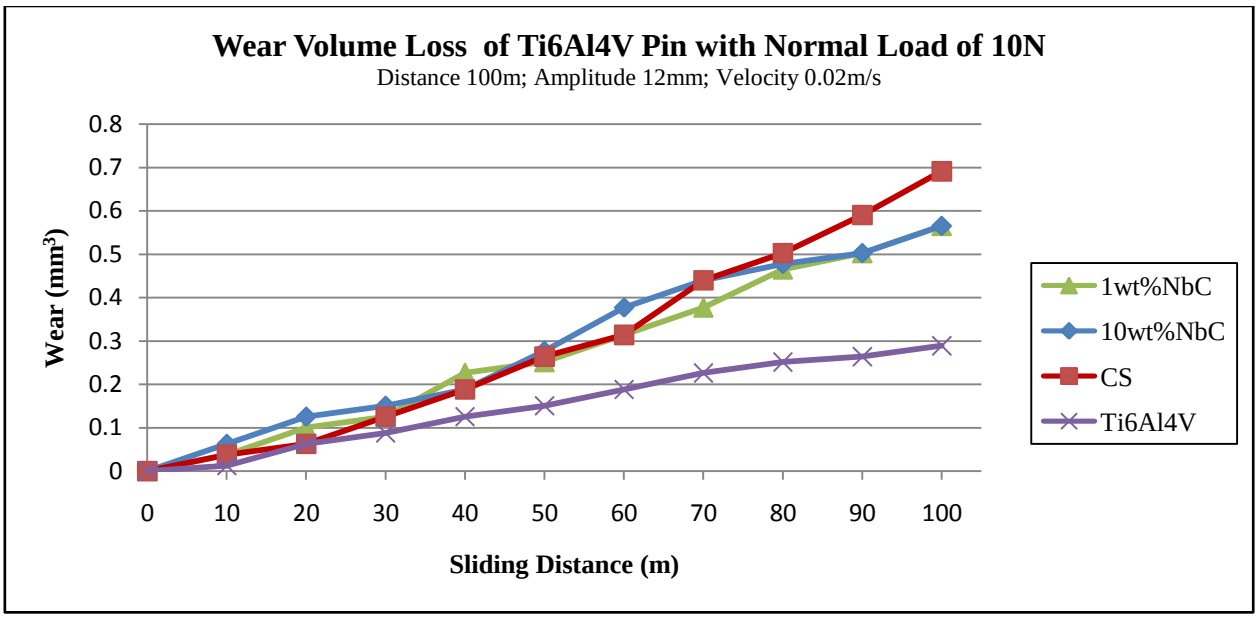

Figure 4.21: Wear volume loss [mm^3] of Ti6Al4V pins coupled with different carbides with a normal force of 10N

Figure 4.22 a) – c) shows the different friction coefficients of the contact couples all with a normal force of 10N. Figure 4.22 a) represents the coefficient of friction graph for the 1wt%NbC cemented carbide. A run-in period does exist and ends at 15m. In Figure 4.22 b) it is very difficult to see a run-in period because of the large fluctuations. Figure 4.22 c) has a definite run-in period. The graph does not stabilise, but has cycles from high to low throughout the total sliding distance. In all three graphs the friction coefficient is higher in the case of the cemented carbides compared to that of Ti6Al4V self-mated couples. The collection of SEM images and EDS analysis are shown in Figure 4.23. The images show the CS carbide that was coupled with the Ti6Al4V pin. The images show that very little wear has taken place on the carbide. Scratches can be observed on the surface. In Figure 4.23 b), c) and d) it appears that drops of material have formed on the surface. A further EDS spot analysis concluded that these drops were about 95% titanium (Figure 4.23 d) and Table 4.7). The surfaces in between were made up of the carbide (Figure 4.23 c) and Table 4.7). These mounds of titanium on the surface were most probably caused by adhesion during sliding. The instability of

the friction coefficient could be a result of this, as the surface roughness could increase and is fluctuating. It is possible that an interlocking motion was caused the tangential force to increase and then decrease considerably. Figure 4.24 are the images taken by the microscope of the Ti6Al4V pins. The images show large wear tracks on the surface and galling. The pieces of material removed from the pins have adhered to the carbide surface as shown by the SEM and EDS analysis. Some of this material was also part of the wear debris.

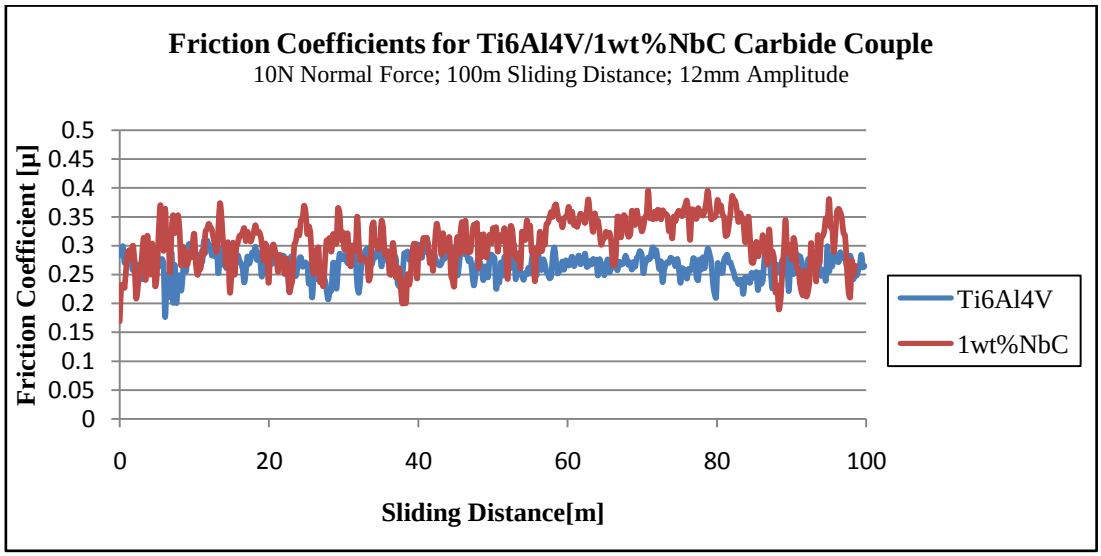

a)

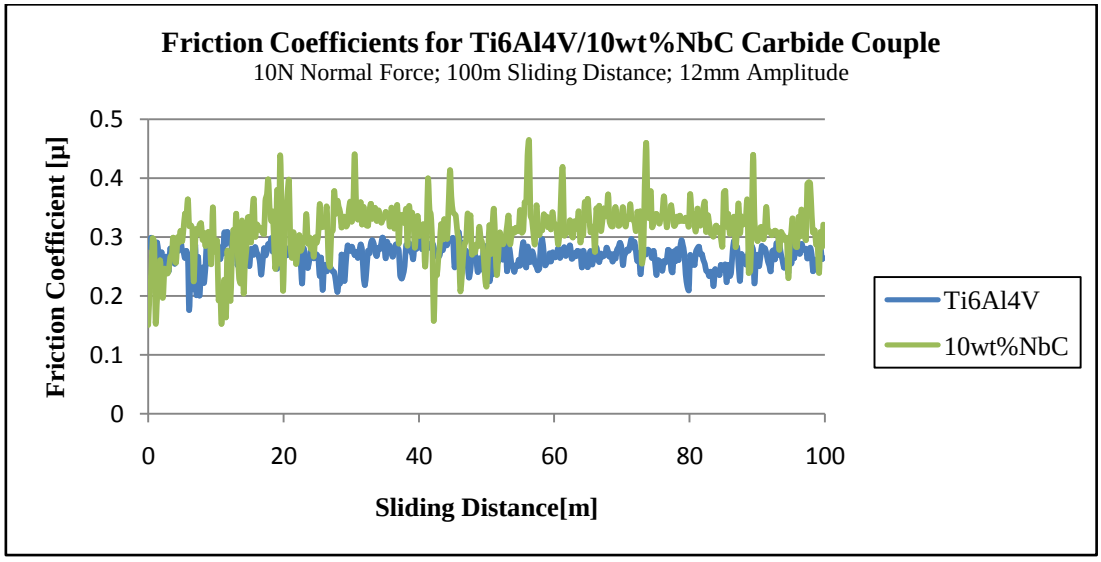

b)

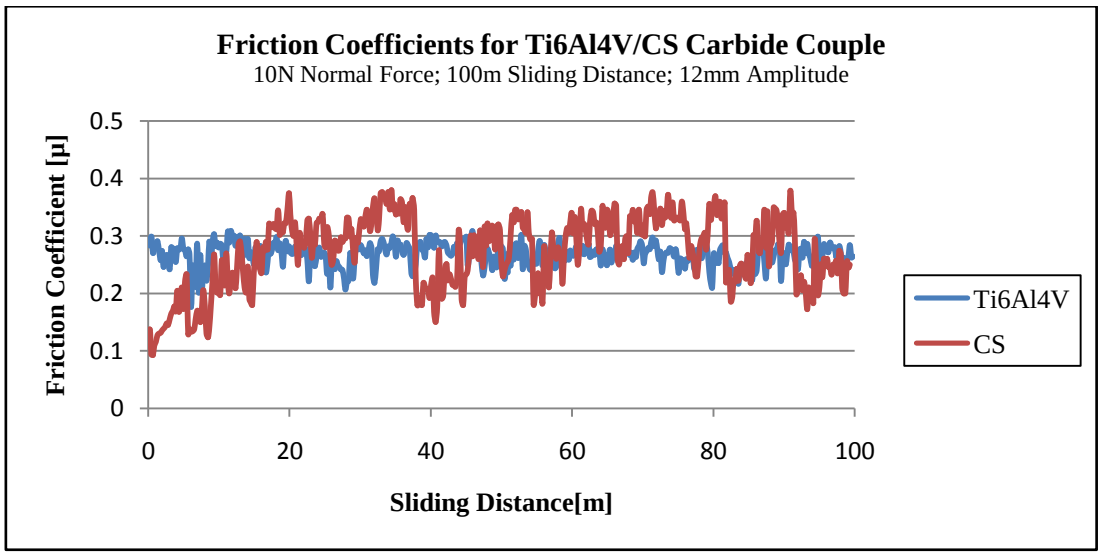

c)

Figure 4.22: Comparison of friction coefficients of Ti6Al4V, with normal force 10N, sliding against cemented carbide counterface materials, a) 1wt%NbC, b) 10wt%NbC and c) CS carbide

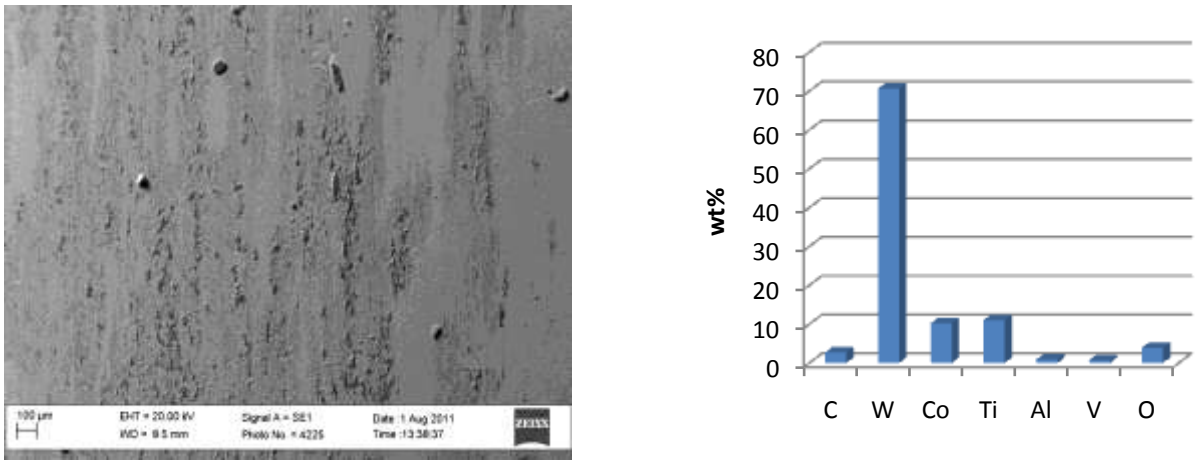

a)

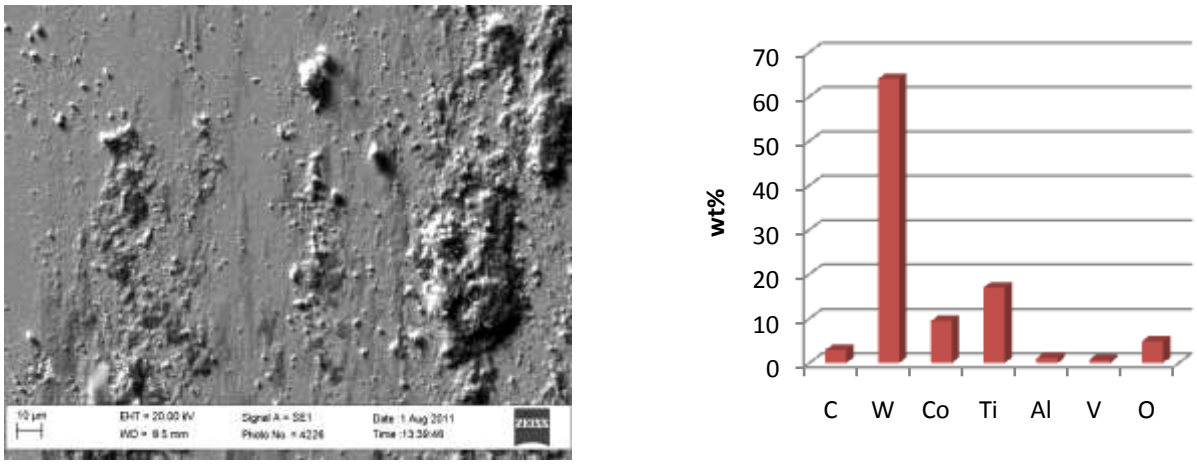

b)

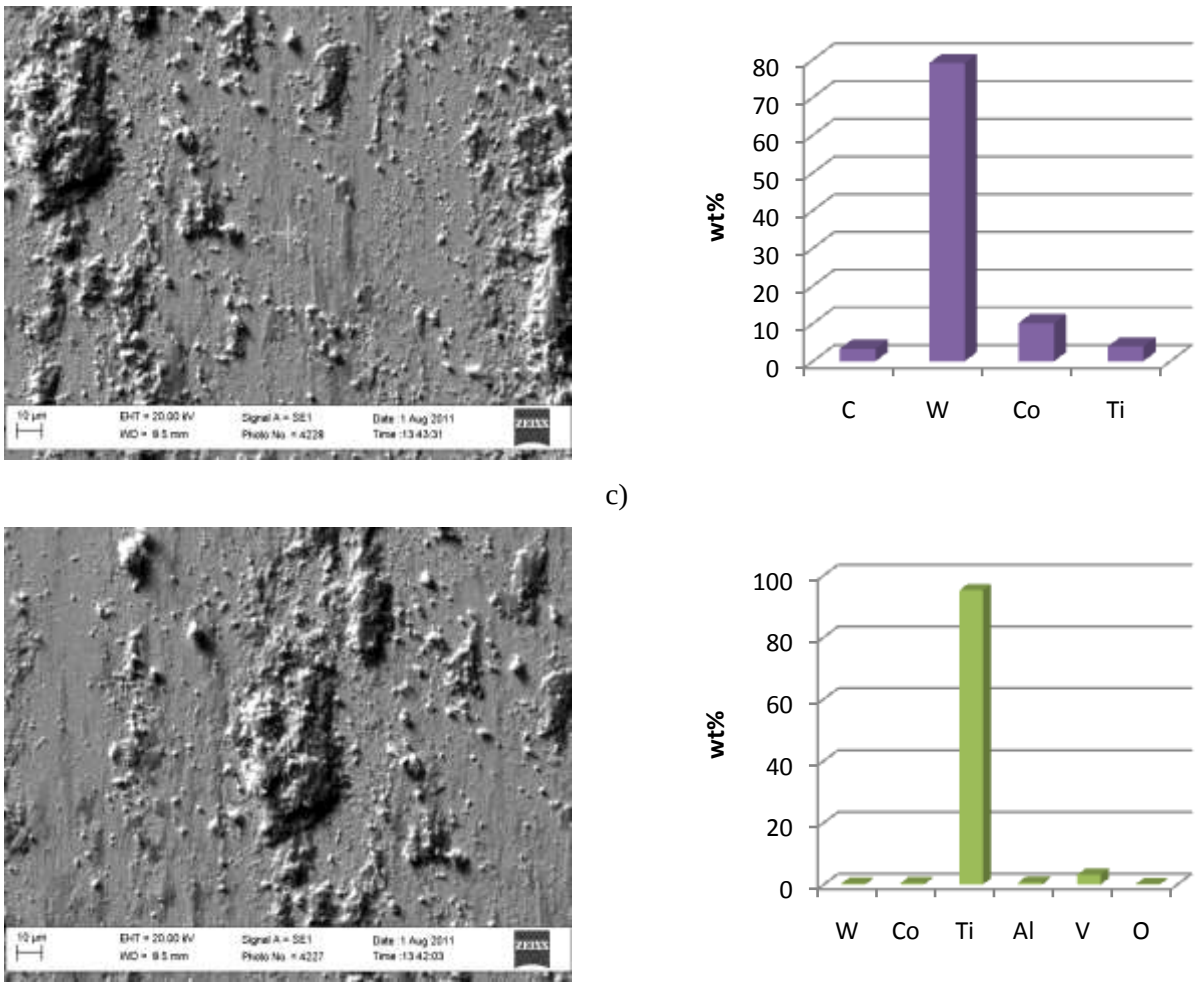

Figure 4.23: SEM images of CS/Ti6Al4V contact couple with an applied normal force of 10N; a) 40X area analysis, b) 500X area analysis, c) 500X spot analysis of surface, d) 500X spot analysis of surface formations

Table 4.7: Quantitative results for CS/Ti6Al4V contact couple (Figure 4.23)

	Element [wt%]						
Figure 4.23	**C**	**W**	**Co**	**Ti**	**Al**	**V**	**O**
a)	2.70	70.63	10.20	11.02	0.87	0.67	3.90
b)	2.89	64.00	9.45	16.99	1.09	0.71	4.87
c)	3.28	79.07	10.11	3.92	0.00	0.00	3.62
d)	0.00	0.33	0.44	95.17	0.69	3.16	0.20

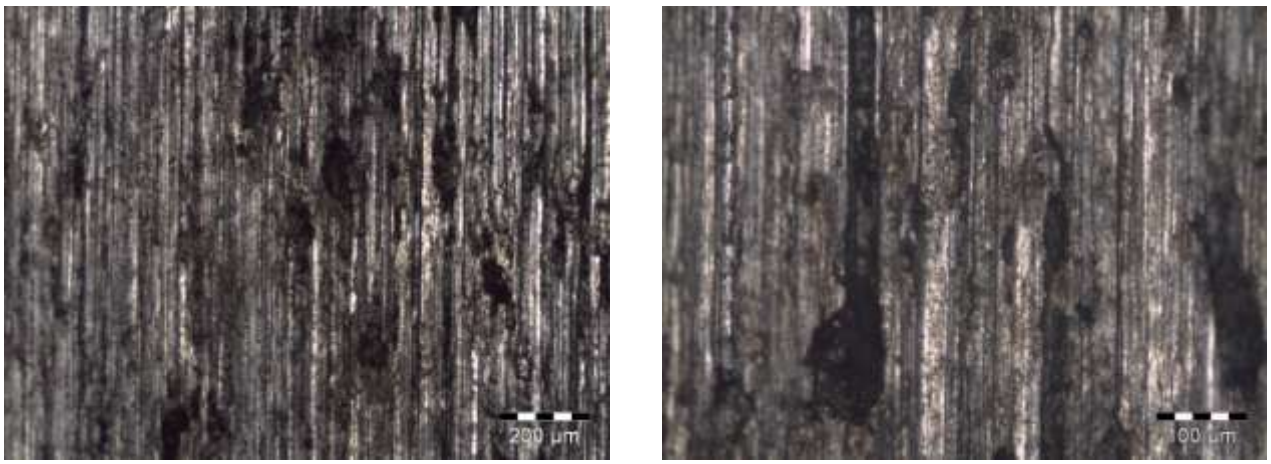

a) b)

Figure 4.24: Microscope images of the Ti6Al4V pin couple with CS carbide with a normal force of 10N; a) 100X MAG, b) 200X MAG

Figure 4.25 a) – c) depicts the volume loss [mm^3] as a result of sliding on the Ti6Al4V pins coupled with four different materials, each with a normal force of 30N. From the figure, the pin coupled with the CS carbide had the largest wear volume loss with a value slightly above 2 mm^3. It is possible that this is a direct result of the higher hardness of the material. The two pins coupled with the SPS carbides showed much the same results. The total volume worn away for both was in the region of 1.5mm^3. The wear of Ti6Al4V pin in a self-mated couple showed lower wear.

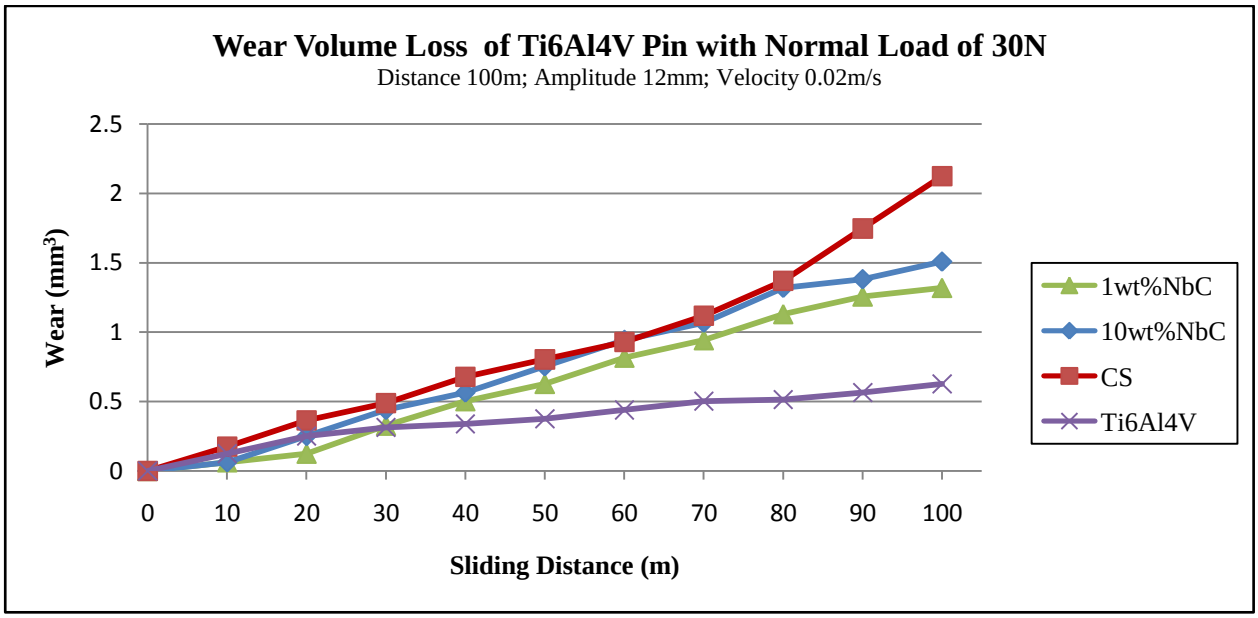

Figure 4.25: Wear volume loss [mm^3] of Ti6Al4V pins coupled with different carbides with a normal force of 30N

Figure 4.26 depicts the friction graphs with regard to sliding distance with a normal force of 30N. These graphs show less fluctuation than the previous set that was studied with at a load of 10N. In this case, the CS

carbide has the most stable friction coefficient and a running-in period can be seen, with the friction coefficient stabilising at 10 – 15m, at a value of ±0.38.. The two SPS carbides fluctuate, from the beginning, but are more stable than the previous experiment. The SEM images and EDS analysis (Figure 4.27 and Table 4.8), demonstrate that a Ti film has formed on the carbide surface compared to the droplets of the previous experiments (10N force). The increase in normal load could be one of the reasons for this finding. The wear debris that was contained within the contact was most probably squashed and through an adhesion process formed this tribo-layer. Long [***34***] noted that the Ti alloy in question readily transferred worn material to the counter surface. The layer in turn acts as a solid-lubricant film. In all the EDS analysis' Ti was found on the surface. The images of the Ti6Al4V pins shown in Figure 4.28, also show signs of galling.

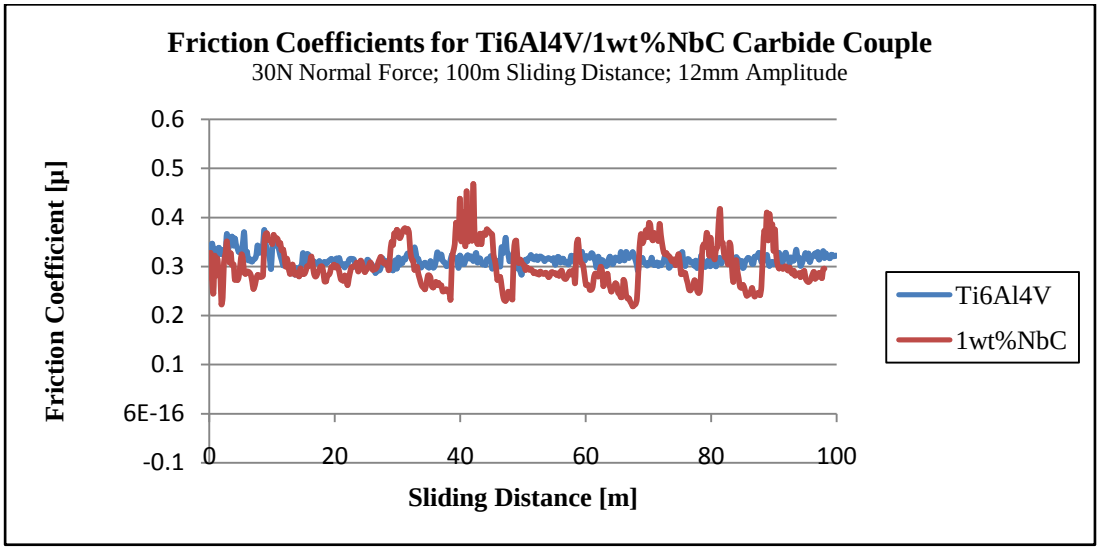

a)

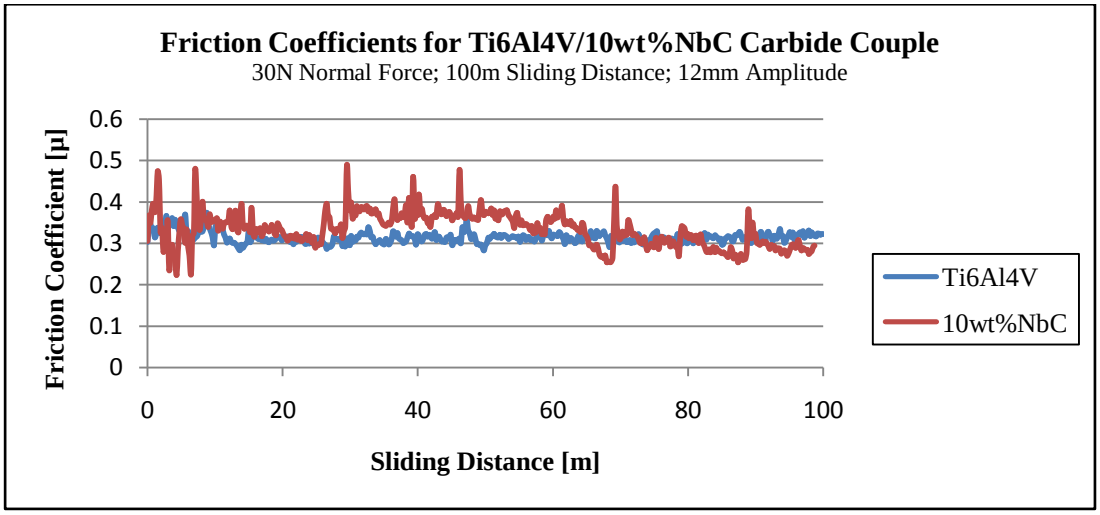

b)

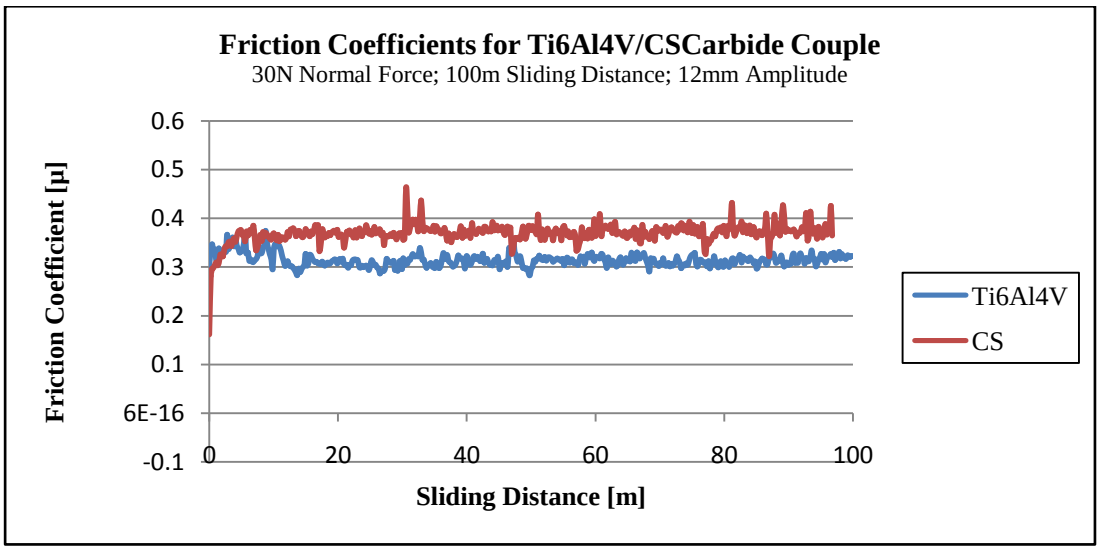

c)

Figure 4.26: Comparison of friction coefficients of Ti6Al4V, with normal force 30N, sliding against counterface materials Ti6Al4V, a) 1wt%NbC, b) 10wt%NbC and c) CS carbide

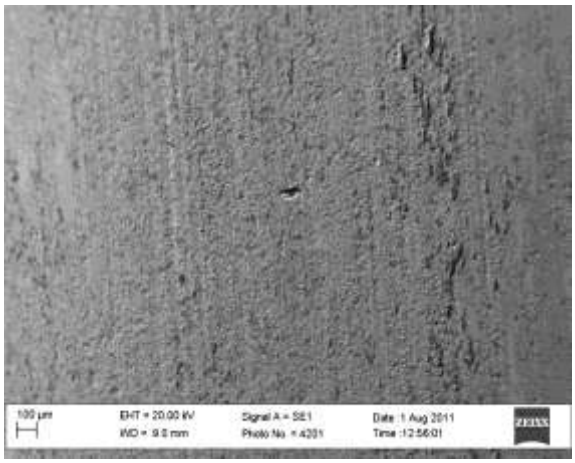

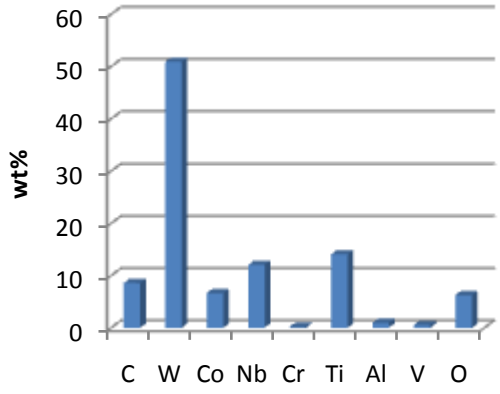

a)

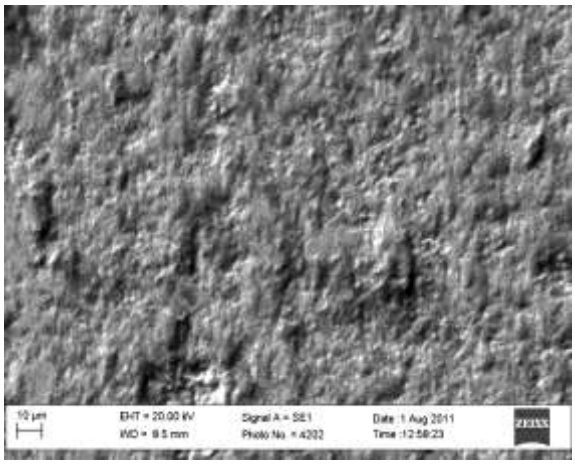

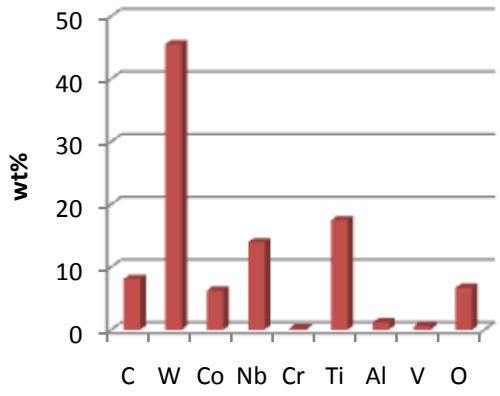

b)

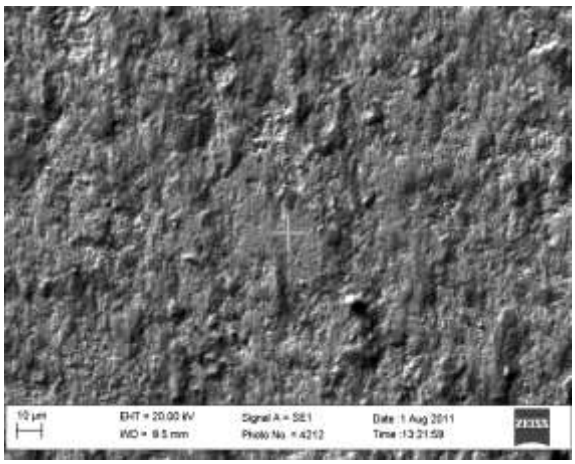

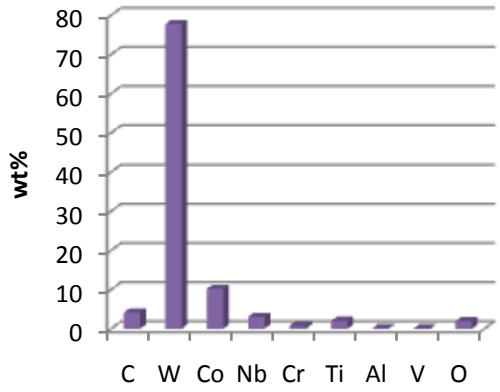

c)

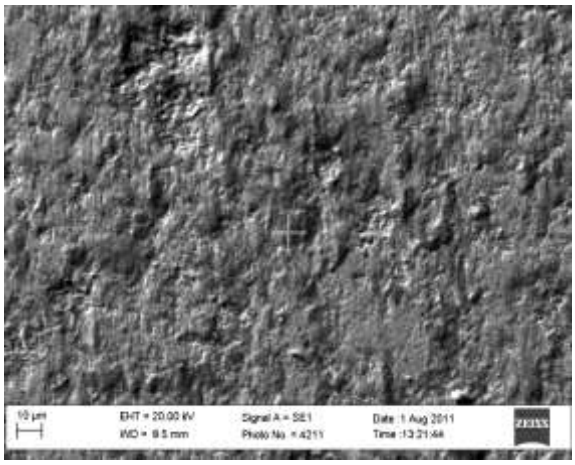

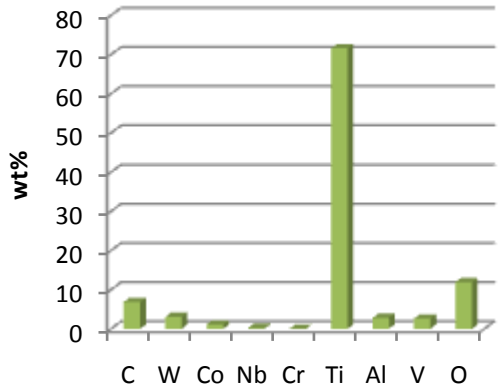

d)

Figure 4.27: SEM images of 1wt%NbC/Ti6Al4V contact couple with an applied normal force of 30N; a) 40X area analysis, b) 500X are analysis, c) 500X spot analysis of surface, d) 500X spot analysis of surface formations

Table 4.8: Quantitative results for 1wt%NbC/Ti6Al4V contact couple (Figure 4.27)

	Element [wt%]								
Figure 4.27	**C**	**W**	**Co**	**Nb**	**Cr**	**Ti**	**Al**	**V**	**O**
a)	8.55	50.88	6.60	12.01	0.19	14.05	0.97	0.53	6.22
b)	8.12	45.52	6.22	13.94	0.24	17.47	1.17	0.62	6.69
c)	4.14	77.73	10.15	3.01	0.76	2.00	0.14	0.12	1.95
d)	6.81	3.03	1.08	0.24	0.04	71.56	2.79	2.59	11.86

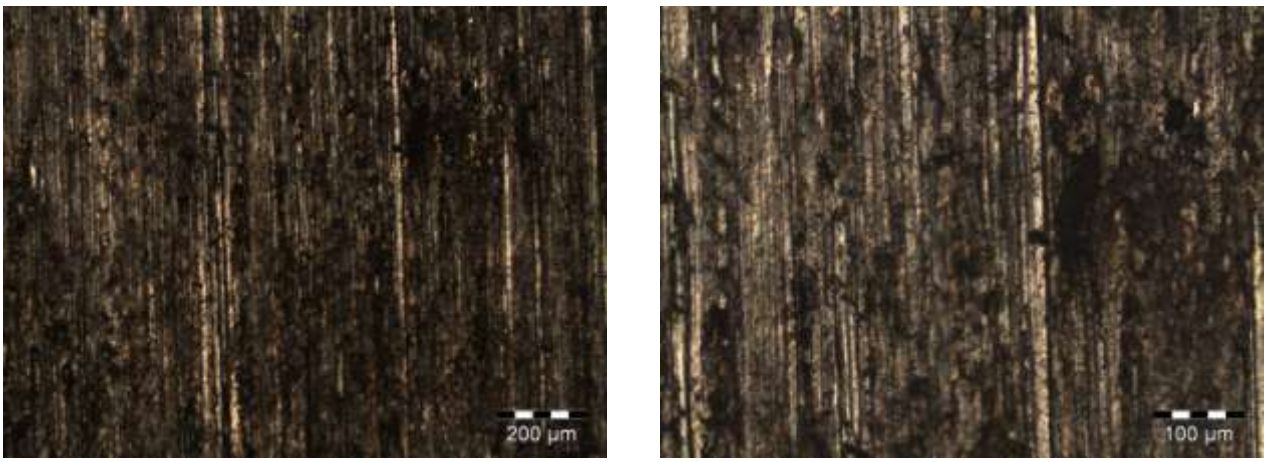

a) b)

Figure 4.28: Microscope images of the Ti6Al4V pin couple with 1wt%NbC carbide with a normal force of 30N; a) 100X MAG, b) 200X MAG

Figure 4.29 shows the graphs of the wear volume for the Ti6Al4V pins that were coupled with the different carbides with a normal force of 50N. The wear rates of the pins are linear in nature. The CS carbide has caused the most wear on the pin followed by the 10wt%NbC SPS carbide and finally the 1wt%NbC SPS carbide. This follows the pattern of the previous two sets of results.

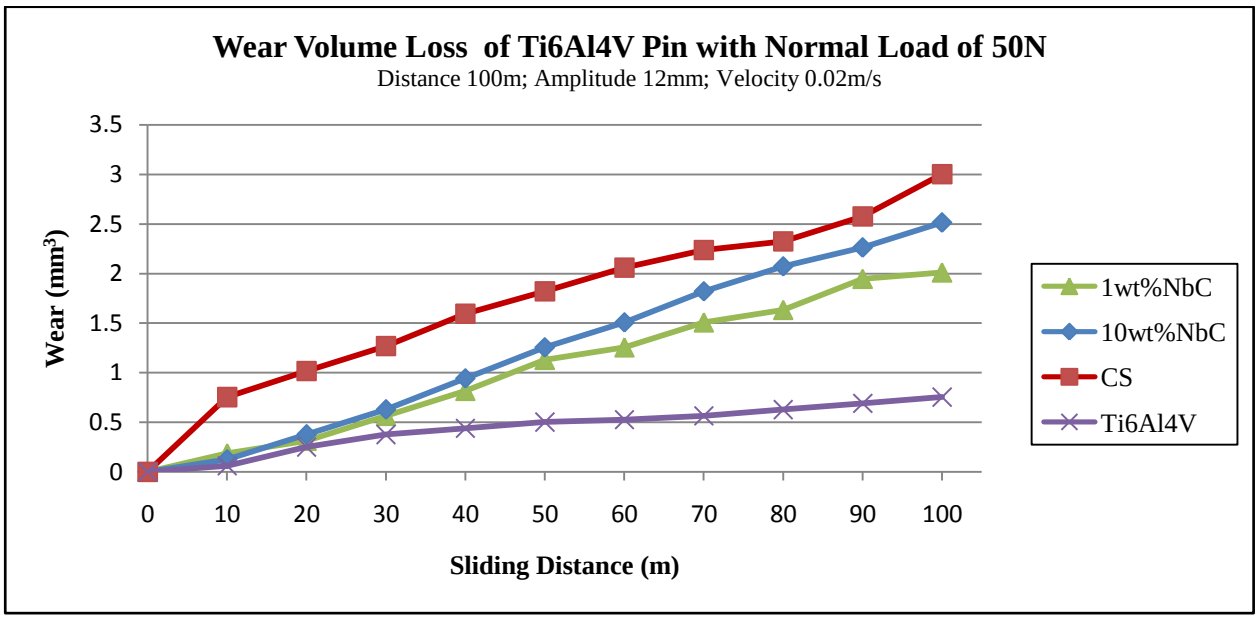

Figure 4.29: Wear volume loss [mm^3] of Ti6Al4V pins coupled with different carbides with a normal force of 50N

The friction graphs shown in Figure 4.30 a) to c) are again stable with the exception of the 1wt%NbC SPS carbide. The CS and 10wt%NbC carbides couple with the titanium pin show that each have a small running-in period from 0 to about 20 meters. From around about the 10m mark, the coefficient of friction stabilizes for these two contact couples until the end of the experiment. This is in accordance with what was discovered

by Bonny [***81***]. The SEM and EDS analysis in Figure 4.31 and Table 4.9 describe the surface of the 10wt%NbC/Ti6Al4V couple with a force of 50N. From area and spot analysis it is shown that Ti had definitely adhered to the surface. It can thus be concluded that adhesion took place. As in the case of the experiments done with a 30N normal force, the Ti on the surface was most probably caught in the contact interface and squashed. The microscope images of the couple are shown in Figure 4.32. From these images it can be seen that pieces of the Ti6Al4V pin were removed. Further SEM, EDS, and optical microscopy analysis are available in Appendix A section A.2 for the Ti6Al4V/carbide contact couples. The analysis revealed similar results to those discussed.

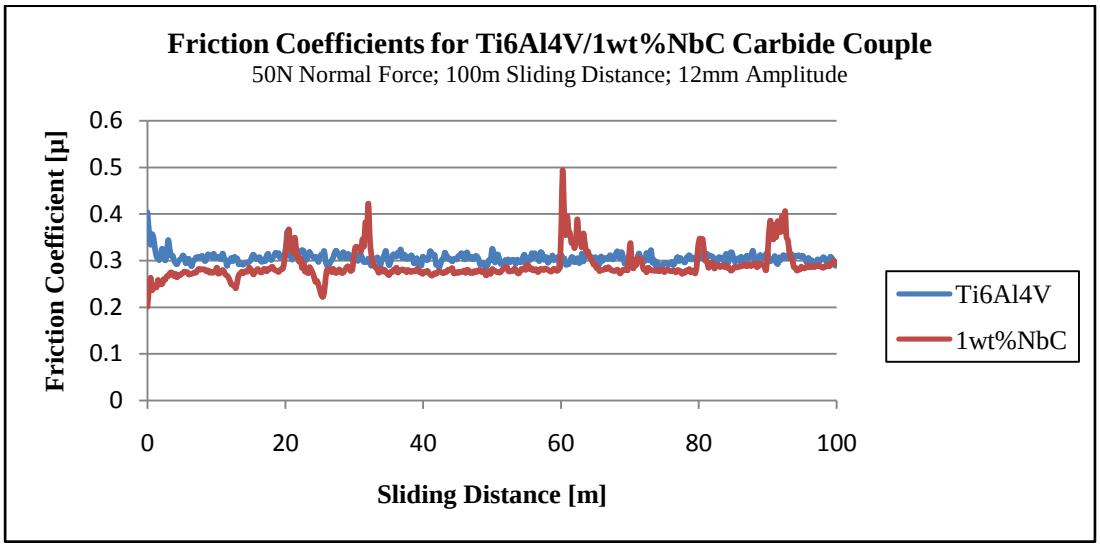

a)

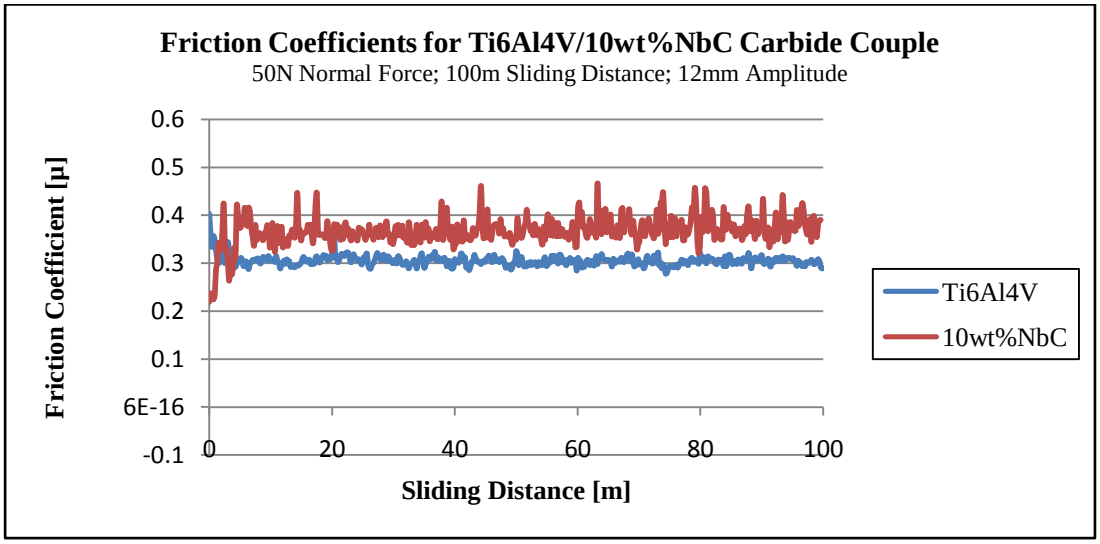

b)

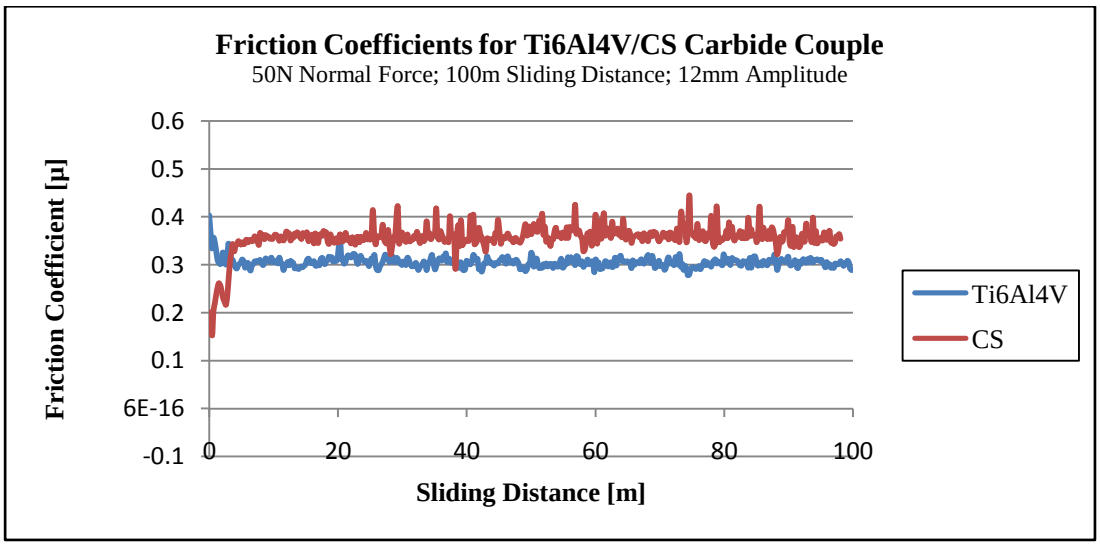

c)

Figure 4.30: Comparison of friction coefficients of Ti6Al4V, with normal force 50N, sliding against counterface materials Ti6Al4V, a) 1wt%NbC, b) 10wt%NbC and c) CS carbide

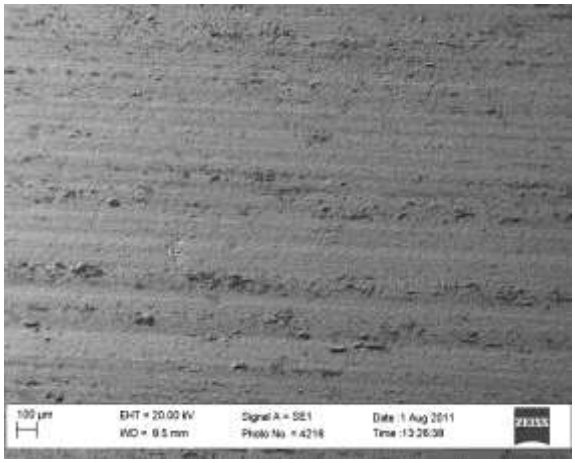

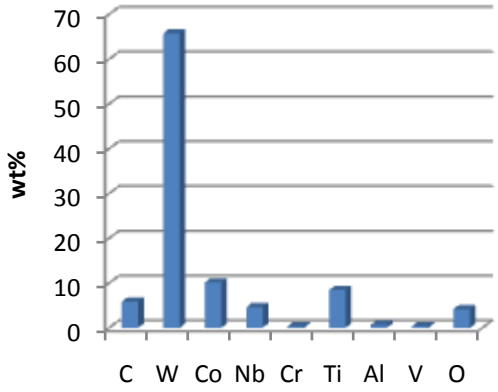

a)

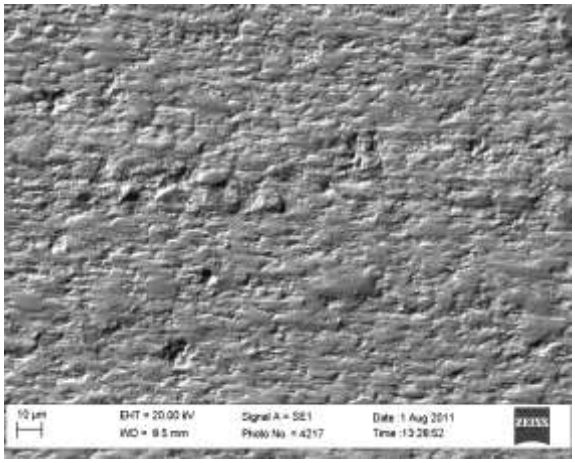

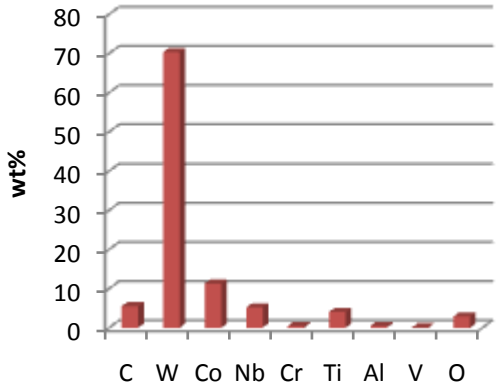

b)

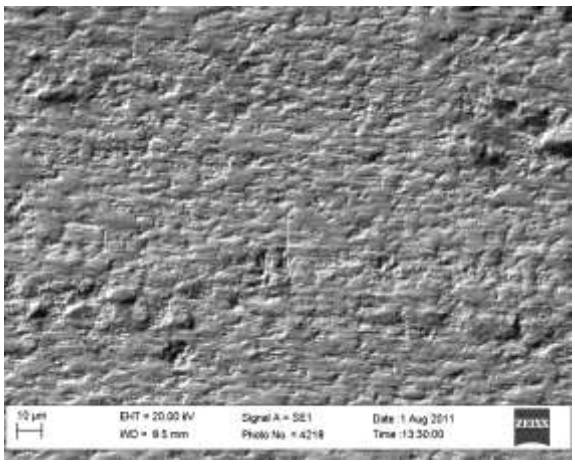

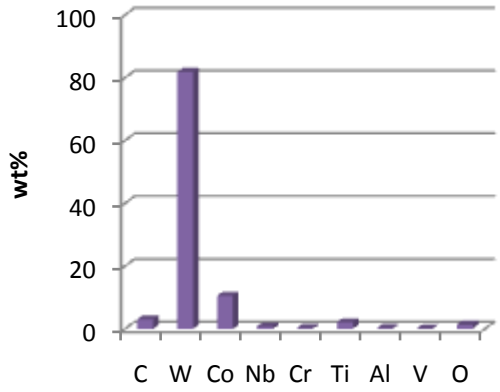

c)

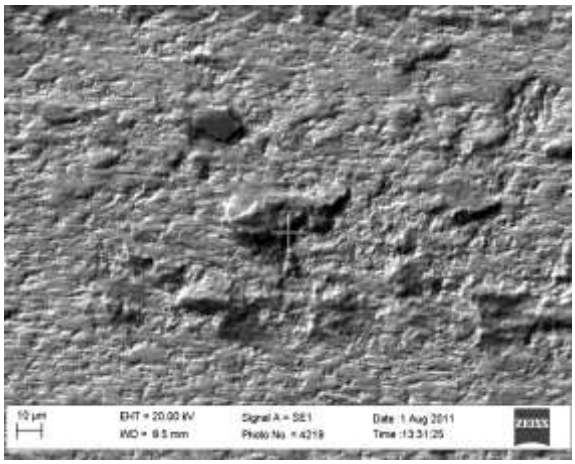

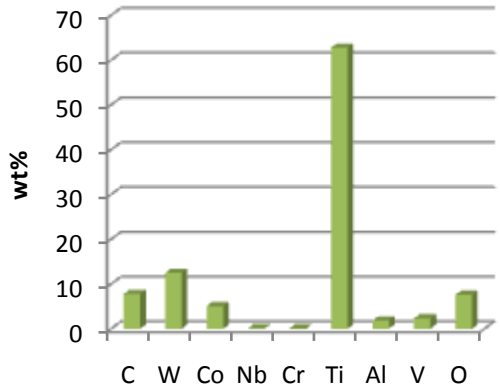

d)

Figure 4.31: SEM images of 10wt%NbC/Ti6Al4V contact couple with an applied normal force of 50N; a) 40X area analysis, b) 500X are analysis, c) 500X spot analysis of surface, d) 500X spot analysis of surface formations

Table 4.9: Quantitative results for 10wt%NbC/Ti6Al4V contact couple (Figure 4.31)

	Element [wt%]								
Figure 4.31	**C**	**W**	**Co**	**Nb**	**Cr**	**Ti**	**Al**	**V**	**O**
a)	5.81	65.67	10.10	4.55	0.34	8.42	0.64	0.35	4.13
b)	5.47	70.27	11.25	5.13	0.43	4.03	0.45	0.11	2.84
c)	2.98	81.81	10.49	0.75	0.23	2.08	0.23	0.14	1.29
d)	7.78	12.45	5.05	0.13	0.11	62.73	1.85	2.31	7.58

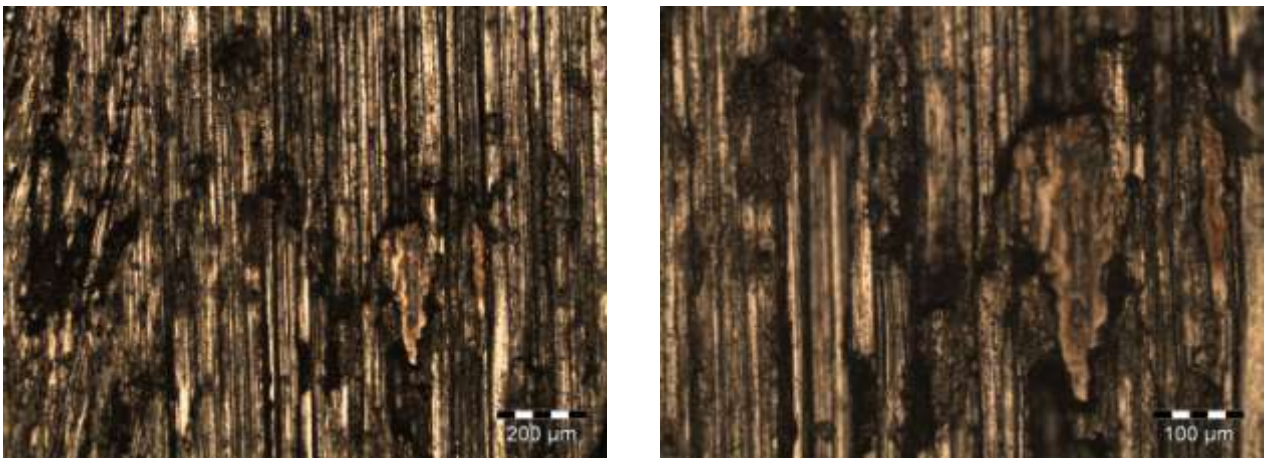

a) b)

Figure 4.32: Microscope images of the Ti6Al4V pin couple with 10wt%NbC carbide with a normal force of 50N; a) 100X MAG, b) 200X MAG

Figure 4.33 shows a mapping analysis of the surface of the 10wt%NbC SPS carbide. The experiment used a normal force of 50N. The map was used to conclude that adhesion took place and this was found to be true. The lighter the colour of the spectrum the more of the specific element is present. This is seen in the Ti image that has a very light green colour, showing that there are pieces of the material on the surface.

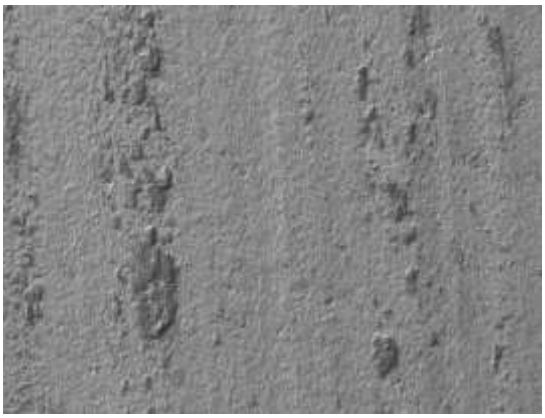

SEM Image

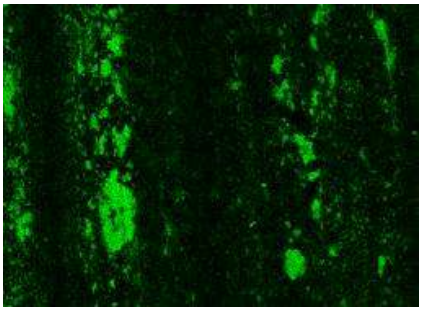

Ti

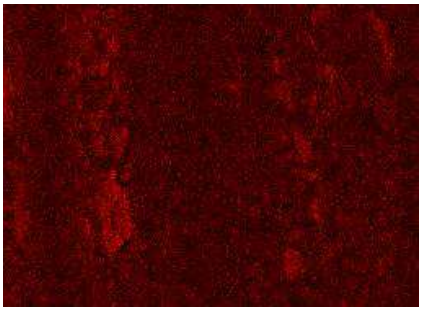

Al

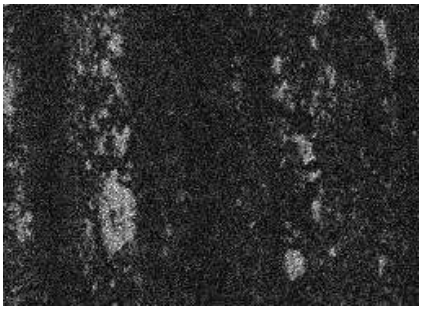

V

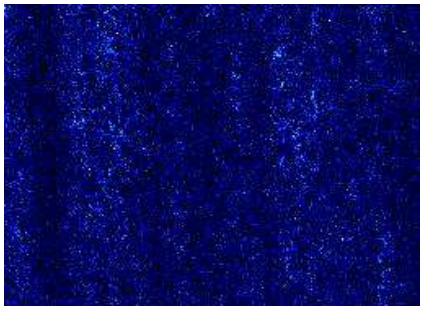

O

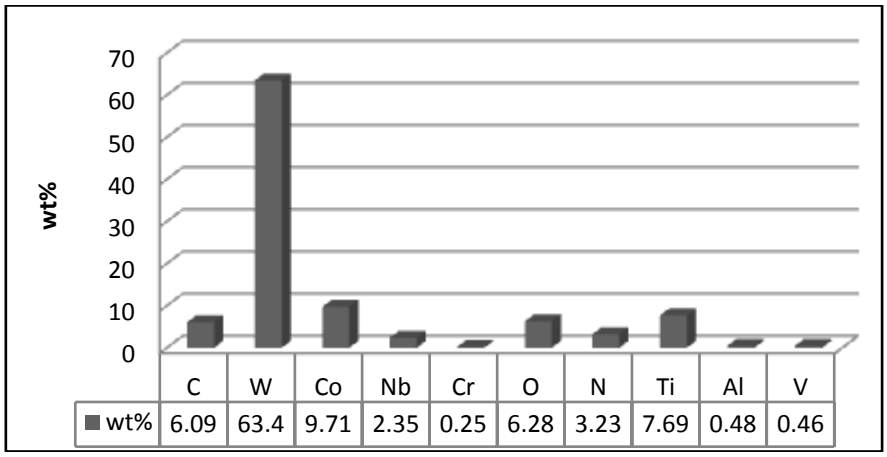

f)

Figure 4.33: SEM and EDS map of the contact between 10w%NbC/Ti6Al4V with a normal force of 50N

4.2.4 Summary of Results for Sliding Experiments

To compare the wear between the different couples with different normal forces, the wear volume loss of each contact couple is shown in Figure 4.34. In all three experiments with the CS carbide, the loss of material due to wear was the greatest. The two SPS carbides caused less wear, with the 10wt%NbC causing more wear on the Ti6Al4V pin between the two. As discussed in previous sections the Ti6Al4V in a self-mated contact couple had the least wear for all three normal forces.

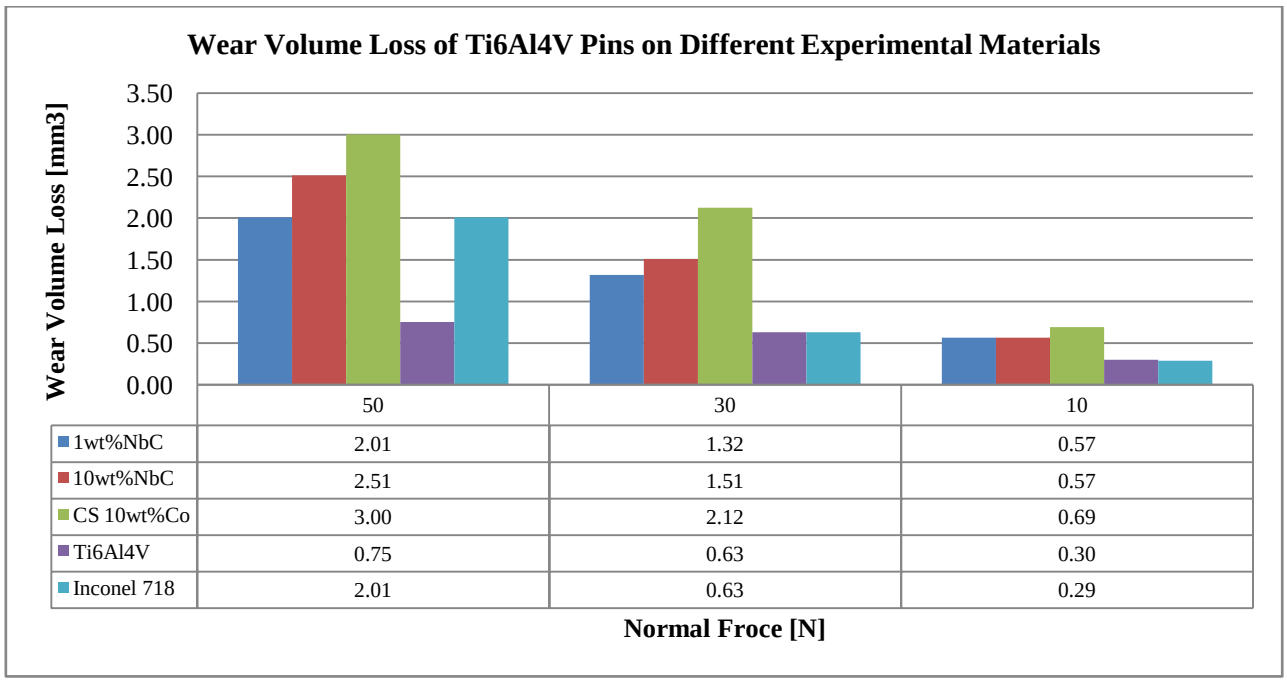

Figure 4.34: Wear volume loss [mm^3] for the different contact couples with varying normal force

The self-mated Ti6Al4V couples presented the least wear on the pins of all the materials, as well as lower and more stable friction coefficients for all three loads. An oxidative mechanism was present in the previously mentioned experiments, as large amounts of oxygen were found on the surface of the Ti6Al4V base material after EDS analysis. It was found that the wear of the Ti6Al4V pins increased when the normal force was increased. The friction coefficients increased slightly but became more stable overall with an increase in load. A correlation between friction and wear was noticed. The higher the friction the higher the wear on the Ti6Al4V pin. Of the cemented carbide materials the CS carbide created the most wear on the pins, followed by the 10wt%NbC and finally the 1wt%NbC. In the sliding experiment involving Ti6Al4V coupled with Inconel 718 the wear on the Ti6Al4V pin was less than those coupled with cemented carbides. It was noted that the wear of the pins was linearly proportional to the sliding distance. What was interesting about these results is that the 1wt%NbC carbide is harder than the 10wt%NbC carbide and should thus increase the wear on the pin. This was not the case, even with increasing load. The wear increase could be attributed to the smaller grains of the 10wt%NbC carbide. The smaller grains in this material were promoted through the use of a grain growth inhibitor namely chromium carbide. The CS carbide is the hardest of the three materials and caused the most wear. The transfer of Titanium was noticed in all the experiments and adhesion took place. Titanium was found to be on all the countersurfaces in substantial amounts.

The wear on the carbide surfaces was minimal and sign of wear on the surfaces were not apparent. On the other hand the Ti6Al4V pins wear was significant. The material was removed from the pins and this can be seen in all the microscope images of the pins. Galling and ploughing took place; this is interpreted from the images.

In conclusion, sliding wear of Ti6Al4V was found to depend on the hardness of the mating surface, loading conditions, as well as sliding distance. Ti6Al4V on Ti6Al4V was found to be the least damaging condition in sliding surfaces considered in this thesis.

5. Conclusion & Recommendations

5.1 Conclusion

The five objectives of the study were addressed in the document. A comprehensive literature review was presented on the topics of friction, sliding wear, the materials used in the thesis and how sliding contact affected the materials. From literature it was evident, that sliding wear has been addressed by various authors, using different materials and different contact configurations. However, all the conclusions and remarks were found to be case dependent.

The in house sliding apparatus was designed and commissioned in this study. The data was gathered using the apparatus regarding the coefficient of friction for specific material contact couples. This linear reciprocating sliding apparatus was found to be capable of providing basic information on two materials sliding against one another.

Spark plasma sintered carbides were compared to conventionally sintered carbide using mechanical and microstructural characterization. The SPS carbides showed good hardness and fracture toughness. The use of grain growth inhibitors in different proportions was effective and the results were encouraging, warranting further research into this form of cemented carbide manufacturing.

The results of the linear reciprocating sliding wear experiments on Ti6Al4V self-mated couples, Inconel 718 and various cemented carbides revealed that with an increase in normal force there was an increase in wear volume loss of the Ti6Al4V pin in all cases discussed. Friction coefficients for the Ti6Al4V/Ti6Al4V contact were found to be the most stable over the entire sliding distance, and also the lowest. Run-in periods were noted on many of the graphs. The friction coefficients of the cemented carbide couples were found to be the highest. Stable friction coefficients were produced when using a higher normal force.

Literature reviewed (Section 2.3.1), discussed the main wear mechanisms of Ti6Al4V when in sliding contact. Literature regarding wear mechanisms involved in sliding wear of Ti6Al4V describes the alloy as having low wear resistance and does not counteract adhesion, abrasion or delamination. The reasons for this are the low resistance to plastic shear and low work hardening, and the second is the low protection exerted by the surface oxide [***33***,***36***]. The experiments showed similar results. Ti6Al4V was prone wear phenomena such as adhesion, abrasion or delamination. SEM images showed small *droplets* of material on certain surfaces and in others large sections of material. Using EDS analysis it was found that these droplets and larger sections were pieces of the titanium alloy. As described in the literature, Ti6Al4V, readily transfers material to the counterface in dry sliding conditions. Wear debris was seen on the sliding surface. It is also possible that some of the debris remained in the contact zone and adhered to the countersurface. Oxygen was

detected on all the surfaces of the various base materials, and can lead to the conclusion that an oxide layer was formed on the surface.

5.2 Recommendations

The following recommendations were made for future investigations:

- Replacing the motor system used for linear motion with a linear actuator for better control over the linear reciprocating process.
- Using a trigger system for starting the data acquisition. This will provide more control over the data being gathered by the DAQ.
- The use of surface profilometry to quantify the wear volume loss of the base material (counterface material) caused by the sliding process.
- The use of SEM and EDS on the flat pin surface to provide better images of the worn pin surface. This will provide more information of the wear mechanisms involved.
- XRD of debris from the sliding process. This will provide further information on the oxide layer forming on the contact area when Ti6Al4V is involved in a sliding process.

References

[1] Williams JA. Engineering Tribology. New York: Oxford University Press Inc., 1994.

[2] Bhushan B. Priciples and Applications of Tribology.: John Wiley & Sons, Inc., 1999.

[3] Wang ZM, Ezugwu EO. Titanium Alloys and Their Machinability a Review. Journal of Materials Processing Technology 1997;68:262

[4] Moir I, Seabridge A. Aircraft Systems: Mechanical, electrical, and avionics subsystem integration, 3rd ed.: John Wiley & Sons, Ltd, 2008.

[5] PlaneCrashInfo.com [Online] [s.a] [access 15 August 2011]; Available: http://planecrashinfo.com/cause.htm

[6] Belobaba P, Odoni A, Barnhart C, editors., The Global Airline Industry. United Kingdom: John Wiley & Sons, Ltd, 2009.

[7] Battles B. Maintenance Costs: Significant but Tricky. [Online] 2003 [access 15 August 2011]; Available: http://www.aviationpros.com/article/10387195/maintenance-costs-significant-but-tricky

[8] Choudhury IA, El-Baradie MA. Machinabilty of nickel-base super alloys: A general review. Journal of Materials Processing technology. 1998;77: 278-284.

[9] Garg D, Dyer PN, Tungsten carbide erosion resistant coating for aerospace components. Materials Research Society: Fall Meeting, 1989.

[10] Pejryd L, Wigren J, Greving DJ, Shadley JR,Rybicki EF. Residual Stresses as a Factor in the Selection of Tungsten Carbide Coatings for a Jet Engine Application. Journal of Thermal Spray Technology 1995;4(3): 268-274.

[11] Agüero A, Camón F, García de Blas J, del Hoyo JC, Muelas R, Santaballa A, Ulargui S, Vallés P. HVOF-Deposited WCCoCr as Replacement for Hard Cr in Landing Gear Actuators. Journal of Thernal Spray Technology, October 2011.

[12] Cassar G, Avelar-Batista Wilson J C, Banfield S, Housden J, Matthews A, Leyland A. A study of the reciprocating-sliding wear performance of plasma treated titanium alloy. Wear 2010;269:60-70.

[13] Molinari A, Straffelini G, Tesi B, Bacci t. Dry Sliding Wear Mechanisms of the Ti6Al4V Alloy. Wear 1997;208:105-112.

[14] Straffelini G, Molinari A. Dry sliding wear of Ti-6Al-4V alloy as influenced by the counterface and sliding conditions. Wear 1999; 236: 328-338.

[15] Bonny K, De Baets P, Perez Y, Vleugels J, Lauwers B. Friction and wear characteristics of WC–Co cemented carbides in dry reciprocating sliding contact. Wear 2010.

[16] Quercia G, Grigorescu I, Contreras H, Di Rauso C, Gutiérrez-Campos D. Friction and wear behavior of several hard materials. International Journal of Refactory Metals and Hard Materials 2001; 19:359-369.

[17] Pirso J, Letunovitš S, Viljus M. Friction and wear behavior of cemented carbides. Wear 2004;257:257-265.

[18] Engqvist H, Högberg H, Botton GA, Ederyd S, Axén N. Tribofilm formation on cemented carbides in dry sliding conformal contact. Wear 2000; 239:219-228.

[19] Komanduri R, Shaw MC. Galling wear of materials at high speed sliding contact. Wear 1975;33:283-292.

[20] Gale WF,Totemeier TC, editors. Smithells Metals Reference Book, 8th ed.: Elsevier Butterwirth-Heinemann, 2004.

[21] Hutchings IM. Tribology: Friction and Wear of Engineering Materials'. London: Edward Arnold, 1992.

[22] Meriam JL, Kraige, LG. Engineering Mechanics: Statics, 5th ed. United States of America, vol 1: John Wiley & Sons, Inc, 2003.

[23] Axén N, Jacobson S, Hognmark S. Influence of hardness of the ounterbody in three-body abrasive wear - an overlooked hardness effect. Tribology International 1994; 27(4): 233-241.

[24] Groover MP. Fundamentals of Modern Manufacturing- Materials, Processes, and Systems, 3rd ed. United States of America: John Wiely & Sons, Inc, 2007.

[25] Callister WD. Material Science and Engineering - An Introduction, 6th ed. United States of America: John Wiley & Sons, Inc, 2003.

[26] Gurrappa I. Characterization of titanium alloy Ti6Al4V for chemical, marine and industrial applications. Materials Characterization 2003;51:131-139.

[27] Rack HJ, Qazi JI. Titanium alloys for biomedical applications. Material Characterization C 2006; 26:1269-1277.

[28] Jaffery SI, Mativenga PT. Assessment of the machinability of Ti-6Al-4V alloy using the wear map approach. International Journal of Advanced Manufufacturing Technology 2009; 40:687-696.

[29] Hughes JI, Sharman AR, Ridgway K. The effect of cutting tool material and edge geometry on tool life and workpiece surface integrity. Proceedings of the Institution od Mechanical Engineers Part B – Journal of Engineering Manufacture 2006;220(B): 93–107.

[30] Su Y, He N, Li L, Li XL. An experimental investigation of effects of cooling/lubrication conditions on tool wear in high-speed end milling of Ti-6Al-4V. Wear 2006; 261: 760-766.

[31] Barnett-Ritchey DD. High-Speed Milling of Titanium and γ-Titanium Aluminide: An Experimental Investigation. [PhD]. McMaster University, 2004.

[32] Arrazola PJ, Garay A, Iriarte LM, Armendia M, Marya S, Le Maître F. Machinability of Titanium Alloys (Ti6Al4V and Ti555.3). Journal of Materials Processing Technology 2009;209:2223–2230.

[33] Qu J, Blau PJ, Watkins TR, Cavin OB,Kulkarni NS. Frction and wear of titanium alloys sliding against metal, polymer, and ceramic counterfaces. Wear 2005;258:1348-1356.

[34] Long M, Rack HJ. Friction and surface behaviour of selected titanium alloys during reciprocating-sliding motion. Wear 2001;249:158-168.

[35] Dong H, Bell T. Tribological behaviour of alumina sliding against Ti6Al4V in unlubricated contact. Wear 1999;225:874-884.

[36] Alman DE, Hawk JA. The abrasive wear od sintered titanium matrix-cermaic particle reinforced composites. Wear 1999;225-229:629-639.

[37] Nazarenko PV, Polishchuk IE, Malyar AG, Ostranitsa AE. Tribotechnical properties of coatings on titanium alloys. Materials Science 1998;34(2):203-210.

[38] International Tungsten Industry Association. [Online] [s.a] [access 20 March 2010]; Available: http://www.itia.info/Default.asp?Page=53

[39] Kurlov AS, Gusev AI. Tungsten Carbides and W–C Phase Diagram. Inorganic Materials 2006;42(2):121-127.

[40] Koc R, Kodambaka SK. Tungsten carbide (WC) synthesis from novel precursors. Journal of the European Ceramic Society 2000;20:1859-1869.

[41] Ågren J, Petersson A. Modelling Wc-Co sintering shrinkage- Effect of carbide grain size and cobalt content. Material Science and Engineering A 2007:452-453:37-45.

[42] Weidow J, Zackrisson J, Jansson B, Andren HO. Characterisation of WC-Co with cubic carbide additions. International Journal of Refactory Metals & Hard Metals 2009;27:244-248.

[43] Hashe NG, Norgren SM, Andren HO, Neethling JH. Characterization of WC-(W, V)C-Co made from pre-alloyed (W, V)C. International Journal of Refactory Metals & Hard Metals 2009;27:229-233.

[44] Lassner E, Schubert wd. Tungsten: Properties, Chemistry, Technology of the Element, Alloys, and Chemical Compounds. New York: Kluwer Academic/Plenum Publishers, 1998.

[45] Mravic B, Mahulikar D, Violette GN, Shapiro H, Halverson HJ. Patent: Lead-free Bullet. 1995:5,399,187.

[46] Prakash LJ. Application of Fine Grained Tungsten Carbide Based Cemented Carbides. International Journal of Refactory Metals and Hardmaterials 1995;13:257-264.

[47] Mamedov V. Spark plasma sintering as advanced PM sintering method. Powder Metallurgy 2002;45(4):322-327.

[48] Zhao S, Song X, Wei C, Zhang L, Liu X, Zhang J. Effects of WC particle size on densification and properties of spark plasma sintered WC–Co cermet. International Journal of Refractory Metals & Hard Materials 2009;27:1014-1018.

[49] Beste U. On the nature of cemented carbide wear in rock drilling. [PhD]. Uppsala University, 2004.

[50] Makgere MF. The Effect of Thermal Shock on the Abrasive Wear of WC-12wt%Co. [Masters Thesis]. Univeristy of the Witwatersrand, 2007.

[51] Ezugwu EO, Okeke CI, Machado AR. High speed threading of inclusion-modified steels with coated carbide tools. Journal of Materials Processing Technology 1999;86:216-225.

[52] Ezugwu EO, Bonney J, Yamane Y. An overview of the machinability of aeroengine alloys. Journal of Materials Processing Technology 2003;134:233-253.

[53] Ezugwu EO. Improvements in the machining of aero-enginealloys using self-propelled rotary tooling technique. Journal of Materials Processing Technology 2007;185:60-71.

[54] Donachie MJ, Donachie SJ. Superalloys. A Technical Guide, 2nd ed.: ASM International, 2002.

[55] Metals Handbook, 10th ed. USA: ASM International, vol. 1, 1990.

[56] Rahman M, Seah WKH, Teo TT. The machinability of Inconel 718. Journal of Materials Processing Technology 1997;63:199-204.

[57] Alauddin M, Mazid MA, El Baradi MA, Hashmi MSJ. Cutting forces in the end milling of Inconel 718. Journal of Materials Processing Technology 1998;77:153-159.

[58] Kitigawa T, Kubo A, Maekawa K. Temperature and wear of cutting tools in high-speed machining of Inconel 718 and Ti-6Al-6V-2Sn. Wear 1997;202:142-148.

[59] Alauddin M, El Baradie MA, Hashmi MSJ. Optimization of surface finish in end milling Inconel 718. Journal of Materials Processing Technology 1996;56:54-65.

[60] Guo Z, Xiong J, Yang M, Song X, Jiang C. Effect of Mo2C on the microstructure and properties of WC–TiC–Ni cemented carbide. International Journal of Refractory Metals & Hard Materials 2008;26:601-605.

[61] Almond EA, Roebuck B. Identification of optimum binder phase compositions for improved WC hard metals. Materials Science and Engineering A 1988;105/106(A):237-248.

[62] Guo Z, Xiong J, Yang M, Jiang C. WC–TiC–Ni cemented carbide with enhanced properties. Journal of Alloys and Compounds 2008;465:157-162.

[63] Haung SG, Li L, Van der Biest O, Vleugels J. Influence of WC addition on the microstructure and mechanical properties of NbC-Co cermets. Journal of Alloys and Compounds 2007;430:158-164.

[64] Haung SG, Liu RL, Li L, Van der Biest O, Vleugels J. NbC as grain growth inhibitor and carbide in WC-Co hardmetals. International Journal of Refactory and Hard Materials 2008;26:289-295.

[65] Sun L, Jia C, Cao R, Lin .Effects of Cr3C2 additions on the densification, grain growth and properties of ultrafine WC-11Co composites by spark plasma sintering. International Journal of Refractory Metals and Hard Materials 2008;26:357-361.

[66] Tsuchida T, Kakuta T. Fabrication of SPS compacts from NbC-Nb2 powder mixtures synthesized by the MA-SHS in air process. Journal of Alloys and Compounds 2006; 415:156 - 161.

[67] Wittmann B,Schubert WD, Lux B. WC grain growth and grain growth inhibition in nickel and iron binder hardmetals. International Journal of Refractory Metals and Hard Materials 2002;20:(1):51-60.

[68] Groover MP. Fundamentals of Modern Manufacturing: Materials, Processes and Systems, 2nd ed.: John Wiley & Sons, Inc, 2002.

[69] Shetty DK, Wright IG, Mincer PN, Clauer AH. Indentation fracture of WC-CO cermets. Journal of Material Science 1985;20:1873-1882.

[70] ASM Handbook Committee, ASM Handbook, 9th ed. United States of America, vol. VII, 1992.

[71] Roebuck B. Magnetic Moment (Saturation) Measurements on Hardmetals. International Journal of Refractory Metals & Hard Materials 1996;14:419-424.

[72] ASM Handbook Committee, ASM Handbook, 9th ed. United States of America, vol X 1992.

References

[73] Oosthuizen E. Investigating Titanium Wear Characteristics; Phase 1: Construction of a Test Jig and Establishment of a Basic Test Method. [Unpublished Final Year Project]. Department of Industrial Engineering, University of Stellenbosch, 2009.

[74] Bonfigilioli. Bonfigilioli: VF-W series. [Online] [s.a] [access 23 March 2010]; Available: http://bonfiglioliproduct.pleiadi.it//static/public/attachments/br_cat_vf-w_1847_r9.pdf

[75] Bonfigilioli. Bonfigilioli: Vectron. [Online] [s.a] [access 23 March 2010]; Available: http://www.vectron.net/pdf/syn/vec171/cat_syn_uk.pdf

[76] HBM. HBM: QuantumX MX410. [Online] [s.a] [access 23 March 2010]; Available: http://www.hbm.com/fileadmin/mediapool/hbmdoc/technical/b2612.pdf

[77] HBM. HBM: SP4C3/SP4C3-MR. [Online] [s.a] [access 23 March 2010]; Available: http://www.hbm.com/en/menu/produkte/waegetechnik/plattform-waegezellen/single/categorie/weighing-single-point-load-cells/product/sp4c3sp4c3-mr/backPID/single-point-load-cells/

[78] Struers. Struers: Metallographic preperation of titanium. [Online]. [s.a] [access 15 May 2011]; Available: http://www.struers.com/default.asp?top_id=5&main_id=24&sub_id=185&doc_id=855

[79] Bonny K, De Baets P, Vleugels J, Huang S, Vande O. Impact of Cr3C2/VC addition on the dry sliding friction and wear response of WC–Co cemented carbides. Wear 2009;267:1642-1652.

[80] ASM. ASM Aerospace Specification Metals Inc. [Online]. [s.a] [access 15 May 2011]; Available: http://asm.matweb.com/search/SpecificMaterial.asp?bassnum=MA7075T6

Appendix A

A.1 Ti6Al4V Self-mated Contact Couple

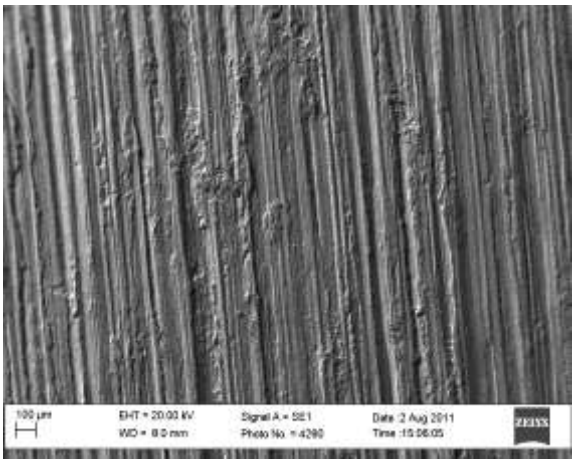

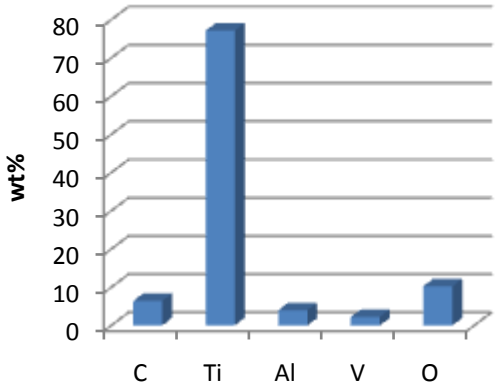

a)

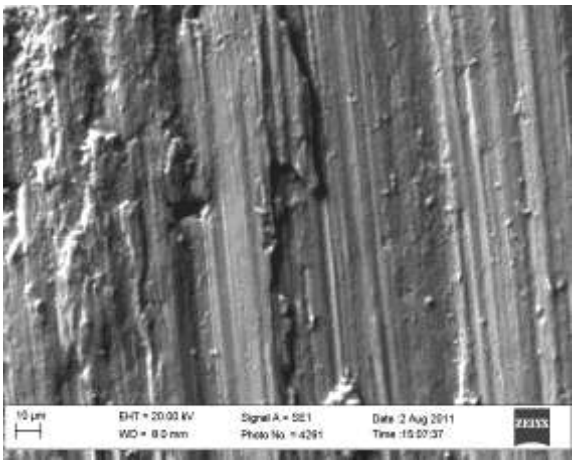

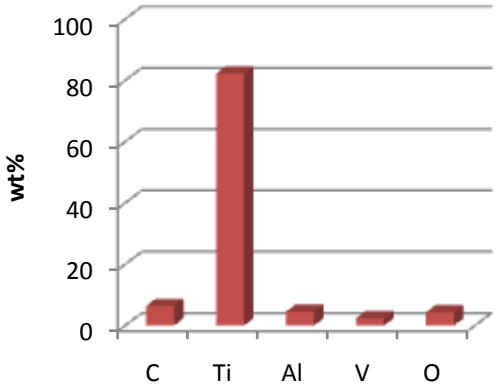

b)

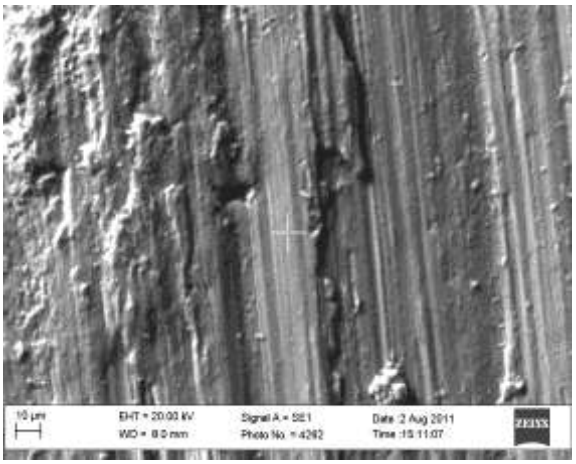

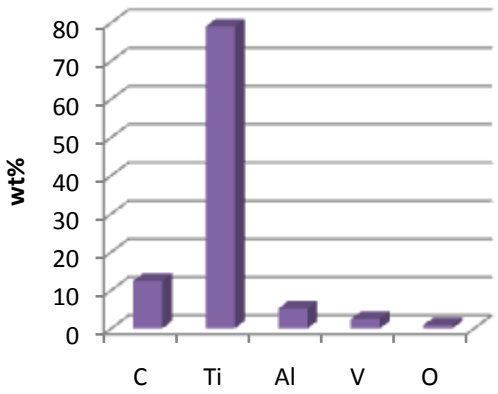

c)

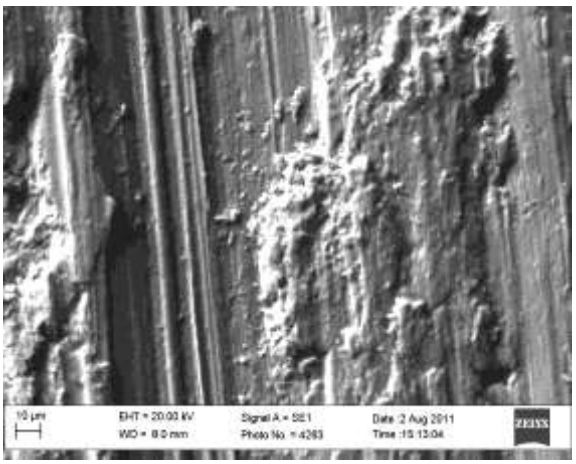

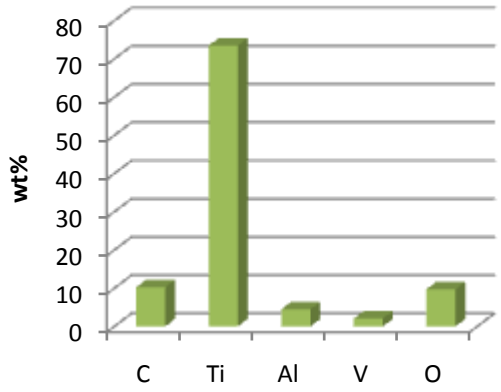

d)

Figure A.1: SEM images of Ti6Al4V/Ti6Al4V contact couple with an applied normal force of 50N; a) 40X area analysis, b) 500X area analysis, c) 500X spot analysis of surface, d) 500X spot analysis of surface formations

Table A.1: Quantitative results for Ti6Al4V/Ti6Al4V contact couple (Figure A.1)

	Element [wt%]				
Figure A.1	C	Ti	Al	V	O
a)	6.38	77.12	3.98	2.24	10.28
b)	6.44	82.27	4.54	2.42	4.33
c)	12.41	79.02	5.22	2.45	0.9
d)	10.24	73.47	4.48	2.07	9.74

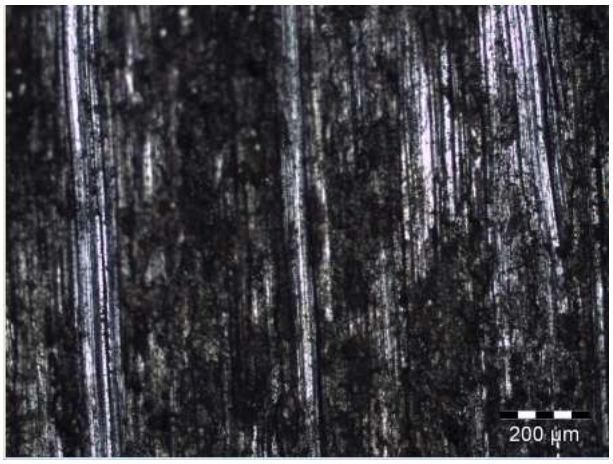

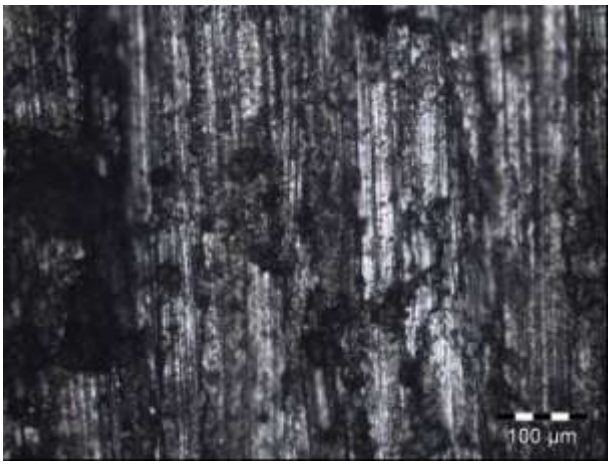

a) b)

Figure A.2: Microscope images of the Ti6Al4V pin couple on Ti6Al4V with a normal force of 50N; a) 100X MAG, b) 200X MAG

Appendix A

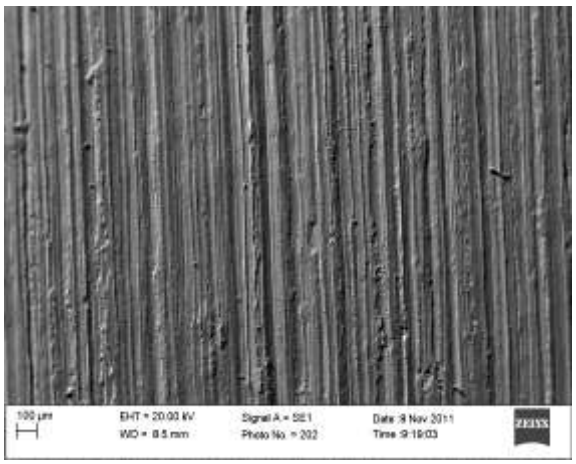

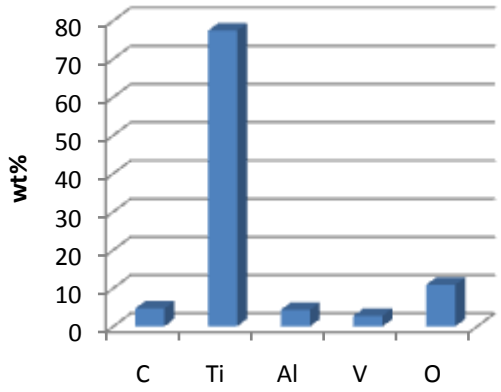

a)

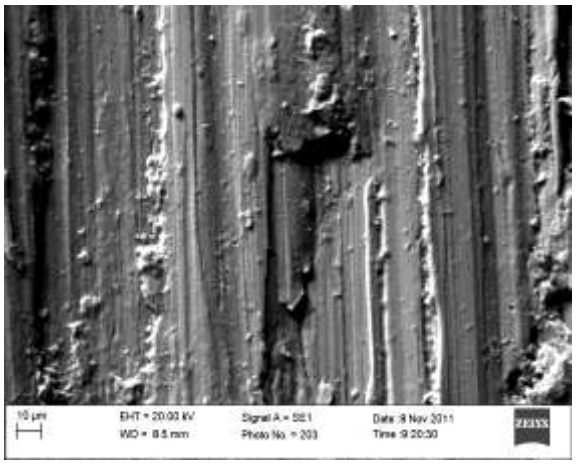

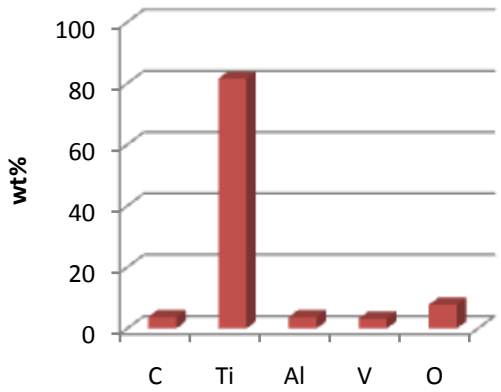

b)

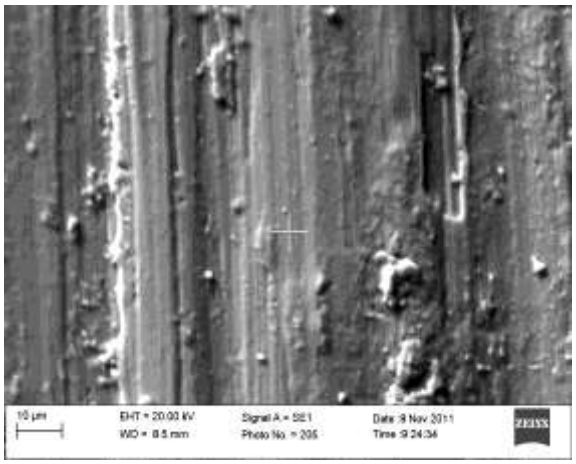

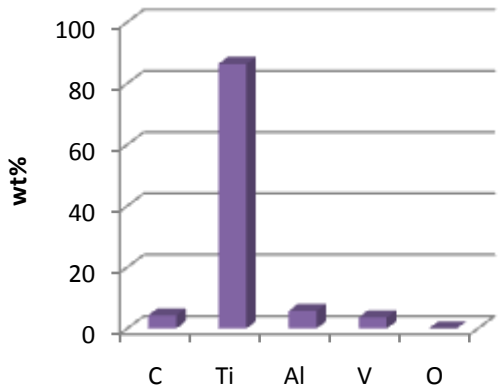

c)

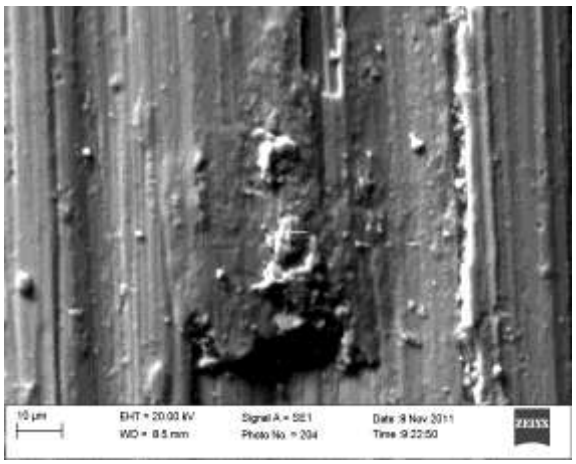

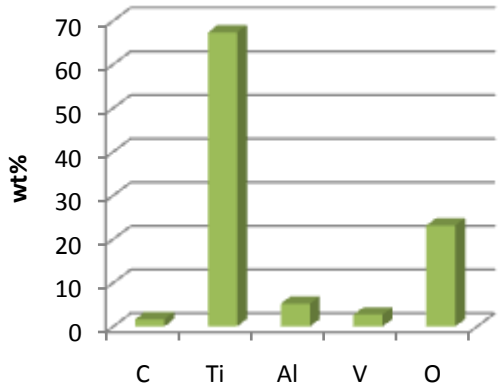

d)

Figure A.3: SEM images of Ti6Al4V/Ti6Al4V contact couple with an applied normal force of 30N; a) 40X area analysis, b) 500X area analysis, c) 500X spot analysis of surface, d) 500X spot analysis of surface formations

Table A.2: Quantitative results for Ti6Al4V/Ti6Al4V contact couple (Figure A.3)

	Element [wt%]				
Figure A.3	**C**	**Ti**	**Al**	**V**	**O**
a)	4.67	77.35	4.30	2.78	10.90
b)	3.74	81.57	3.71	3.21	7.77
c)	4.30	86.35	5.72	3.62	0.00
d)	1.65	67.32	5.20	2.70	23.12

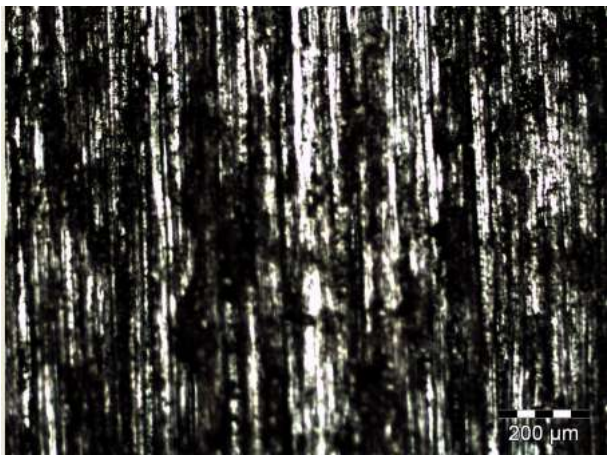

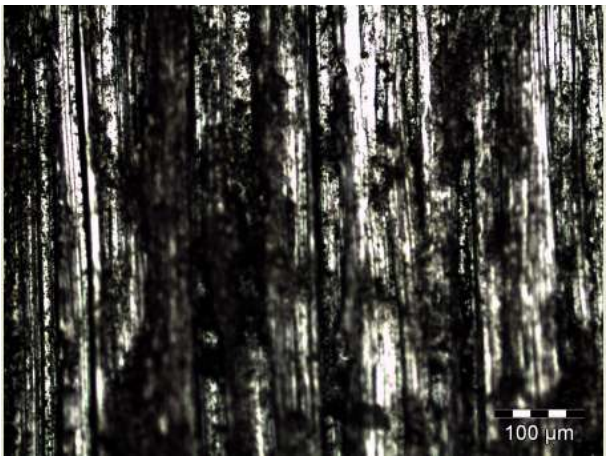

a) b)

Figure A.4: Microscope images of the Ti6Al4V pin couple on Ti6Al4V with a normal force of 30N; a) 100X MAG, b) 200X MAG

A.2 Ti6Al4V/Cemented Carbide Contact Couples

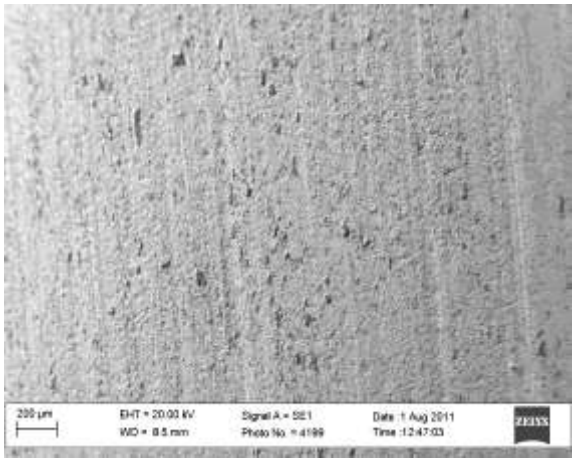

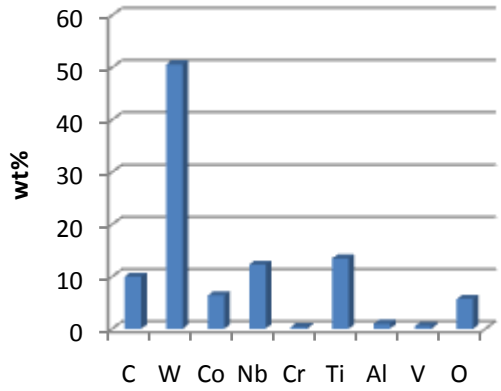

a)

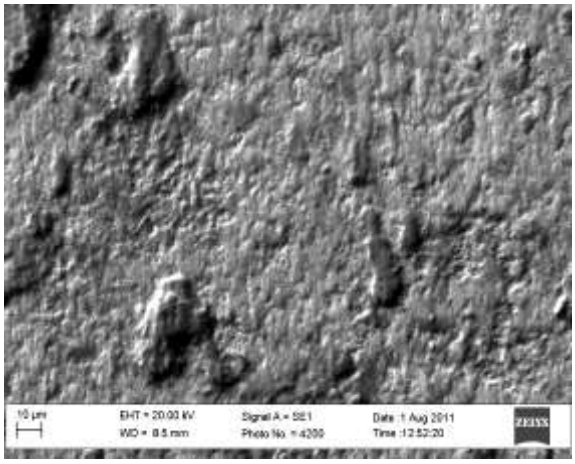

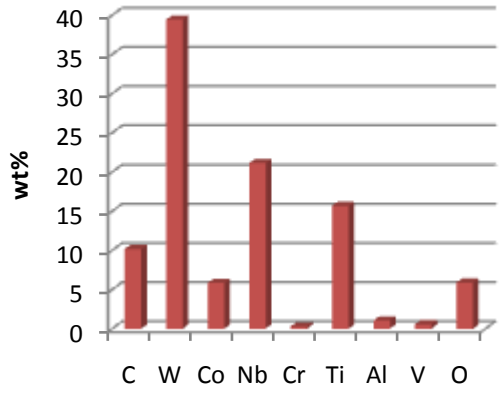

b)

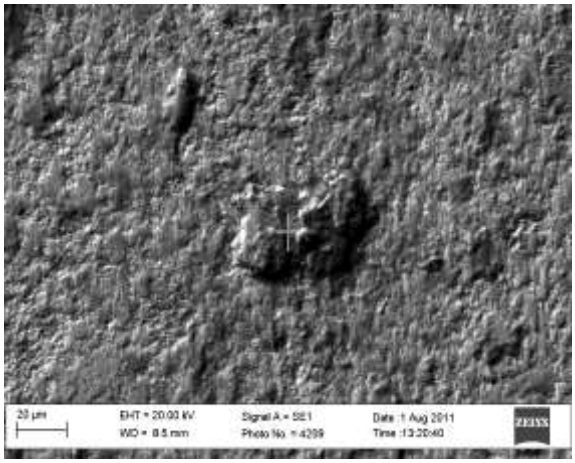

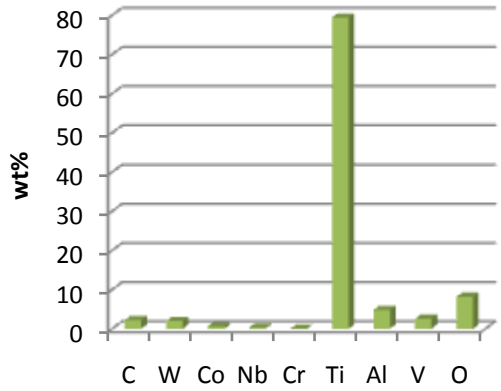

c)

Figure A.5: SEM images of 1wt%NbC/Ti6Al4V contact couple with an applied normal force of 50N; a) 40X area analysis, b) 500X area analysis, c) 500X spot analysis of surface formations

Table A.3: Quantitative results for 1wt%NbC/Ti6Al4V contact couple (Figure A.4)

	Element [wt%]								
Figure A.4	**C**	**W**	**Co**	**Nb**	**Cr**	**Ti**	**Al**	**V**	**O**
a)	9.94	50.56	6.39	12.23	0.33	13.44	0.92	0.51	5.68
b)	10.17	39.43	5.84	21.12	0.29	15.66	1.04	0.56	5.89
c)	2.22	1.96	0.58	0.31	0.05	79.38	4.81	2.53	8.16

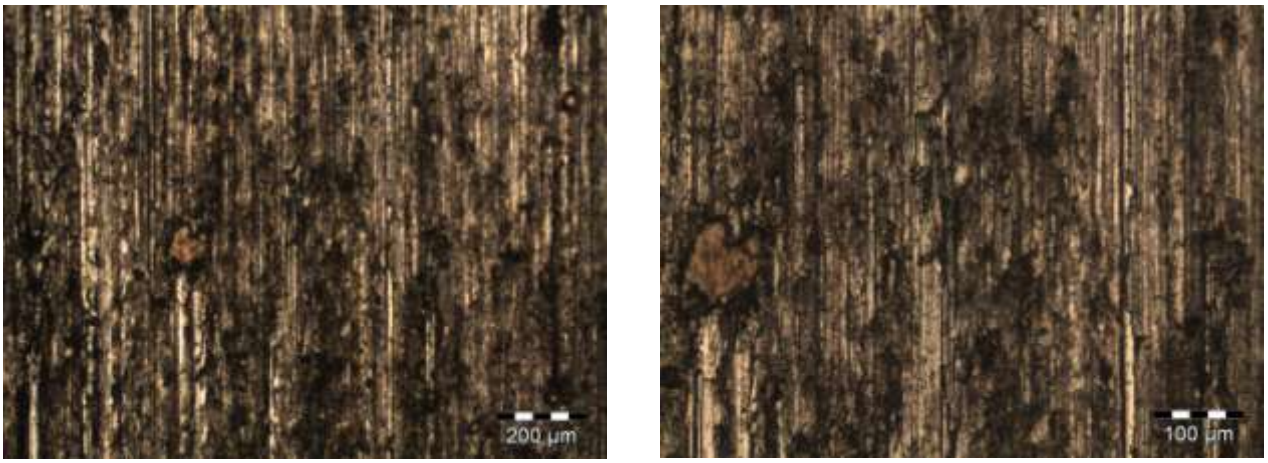

a) 100X b) 200X

Figure A.6: Microscope images of the Ti6Al4V pin couple with 1wt%NbC with a normal force of 50N; a) 100X MAG, b) 200X MAG

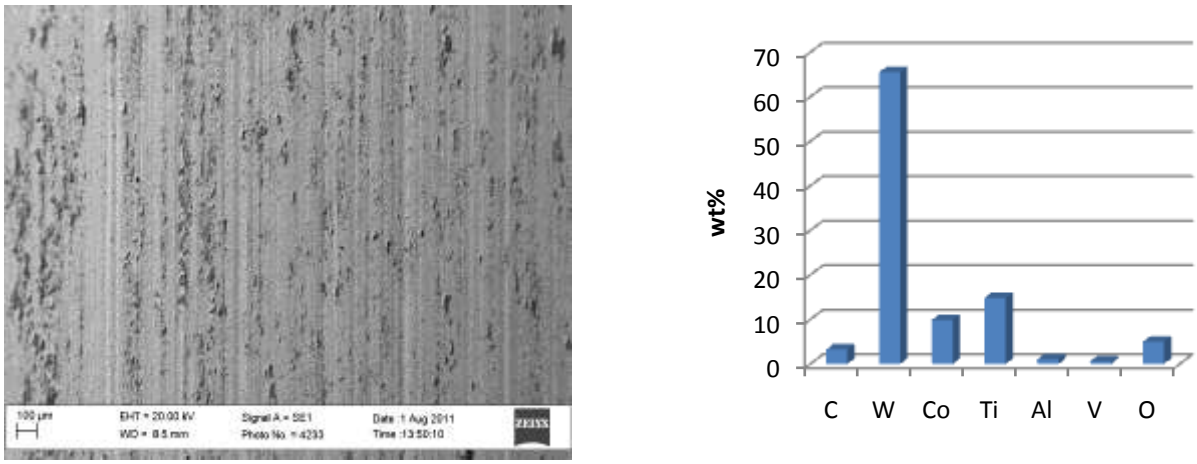

a)

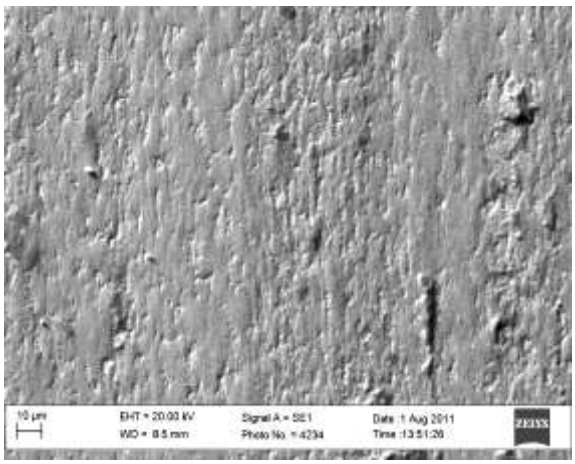

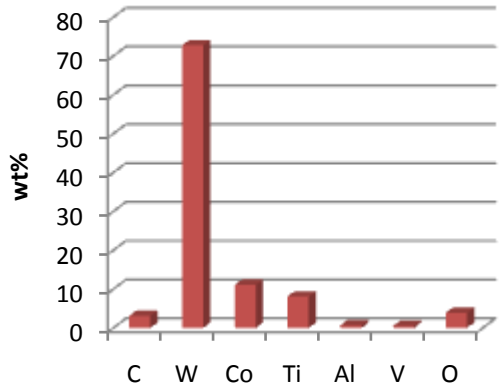

b)

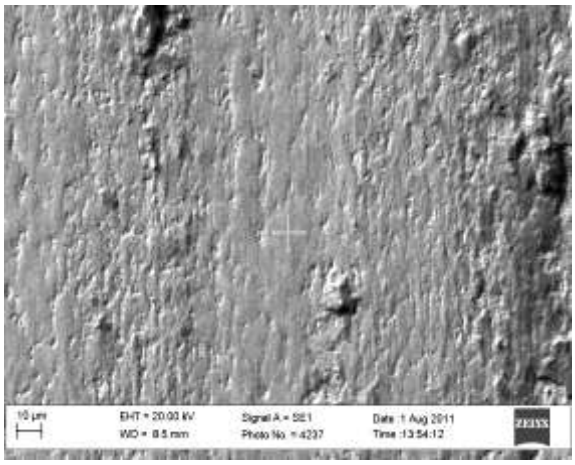

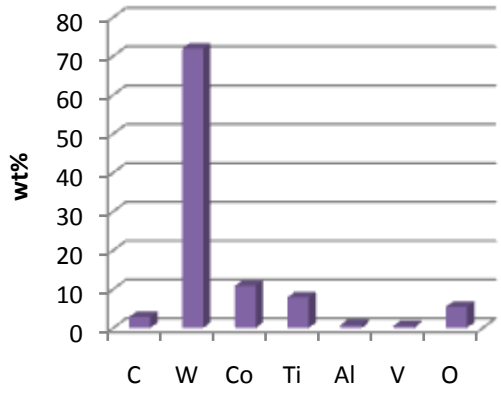

c)

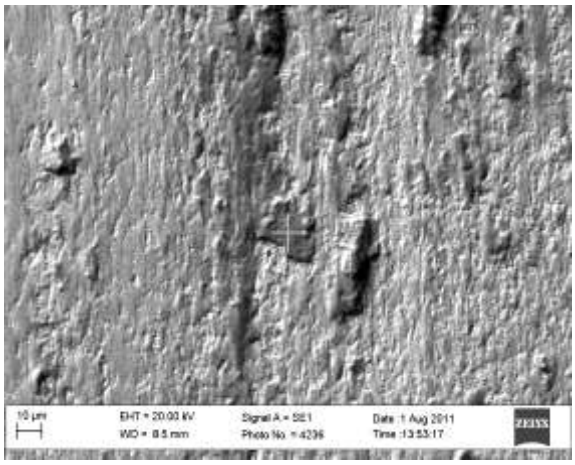

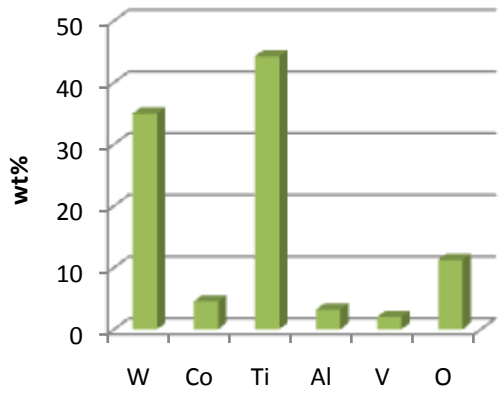

d)

Figure A.7: SEM images of CS/Ti6Al4V contact couple with an applied normal force of 50N; a) 40X area analysis, b) 500X area analysis, c) 500X spot analysis of surface, d) 500X spot analysis of surface formations

Table A.4: Quantitative results for CS/Ti6Al4V contact couple (Figure A.5)

	Element [wt%]						
Figure A.5	**C**	**W**	**Co**	**Ti**	**Al**	**V**	**O**
a)	3.24	65.49	9.87	14.82	1.03	0.56	5.00
b)	3.10	72.75	11.05	8.06	0.64	0.50	3.89
c)	2.81	71.86	10.82	7.89	0.75	0.47	5.40
d)	0.26	4.09	1.29	75.91	3.13	3.04	12.28

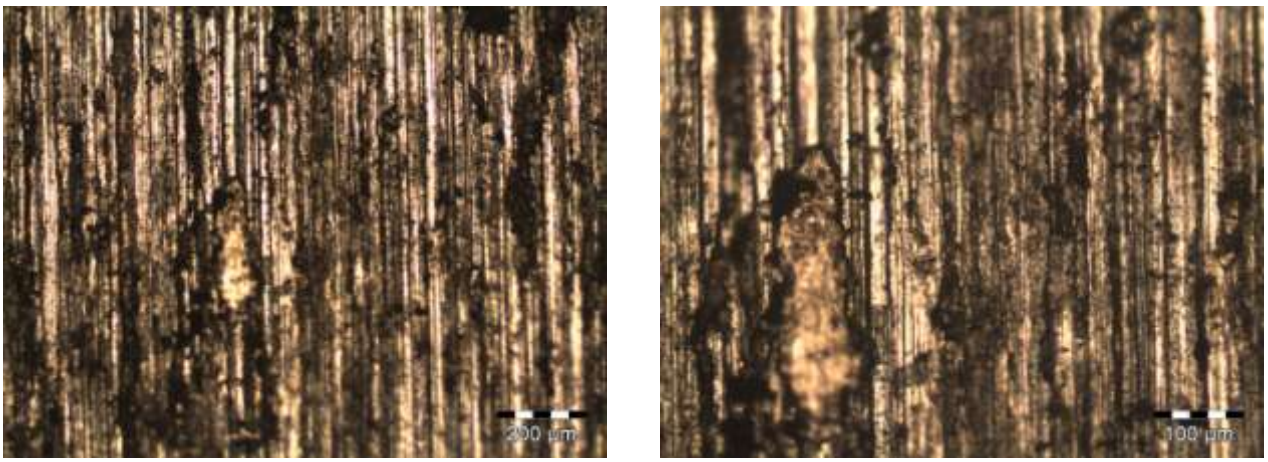

a) 100X b) 200X

Figure A.8: Microscope images of the Ti6Al4V pin couple with CS with a normal force of 50N; a) 100X MAG, b) 200X MAG

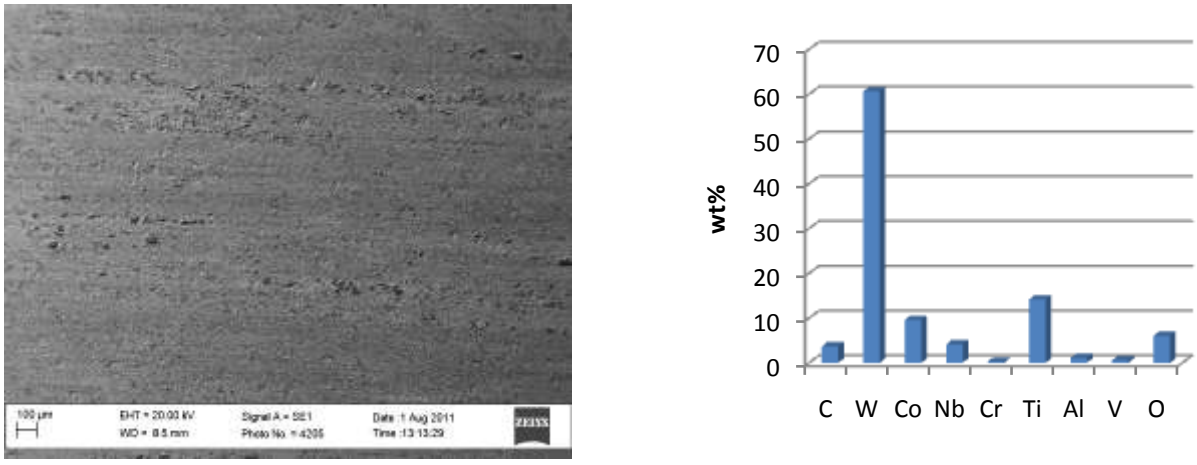

a)

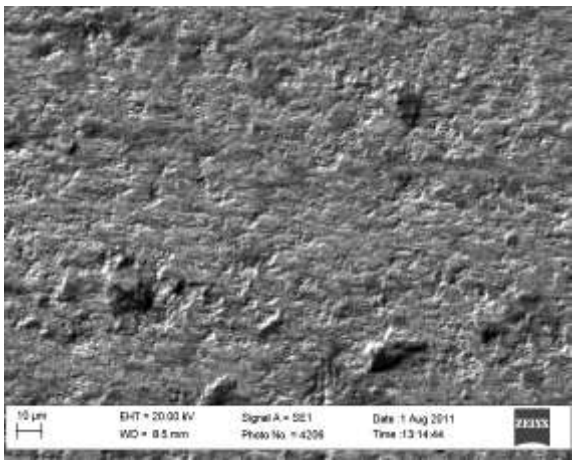

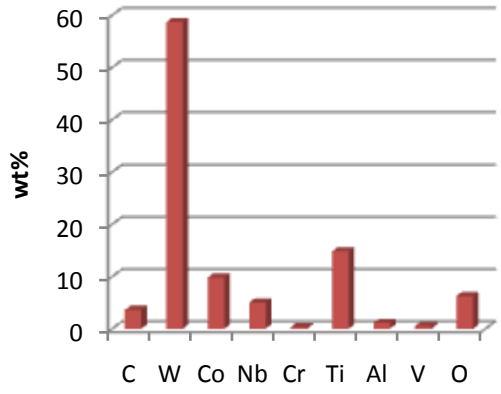

b)

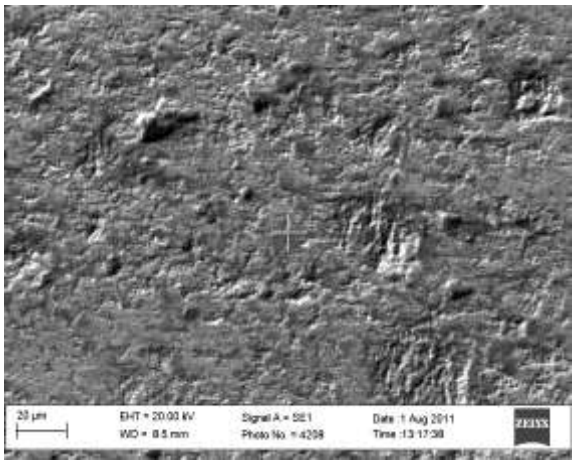

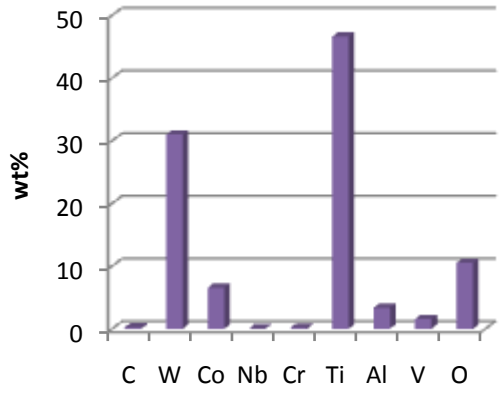

c)

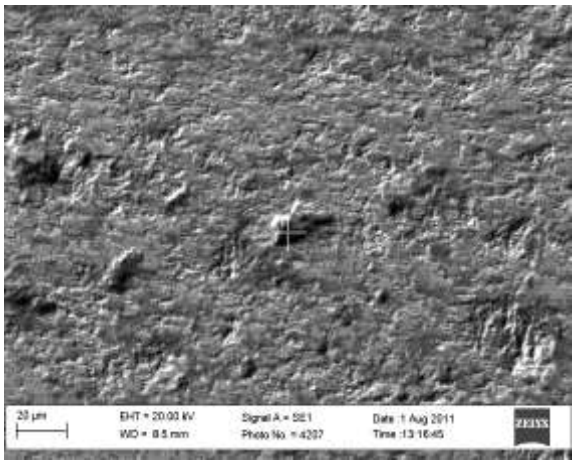

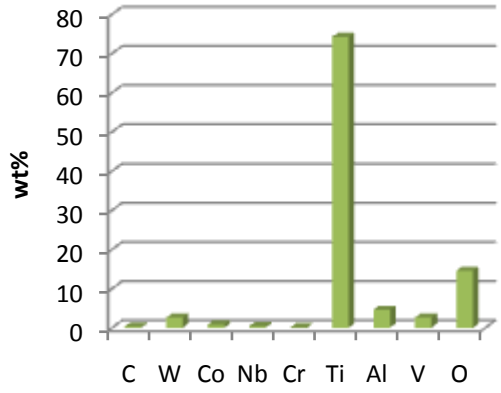

d)

Figure A.9: SEM images of 10wt%NbC/Ti6Al4V contact couple with an applied normal force of 30N; a) 40X area analysis, b) 500X area analysis, c) 500X spot analysis of surface, d) 500X spot analysis of surface formations

Table A.5: Quantitative results for 10wt%NbC/Ti6Al4V contact couple (Figure A.6)

	Element [wt%]								
Figure A.6	**C**	**W**	**Co**	**Nb**	**Cr**	**Ti**	**Al**	**V**	**O**
a)	3.66	60.58	9.57	4.12	0.26	14.13	1.10	0.57	6.01
b)	3.61	58.68	9.78	4.99	0.33	14.81	1.08	0.51	6.23
c)	0.23	30.99	6.53	0.05	0.19	46.60	3.36	1.55	10.50
d)	0.29	2.59	0.77	0.38	0.13	74.18	4.55	2.60	14.52

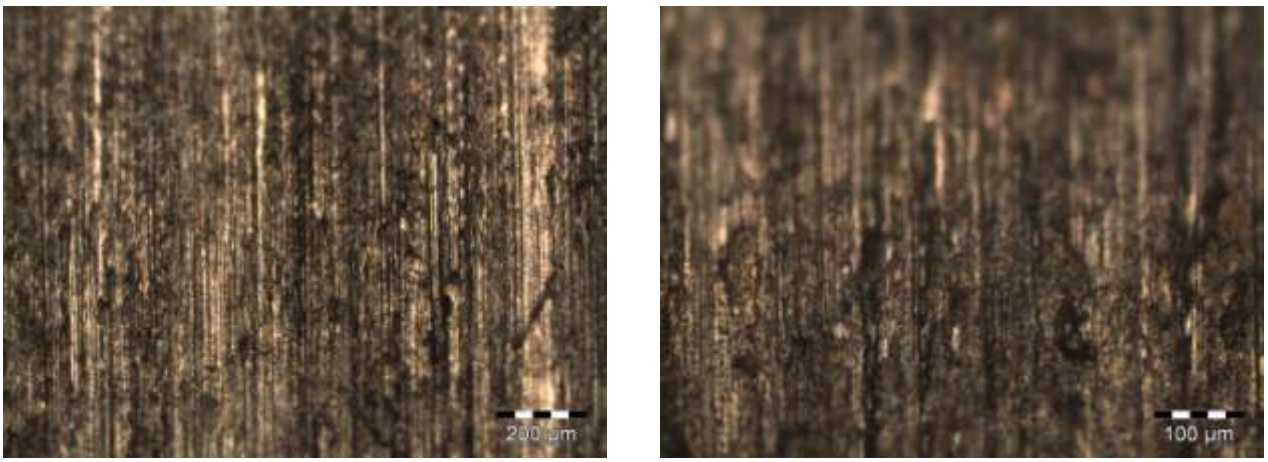

a) 100X b) 200X

Figure A.10: Microscope images of the Ti6Al4V pin couple with 10wt%NbC with a normal force of 30N; a) 100X MAG, b) 200X MAG

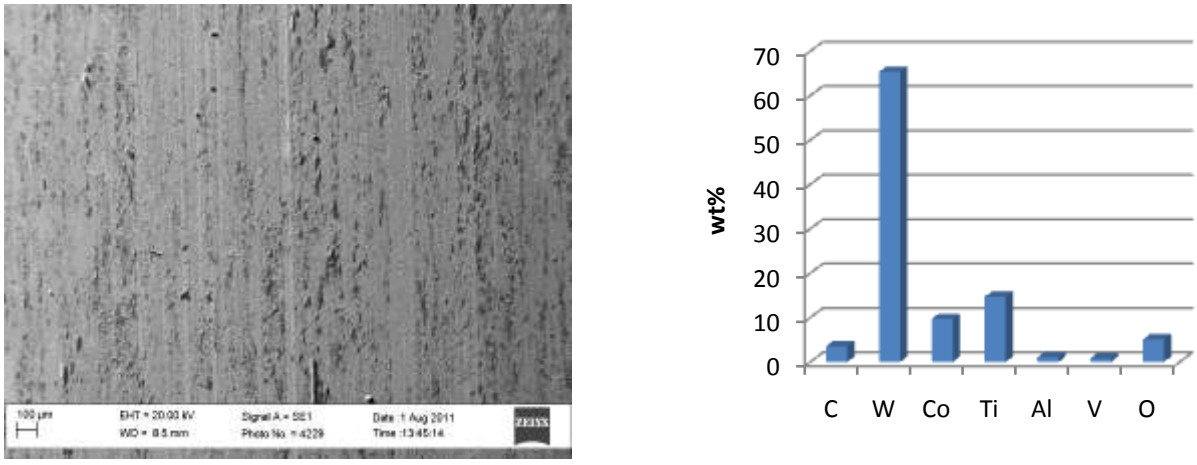

a)

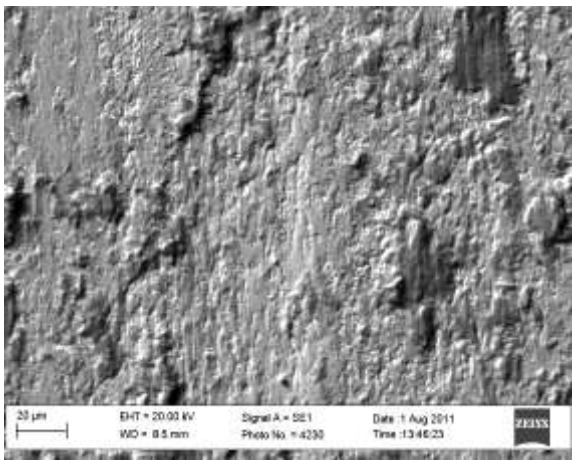

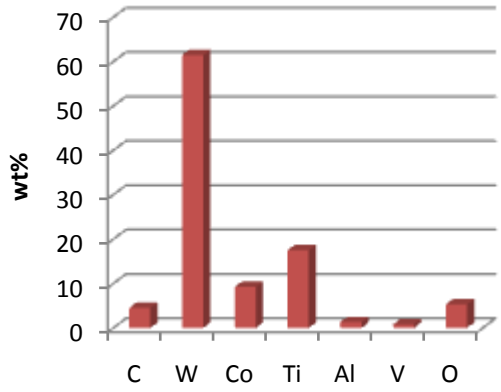

b)

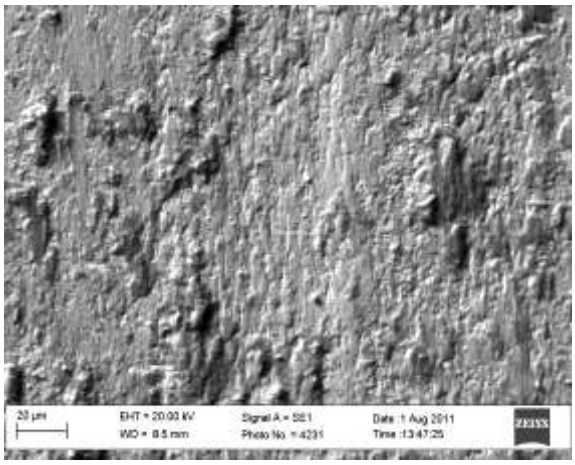

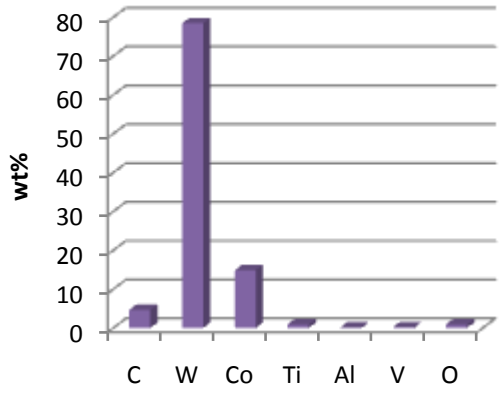

c)

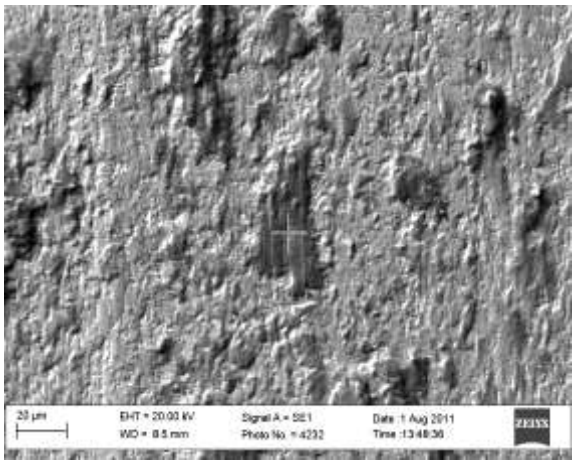

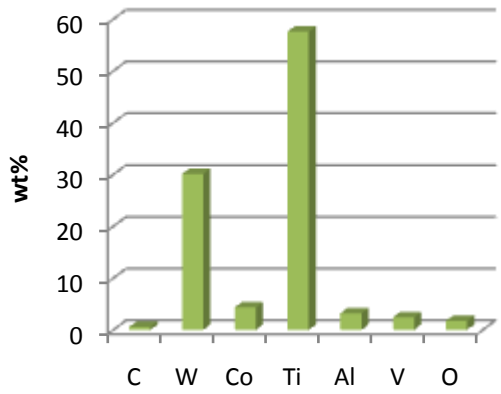

d)

Figure A.11: SEM images of CS/Ti6Al4V contact couple with an applied normal force of 30N; a) 40X area analysis, b) 500X area analysis, c) 500X spot analysis of surface, d) 500X spot analysis of surface formations

Table A.6: Quantitative results for CS/Ti6Al4V contact couple (Figure A.11)

	Element [wt%]						
Figure A.11	**C**	**W**	**Co**	**Ti**	**Al**	**V**	**O**
a)	3.55	65.35	9.66	14.64	0.99	0.76	5.04
b)	4.48	61.43	9.24	17.47	1.29	0.79	5.30
c)	4.66	78.43	14.82	0.90	0.11	0.20	0.88
d)	0.57	30.13	4.33	57.58	3.19	2.45	1.74

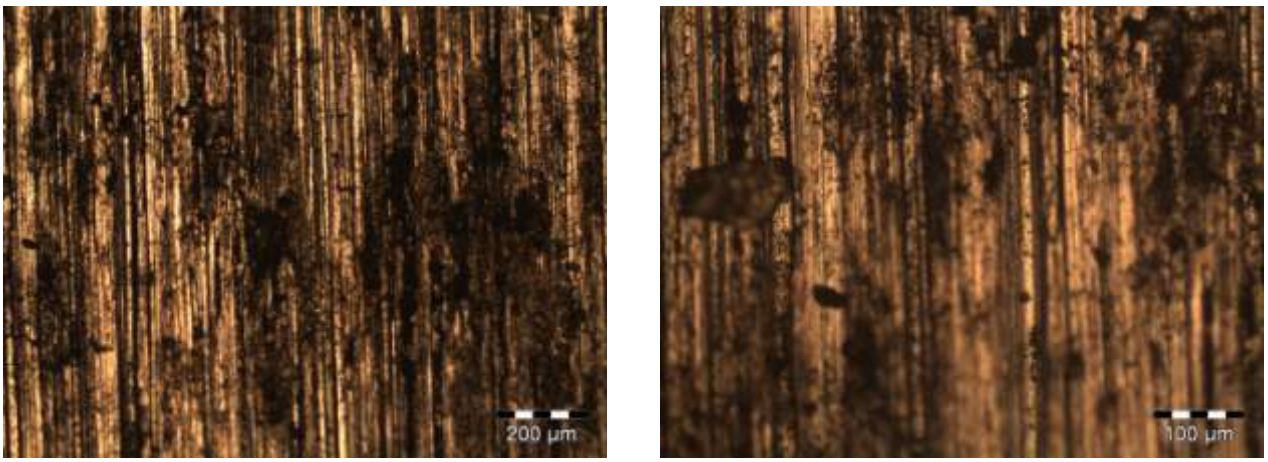

a) 100X b) 200X

Figure A.12: Microscope images of the Ti6Al4V pin couple with CS with a normal force of 30N; a) 100X MAG, b) 200X MAG

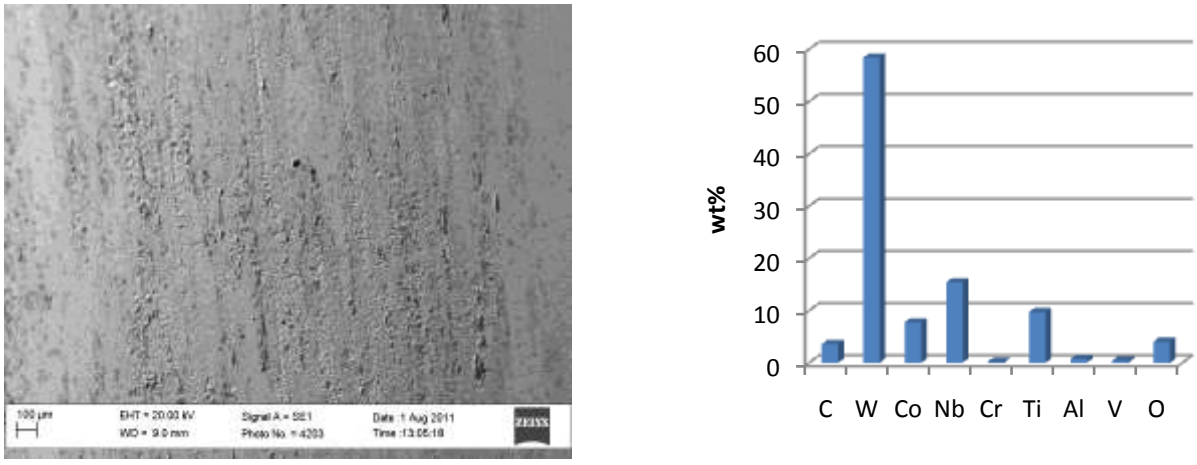

a)

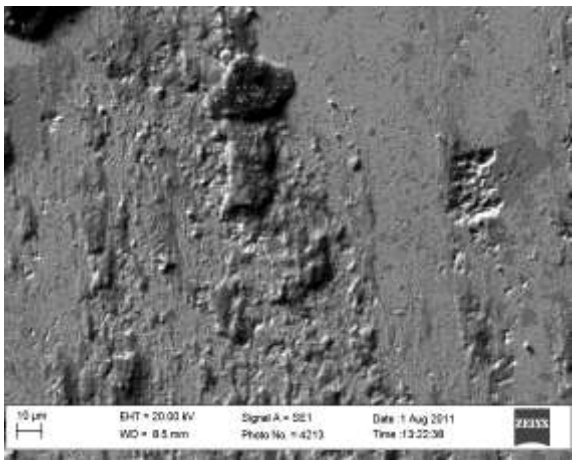

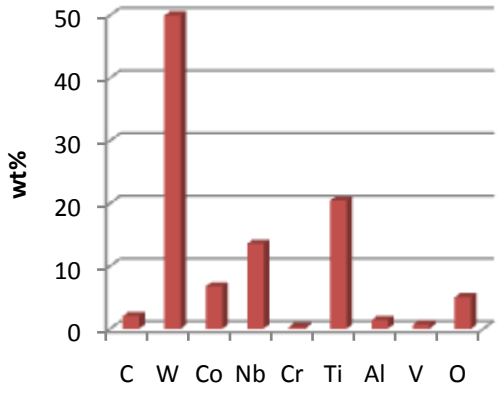

b)

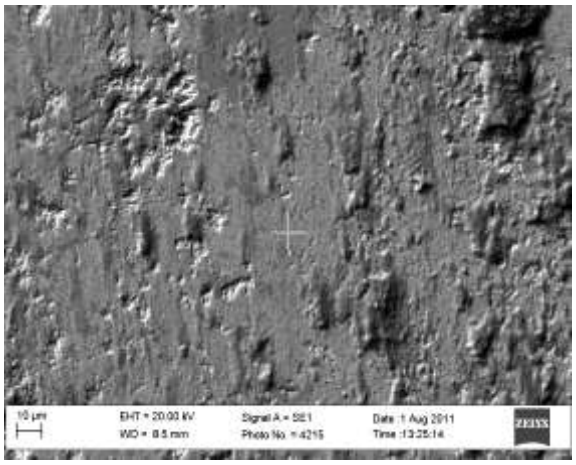

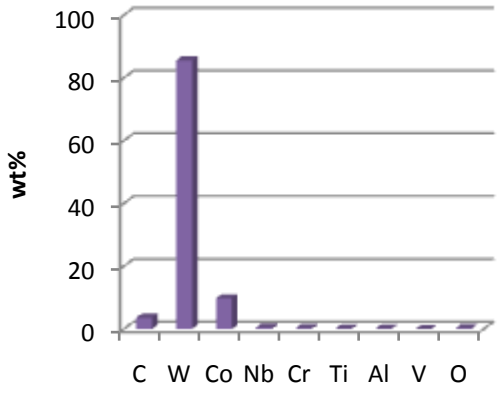

c)

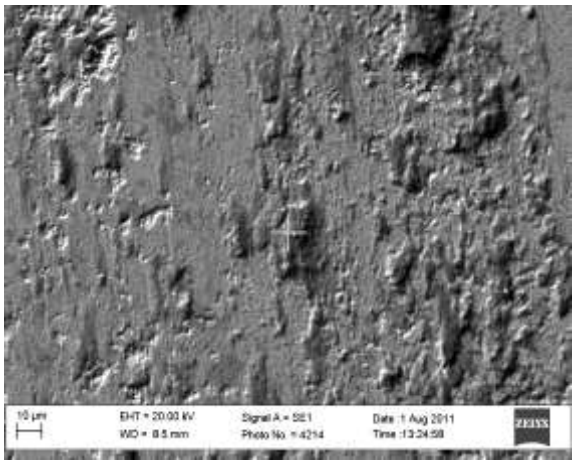

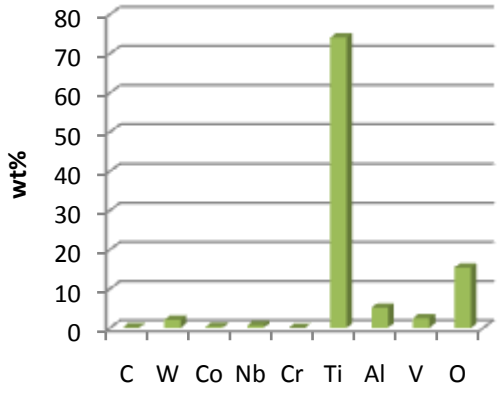

d)

Figure A.13: SEM images of 1wt%NbC/Ti6Al4V contact couple with an applied normal force of 10N; a) 40X area analysis, b) 500X area analysis, c) 500X spot analysis of surface, d) 500X spot analysis of surface formations

Table A.7: Quantitative results for 1wt%NbC/Ti6Al4V contact couple (Figure A.13)

	Element [wt%]								
Figure A.13	**C**	**W**	**Co**	**Nb**	**Cr**	**Ti**	**Al**	**V**	**O**
a)	3.57	58.39	7.72	15.37	0.18	9.66	0.69	0.40	4.02
b)	2.01	49.96	6.73	13.55	0.29	20.42	1.38	0.66	5.01
c)	3.54	85.48	9.74	0.48	0.26	0.12	0.11	0.00	0.27
d)	0.08	2.05	0.33	0.61	0.00	74.05	5.13	2.40	15.35

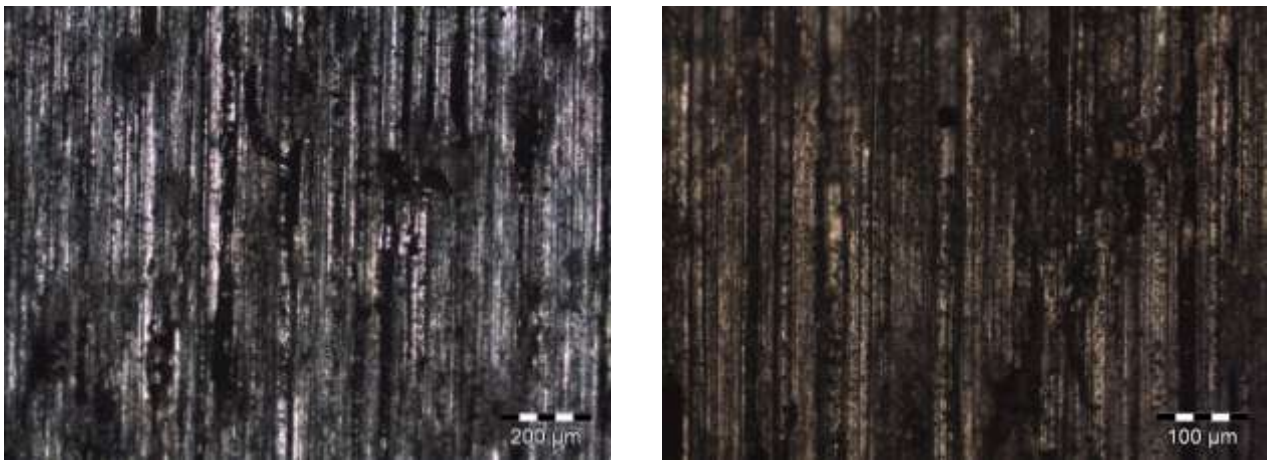

a) 100X b) 200X

Figure A.14: Microscope images of the Ti6Al4V pin couple with 1wt%NbC with a normal force of 10N; a) 100X MAG, b) 200X MAG

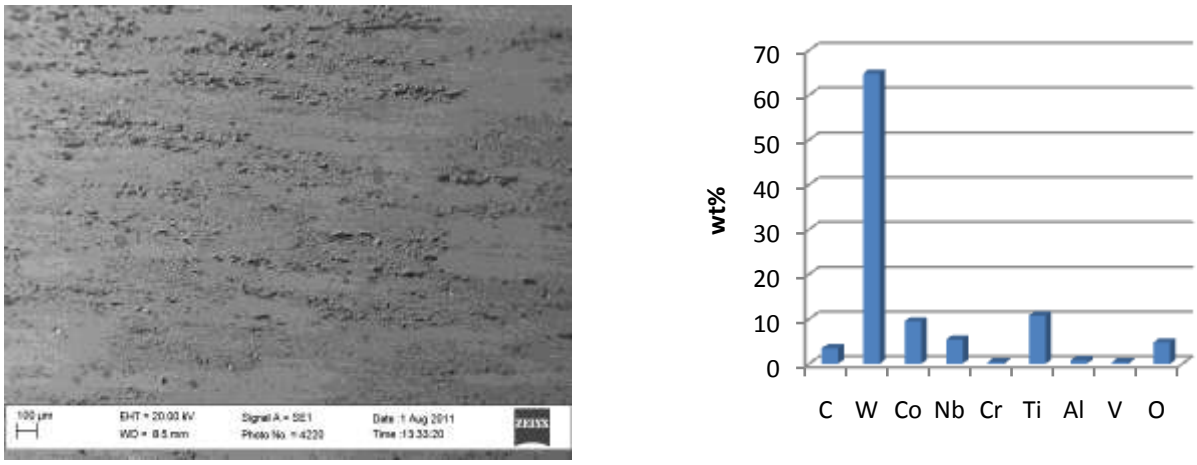

a)

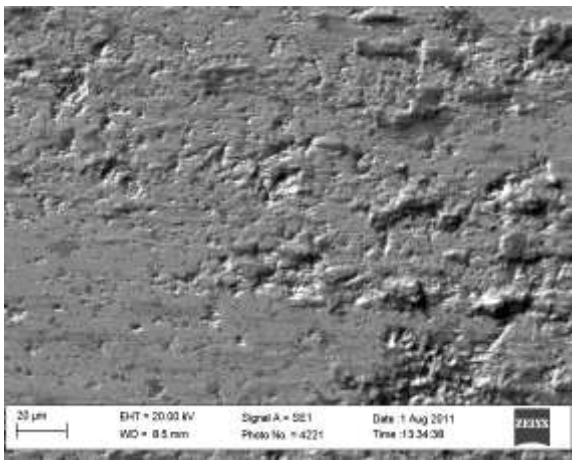

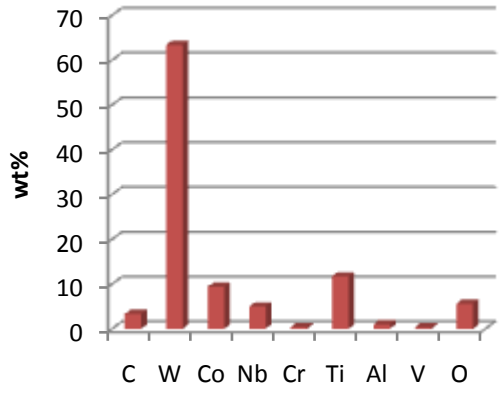

b)

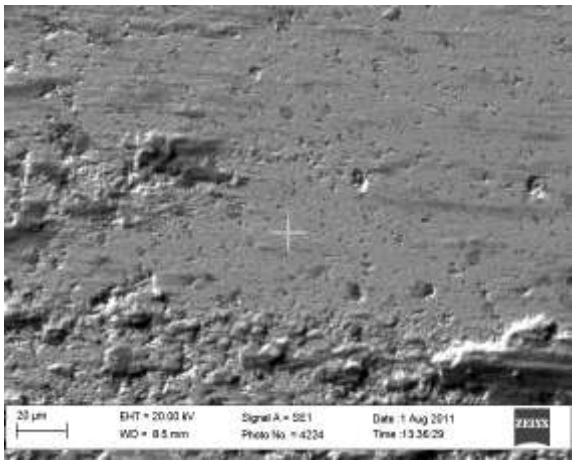

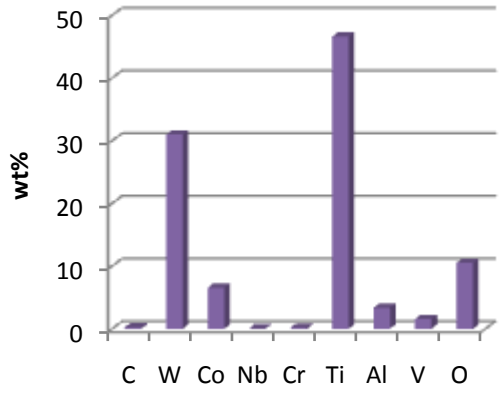

c)

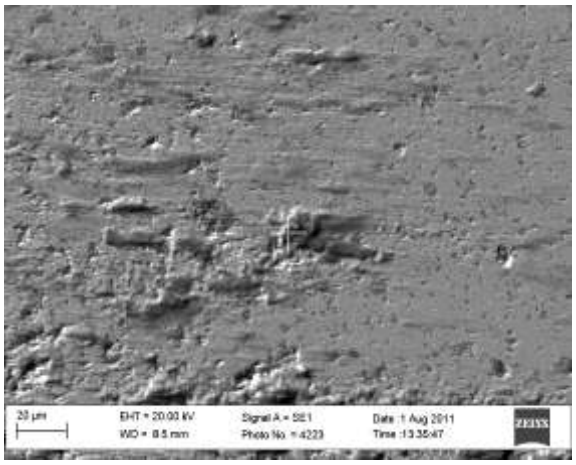

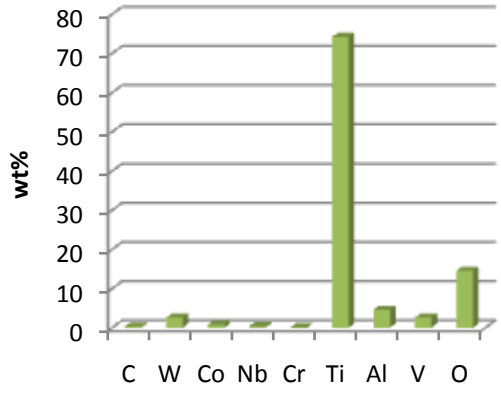

d)

Figure A.15: SEM images of 10wt%NbC/Ti6Al4V contact couple with an applied normal force of 10N; a) 40X area analysis, b) 500X area analysis, c) 500X spot analysis of surface, d) 500X spot analysis of surface formations

Table A.8: Quantitative results for 10wt%NbC/Ti6Al4V contact couple (Figure A.15)

	Element [wt%]								
Figure A.15	C	W	Co	Nb	Cr	Ti	Al	V	O
a)	3.43	64.76	9.44	5.38	0.40	10.74	0.74	0.38	4.73
b)	3.32	63.37	9.37	4.99	0.36	11.69	0.99	0.32	5.59
c)	4.19	86.83	7.54	0.49	0.21	0.13	0.05	0.09	0.48
d)	0.00	13.71	2.35	0.09	0.19	62.37	4.18	1.90	15.22

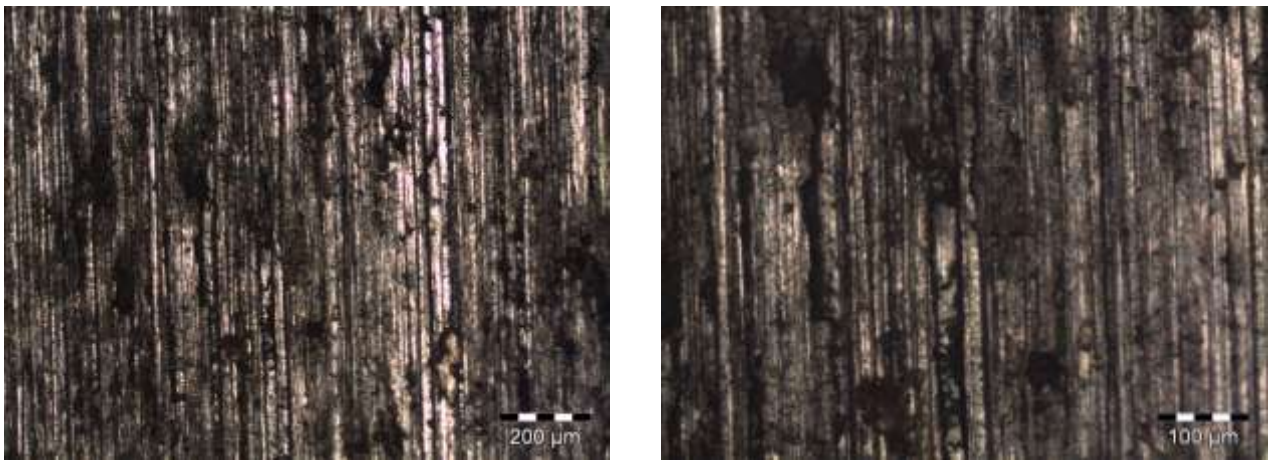

a) 100X b) 200X

Figure A.16: Microscope images of the Ti6Al4V pin couple with 10wt%NbC with a normal force of 10N; a) 100X MAG, b) 200X MAG

Appendix B

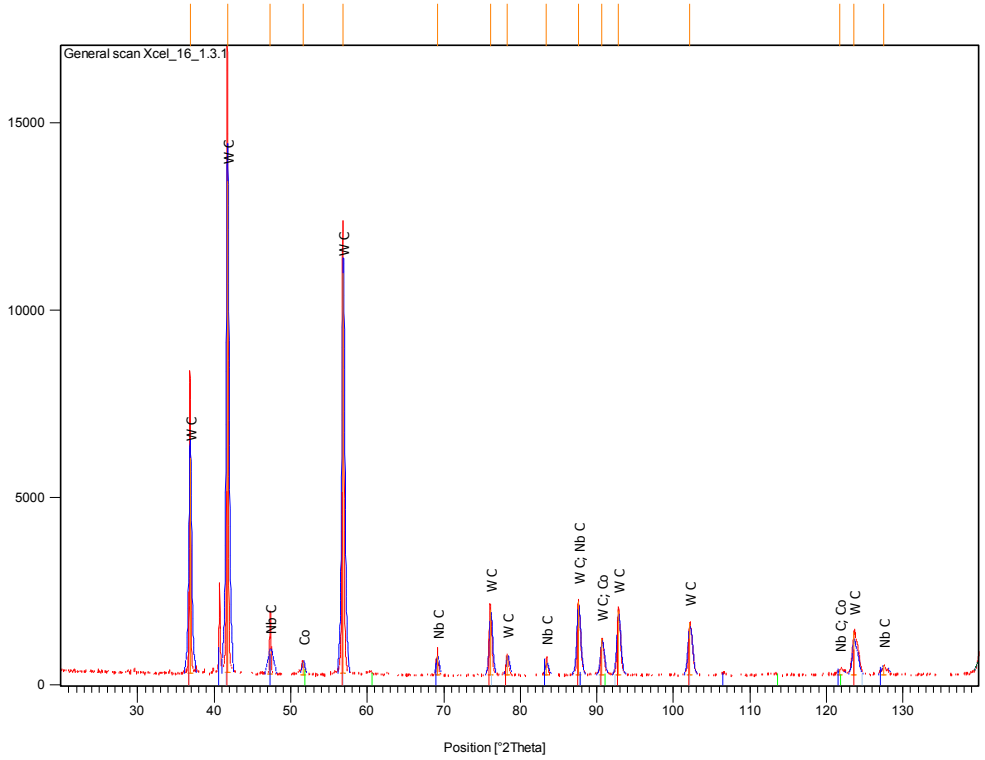

a)

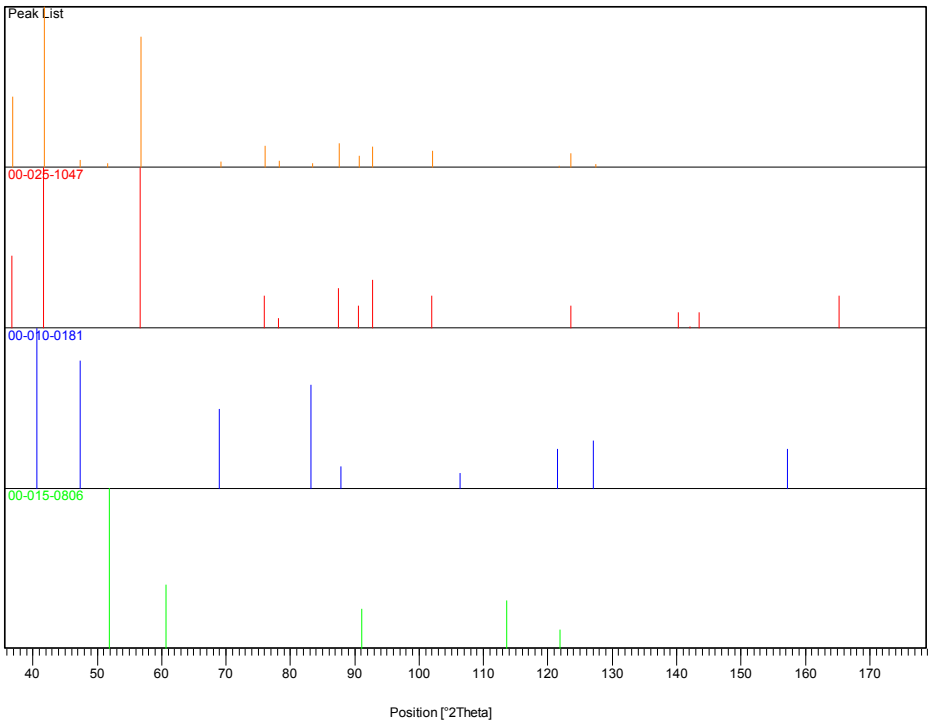

b)

Figure B.1: XRD pattern and phase composition of a WC – 10wt%Co – 1wt%NbC - 0.3wt%Cr_3C_2

Appendix B

Table B.1: Identified patterns list for WC – 10wt%Co – 1wt%NbC - 0.3wt%Cr_3C_2

Ref. Code	Score	Compound Name	Displacement [°2Th.]	Scale Factor	Chemical Formula
00-025-1047	80	Unnamed mineral, syn [NR]	0.000	0.284	W C
00-010-0181	51	Niobium Carbide	0.000	0.041	Nb C
00-015-0806	21	Cobalt	0.000	0.009	Co

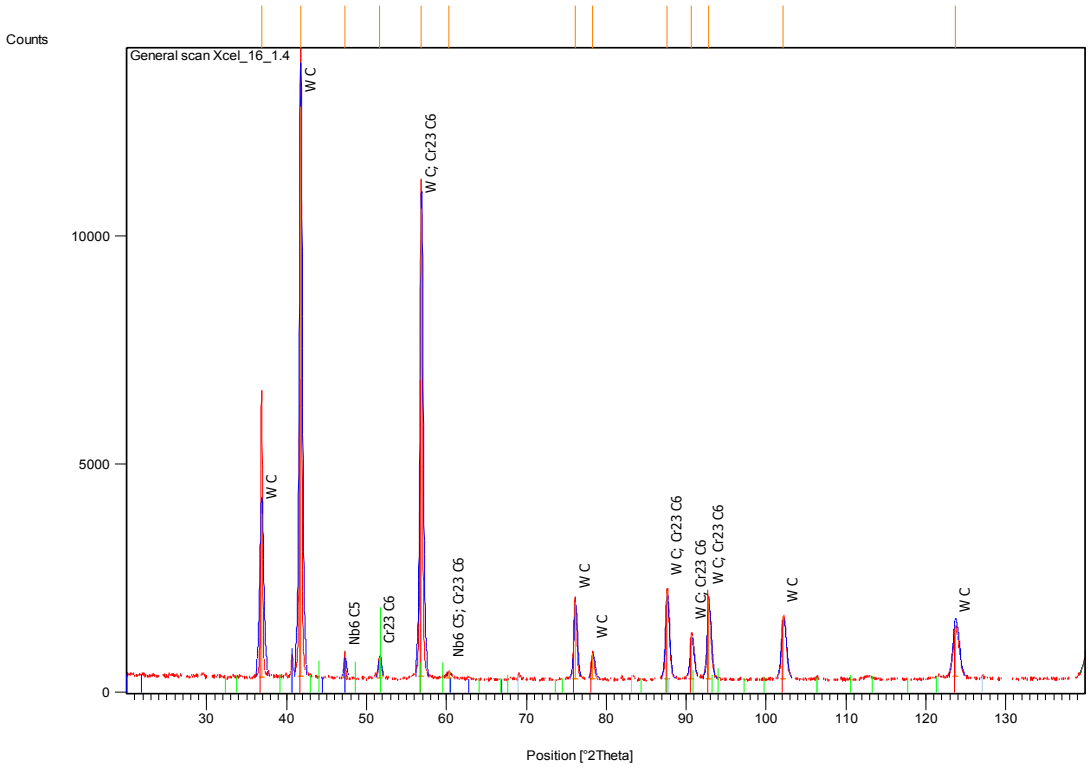

a)

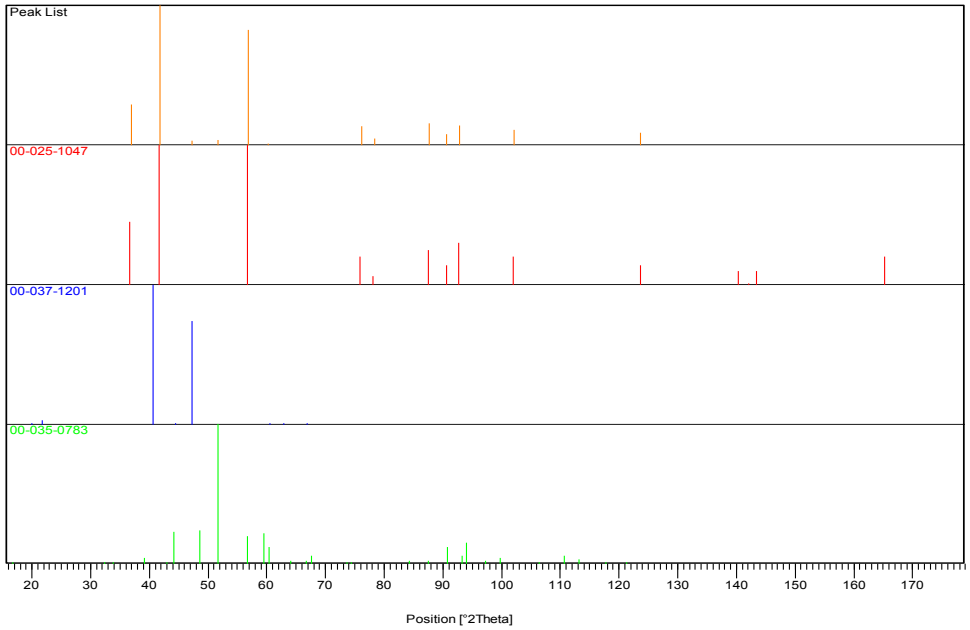

b)

Figure B.2: XRD pattern and phase composition of a WC – 10wt%Co – 3wt%NbC - 0.3wt%Cr_3C_2

Table B.2: Identified patterns list for WC – 10wt%Co – 3wt%NbC - 0.3wt%Cr_3C_2

Ref. Code	Score	Compound Name	Displacement [°2Th.]	Scale Factor	Chemical Formula
00-025-1047	82	Unnamed mineral, syn [NR]	0.000	0.460	W C
00-037-1201	32	Niobium Carbide	0.000	0.044	Nb6 C5
00-035-0783	23	Chromium Carbide	0.000	0.111	Cr23 C6

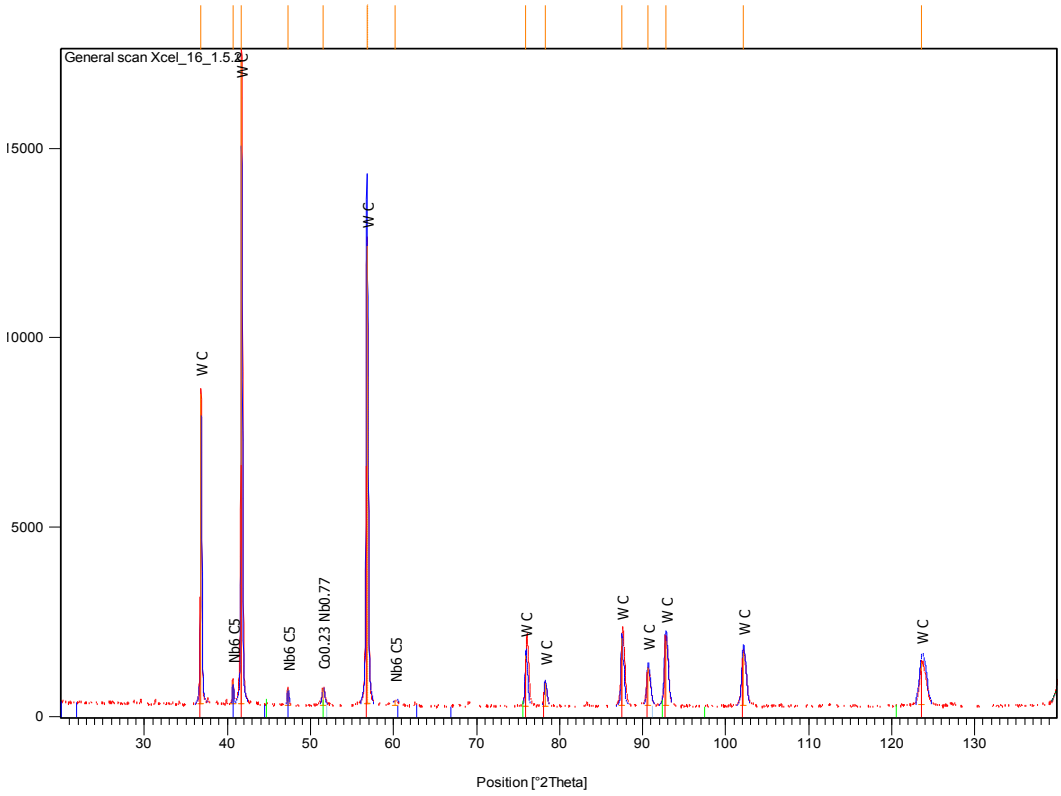

a)

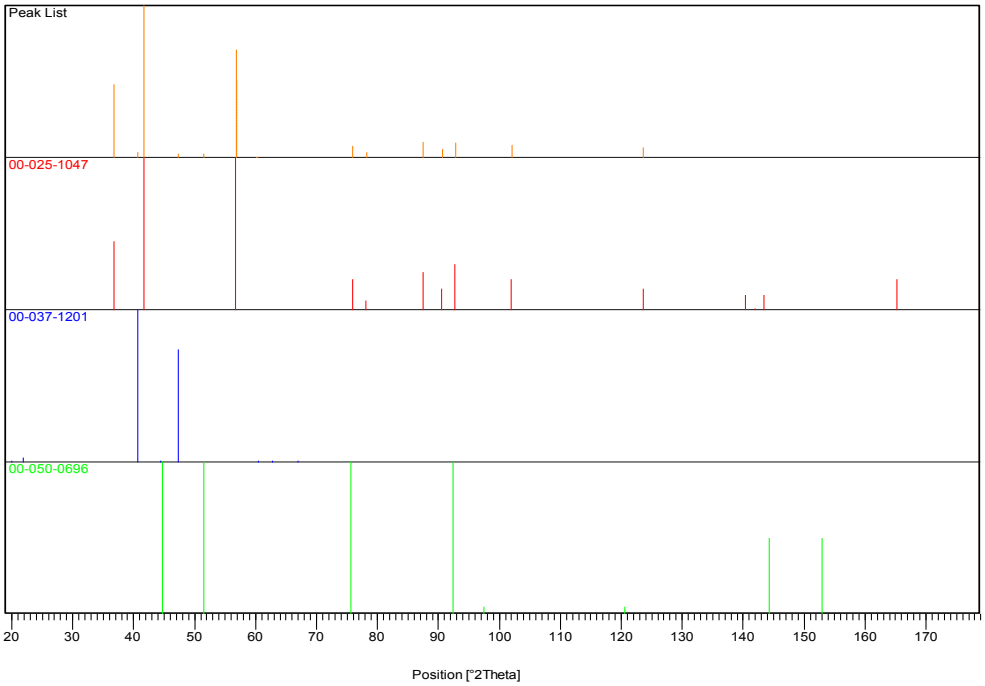

b)

Figure B.3: XRD pattern and phase composition of a WC – 10wt%Co – 10wt%NbC - 0.3wt%Cr3C2

Appendix B

Table B.3: Identified patterns list for WC – 10wt%Co – 10wt%NbC - 0.3wt%Cr3C2

Ref. Code	Score	Compound Name	Displacement [°2Th.]	Scale Factor	Chemical Formula
00-025-1047	77	Unnamed mineral, syn [NR]	0.000	0.357	W C
00-037-1201	61	Niobium Carbide	0.000	0.030	Nb6 C5
00-050-0696	26	Cobalt Niobium	0.000	0.009	Co0.23 Nb0.77

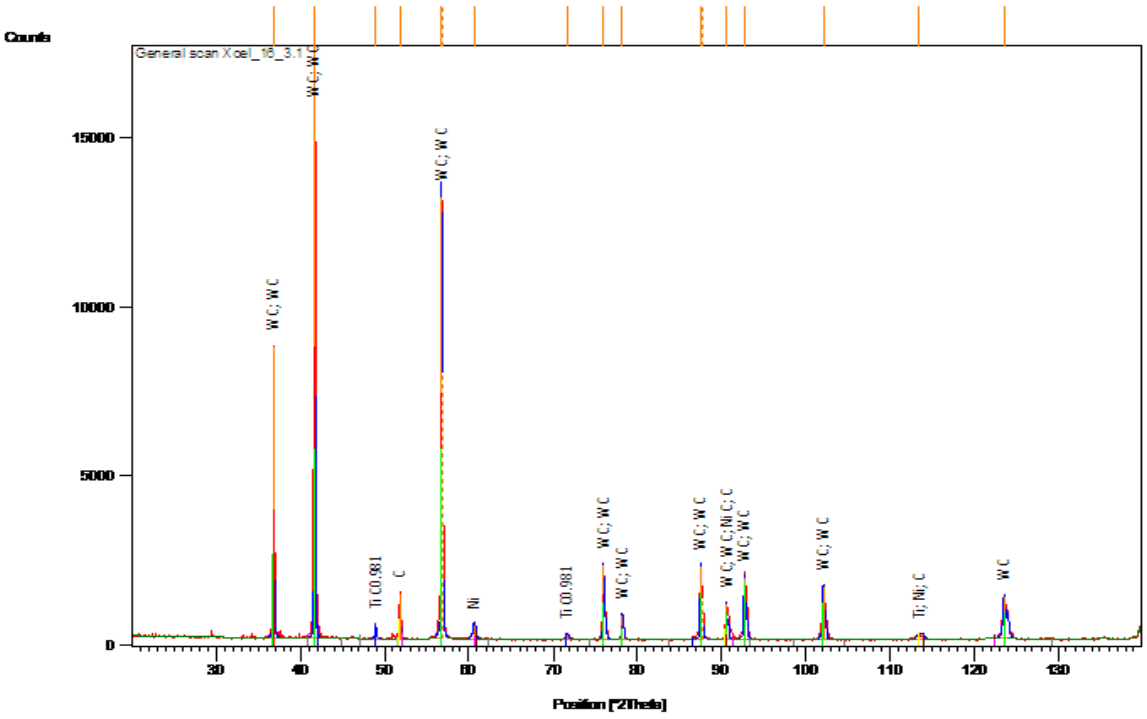

a)

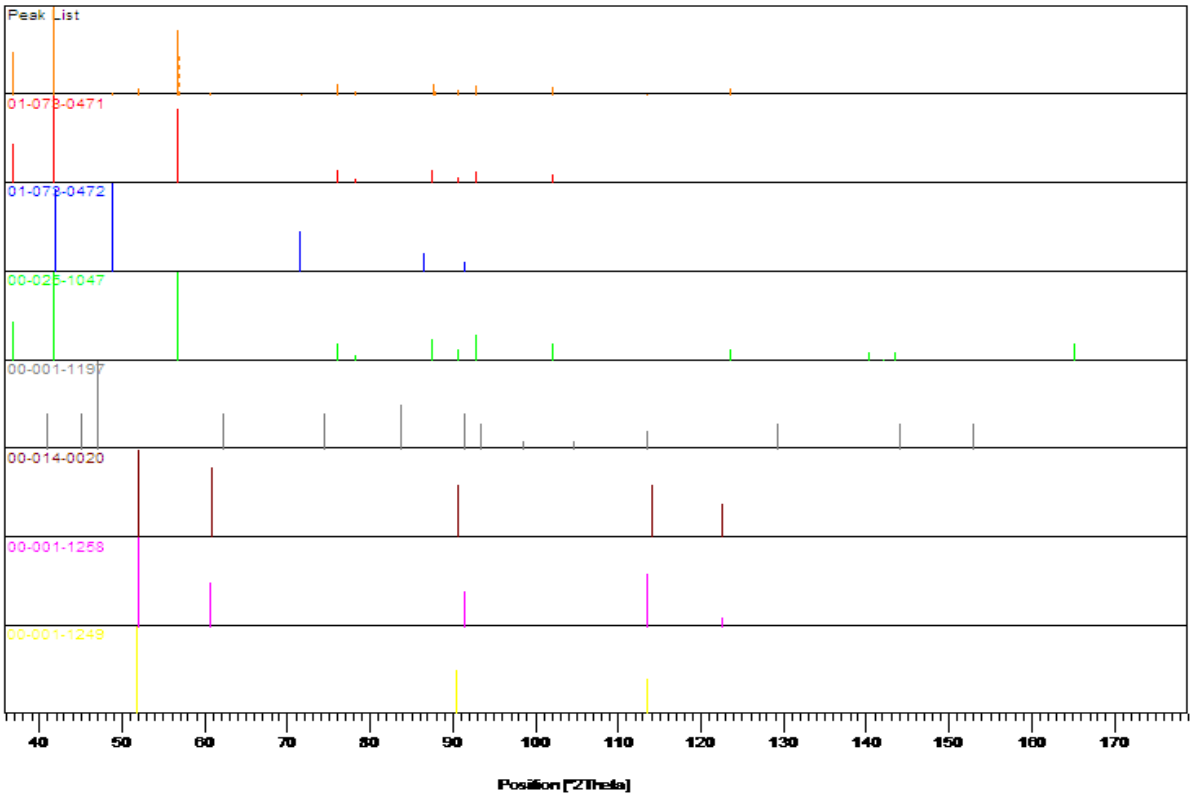

b)

Figure B.4: XRD pattern and phase composition of WC - 9.3wt%Ni - 6.25wt%TiC carbide

Table B.4: Identified patterns list for WC - 9.3wt%Ni - 6.25wt%TiC carbide

Ref. Code	Score	Compound Name	Displacement [°2Th.]	Scale Factor	Chemical Formula
01-073-0471	76	Tungsten Carbide	0.000	0.486	W C
01-073-0472	42	Khamrabaevite, syn	0.000	0.025	Ti C0.981
00-025-1047	71	Unnamed mineral, syn[NR]	0.000	0.316	W C
00-001-1197	6	Titanium	0.000	0.008	Ti
00-014-0020	16	Nickel Carbide	0.000	0.016	Ni C
00-001-1258	32	Nickel	0.000	0.012	Ni
00-001-1249	43	Diamond	0.000	0.037	C

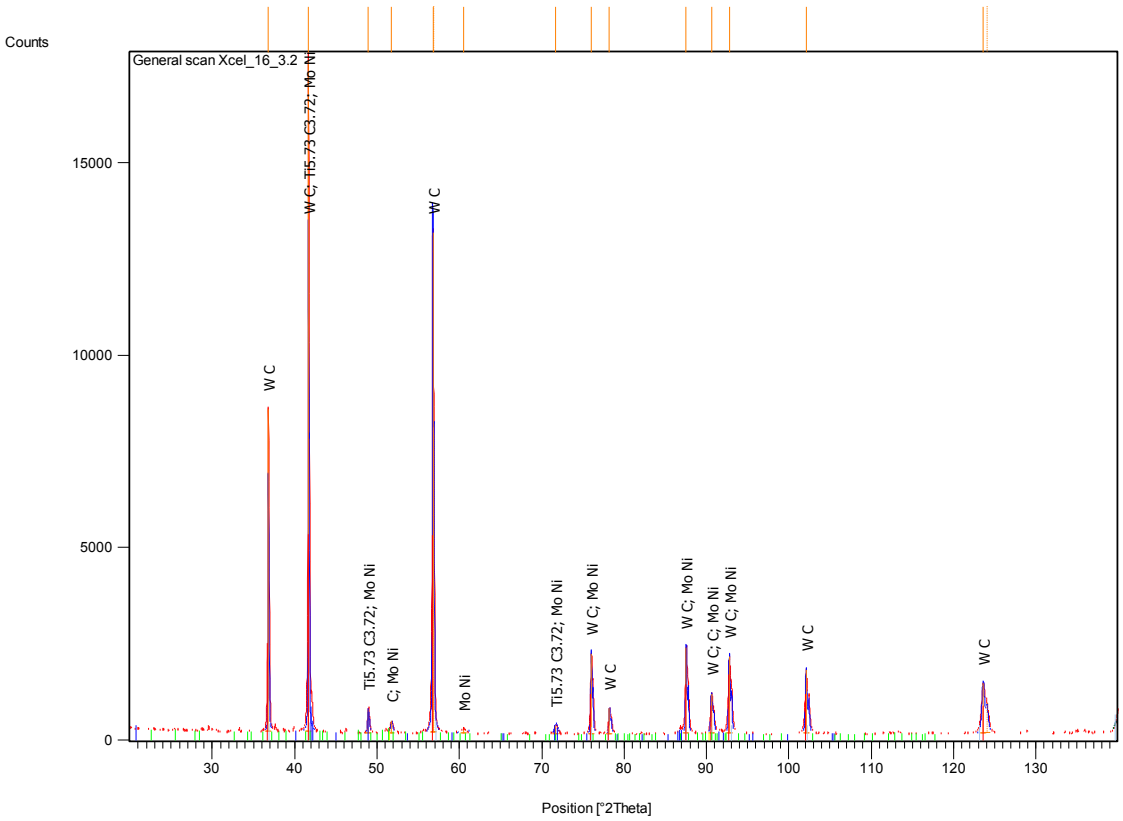

a)

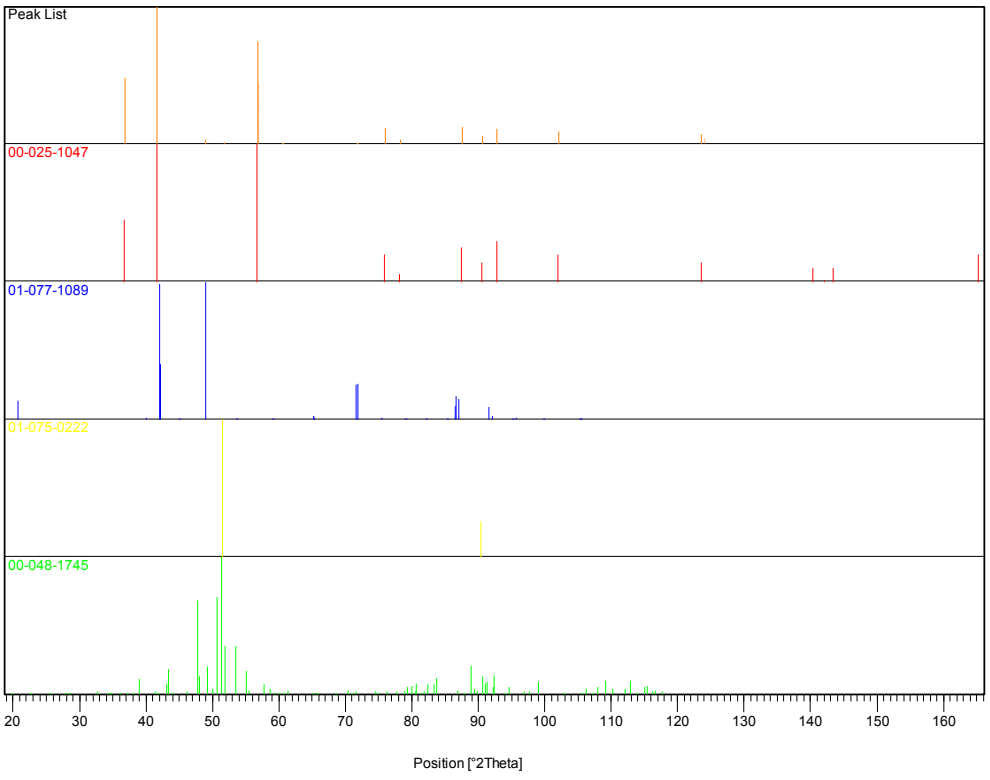

b)

Figure B.5: XRD pattern and phase composition of WC - 9.3wt%Ni - 6.25wt%TiC – 3.5wt%Mo_2C carbide

Table B.5: Identified patterns list for WC - 9.3wt%Ni - 6.25wt%TiC – 3.5wt%Mo2C carbide

Ref. Code	Score	Compound Name	Displacement [°2Th.]	Scale Factor	Chemical Formula
00-025-1047	80	Unnamed mineral, syn [NR]	0.000	0.286	W C
01-077-1089	49	Titanium Carbide	0.000	0.036	Ti5.73 C3.72
01-075-0222	20	Diamond	0.000	0.004	C
00-048-1745	7	Molybdenum Nickel	0.000	0.008	Mo Ni